PEOPLE'S DEMOCRATIC REPUBLIC OF ALGERIA

MINISTRY OF HIGHER EDUCATION AND SCIENTIFIC RESEARCH

Blida 01 University

Institute of Aeronautics and Space Studies

Numerical Simulation On the influence of the clearance between the carter and the diffuser blade on the performance of a centrifugal compressor

A Thesis Submitted by

Mr. yacine BOUCHELAGHEM

In partial fulfillment of the requirements for

The Degree of Master in Aeronautics.

Specialty: Aircraft propulsion

Under the Supervision of

Dr. Sbaa Laazeb

Promotion: 2023-2024

Abstract:

Centrifugal compressors rarely perform exactly as designed due to uncertainties in manufacturing and operation. These uncertainties can negatively impact The actual compressor performance, leading to instability. However, studies examining the combined effects of geometric and operational uncertainties are limited, and the underlying flow mechanisms are poorly understood. This study presents the influence of Tip clearance between the diffuser and the carter of the centrifugal compressor Ziegler. It is an analysis using ANSYS CFX 23 solver, to find the better Tip clearance performances, we use K omega SST as a turbulence module. The results are shown and presented in this study.

ملخص:

نادرًا ما تعمل ضواغط الطرد المركزي تمامًا كما هي مصممة بسبب عدم اليقين في التصنيع والتشغيل. يمكن أن يتأثر أداء الضاغط الفعلي سلبًا بهذه الشكوك، مما يؤدي إلى عدم الاستقرار. هذه الأطروحة تعرض تأثير إزالة الطرف بين الناشر وكارتر ضاغط الطرد المركزي Ziegler. كان الهدف من الدراسة هو فحص تأثير المسافة بين الشفرات والإطار الخارجي على أداء الضاغط. تم إجراء التحليل باستخدام المحلل التجاري ANSYS CFX 23 بناءً على تقنيات الحجم المتناهي. للعثور على أفضل النتائج. نستخدم K omega SST كوحدة اضطراب. تم عرض النتائج وعرضها في هذه الدراسة.

Résumé :

Les compresseurs centrifuges fonctionnent rarement exactement comme prévu en raison des incertitudes de fabrication et de fonctionnement. Ces incertitudes peuvent avoir un impact négatif sur les performances réelles du compresseur, entraînant une instabilité. Cette thèse montre l'effet de la suppression de l'embout entre le diffuseur et le carter du compresseur centrifuge Ziegler. L'étude avait pour but d'examiner l'impact du jeu entre les aube difuseur et le carter sur les performances du compresseur. L'analyse a été réalisée à l'aide de l'analyste commercial ANSYS CFX 23, en utilisant des techniques de volume finie. nous utilisons K omega SST comme module de turbulence. Les résultats sont présentés dans cette étude.

ACKNOWLEDGEMENT

We would like to thank ALLAH, the almighty for giving us gave courage and determination to do this modest work.

We would like to express our sincere thanks to our promoter "LAAZAB Sbaa" for his patience, remarks and advice,
his availability and caring.

Special thanks to Dr. T. Rezzoug for supporting us with materials.

We thank the members of the jury who kindly presented today.

Our thanks also go to all our teachers from Aircraft Propulsion to our training.

And to all those who participated directly or indirectly in the realization of this work.

Thank you all

الإهداء

وُجد الإنسان على وجه البسيطة، ولم يعش بمعزل عن باقي البشر وفي جميع مراحل الحياة، يُوجد أُناس يستحقُّون منَّا الشُّكر.

أهدي بحثي المتواضع هذا إلى صاحب السيرة العطرة، والفكر المُستنير والدي الحبيب، أطال الله في عُمره.

إلى من وضعتني على طريق الحياة، وجعلتني رابط الجأش، ورعتني حتى صرت كبيرًا أمي الغالية، طيَّب الله ثراها.

إلى إخوتي؛ من كان لهم بالغ الأثر في كثير من العقبات والصعاب.

إلى جميع أساتذتي الكرام؛ ممن لم يتوانوا في مد يد العون لي.

إلى جميع إخوتي وأصدقائي في الإقامة الجامعية كل باسمه لجميع اللحظات التي لا تُنسى التي قضيناها معًا.

Summer

List of Figures:

Chapter 1:

Chapter 2:

Chapter 3:

Chapter 4:

Table List:

Chapter 2:

Chapter 4:

INTRODUCTION:

Turbomachinery encompasses a wide range of devices that transfer energy between a rotor and a fluid, including both turbines and compressors. These machines are essential in various applications, from power generation to propulsion in aircraft. The primary function of turbomachinery is to convert energy between mechanical and fluid forms, thereby enabling the operation of engines, pumps, and other critical systems.

Turbomachinery can be broadly classified into two categories based on their function: turbines and compressors. Turbines extract energy from fluids, compressors work by taking in low-pressure fluid and compressing it to a higher pressure, which is essential in processes like gas transmission, refrigeration, and aeronautics.

In the field of aeronautics, centrifugal compressors play a pivotal role in jet engines and gas turbines. These compressors are preferred in aircraft engines due to their high efficiency and compact design. They enable the engines to achieve the necessary pressure ratios to ensure efficient combustion and thrust generation.

The flow in a centrifugal compressor is generally viscous and turbulent, three-dimensional, unsteady, and compressible fluid.

The study and analysis of the flow in this compressor can be done through two methods, the numerical method and the experimental method.

The numerical method is done using the ANSYS CFX logical. It is composed of four modules which are Blade Gen to create geometry, TurboGrid to generate mesh, TASCflow to solve the system, and CFD Post to present the results.

This work is divided into four chapters

The first chapter: presents generalities on turbomachines and the general definitions concerning centrifugal compressors and their classification.

The second chapter: presents the general equations governing the flows, the method of calculating aerothermodynamic parameters in a centrifugal compressor stage, and turbulence models, we will use K omega SST for this study.

The third chapter: this chapter deals with the numerical modeling and the presentation of the software using ANSYS CFX. The modeling of the geometries of the centrifugal compressor stage and the following mesh of the conditions have been created.

Fourth chapter: the results are present for the centrifugal compressor stage at a nominal point, and present the flow influence, and Tip clearance influence.

Many researchers have already analyzed the flow in a centrifugal compressor. The parameters considered by researchers:

Kai U. Ziegler, Heinz E. Gallus, Reinhard Niehuis (2002): This study presents an experimental investigation of the effect of impeller-diffuser interaction on the unsteady and time-averaged flow configuration in the impeller and diffuser and the performance of these components.

Rui Zhu, Yaping Ju, Chuhua Zhang(2021): This study presents both deterministic and uncertainty analyses of a centrifugal compressor stage, considering geometric and operational uncertainties simultaneously. It combines CFD simulation with nonintrusive sparse grid-based stochastic collocation methods.

CHAPTER 1: GENERALITIES

1.1. INTRODUCTION

The energy consumption of mankind has been steadily increasing. The production of mechanical energy from the basic sources of energy and the consumption of that mechanical energy to run the devices to make life easier require various systems. These systems have different components with varied functions and complexities. Some of these components are those in which the fluids flow and cause energy conversion. Various types of turbines that produce mechanical energy and various types of pumps and compressors that consume mechanical energy possess some common features.

These components, termed under a common name – turbomachines, have the same basic principles of working. Whether it is a tiny fan measuring just 5 cm in diameter to provide the circulation of cooling air to a laptop or a steam turbine producing hundreds of megawatts of power to run electrical generators, the design principles are based on the same fundamentals. This book is intended to make an effort to understand such fundamentals concerning turbomachines.

1.2. Turbomachine

A turbomachine is a mechanical assembly designed to facilitate the exchange of energy between a flowing fluid and a rotor, typically rotating uniformly around its axis. Turbomachinery encompasses a variety of machines that utilize fluid to convert energy. Broadly speaking, a turbomachine is characterized as a device enabling the transfer of energy to or from a fluid through the dynamic action of a rotating component known as a rotor. Comprising static and/or mobile components, a turbomachine consists of one or more rotating wheels (rotors) fitted with blades (vanes), creating passages for fluid flow.

The energy exchange occurs within the rotor, driven by aerodynamic forces acting on the blades as a result of fluid flow, primarily influenced by pressure differentials across the blade surfaces.

1.3. Classification of turbomachines

1.3.1. Based on energy transfer

a) Energy is given by fluid to the rotor - Power generating turbo machine E.g. Turbines

b) Energy is given by the rotor to the fluid – Power absorbing turbo machine E.g. Pumps, blowers, and compressors.(see *Figure 1. 1*)

1.3.2. Based on fluid flowing in the turbo machine

- Water
- Air
- Steam
- Hot gases
- Liquids like petrol etc.

1.3.3. Based on the direction of flow through the impeller or vanes or blades, concerning the axis of shaft rotation

- Axial flow – Axial pump, compressor or turbine.
- Mixed flow – Mixed flow pump, Francis turbine.
- Radial flow – Centrifugal pump or compressor.
- Tangential flow – Pelton water turbine.

1.3.4. Based on the fluid condition in the turbo machine

a- Impulse type (constant pressure) E.g. Pelton water turbine.

b-Reaction type (variable pressure) E.g. Francis reaction turbines.

1.3.5. Based on the position of the rotating shaft

a) Horizontal shaft – Steam turbines.

b) Vertical shaft – Kaplan water turbines.

c) Inclined shaft – Modern bulb micro

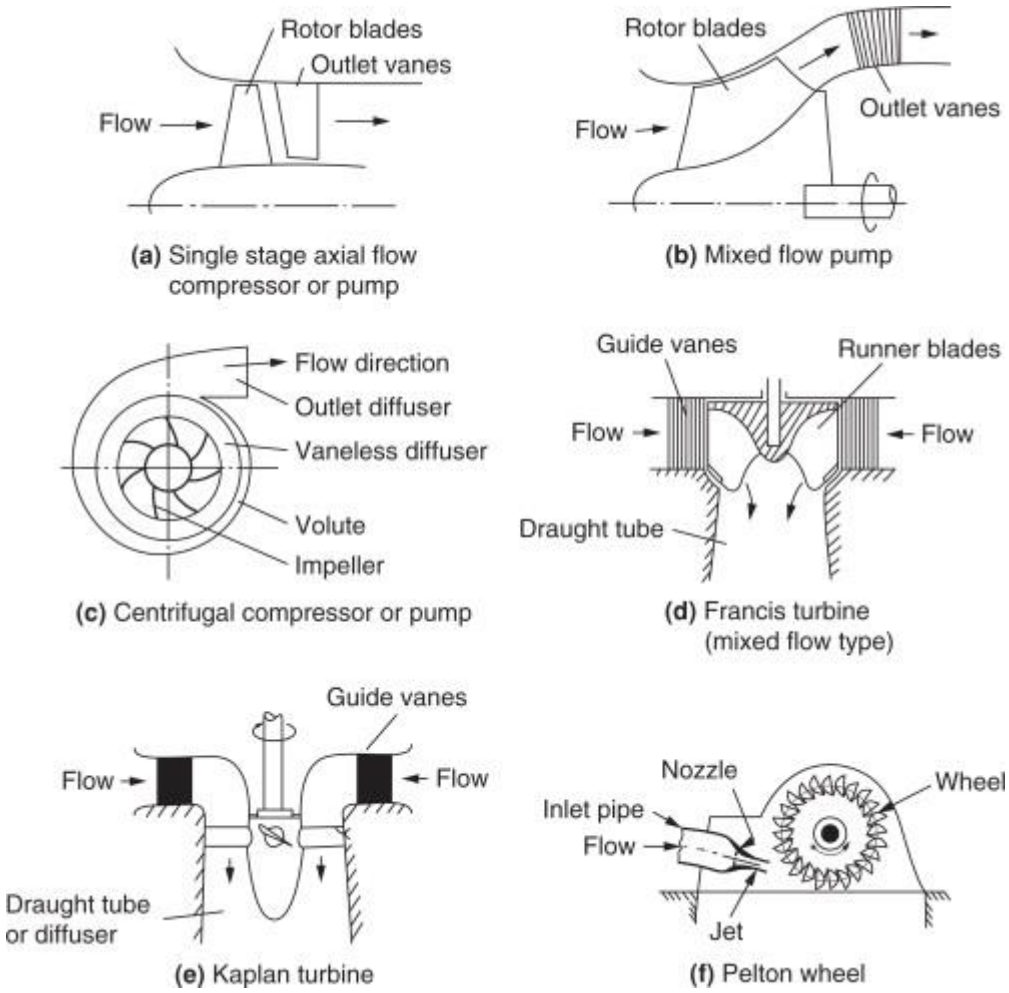

Figure 1. 2: the different types of turbomachine **[10]**

1.4. Centrifugal Compressor

The centrifugal compressor can be centrifugal or radial then centrifugal; it produces compressed air for combustion, air conditioning, propulsion...etc. In the centrifugal compressor, high pressure is achieved to give kinetic energy to the fluid.

The speeds are relatively high and it happens that at such speeds; the compressor chokes and even reaches the breaking of the blades, this is due to the Mach number (the shock wave), when it approaches unity, it is a zone to avoid.

Another phenomenon occurs at low speeds which is pumping, the effect of compressibility is taken into consideration at each point of the compressor.

The fluid that passes through the compressor wheel gives it energy by imparting a relatively high outlet velocity (subsonic) depending on the desired compression ratio. In a centrifugal compressor, a "wheel" composed of blades (see figure (I.6)) axially sucks in the air and radially discharges it after accelerating and compressing it, thanks to the effect of centrifugal force and rotation speed. This air is then straightened in a fixed blade which converts some of the kinetic energy into pressure. A collector collects this compressed air figure.

The compressor has the advantage of providing a compression ratio, in one stage higher than that of a 5-stage axial compressor, on the other hand, its radial size is significant.

Centrifugal compressors are capable of providing a flow rate of 900 to 35,000 m^3/h. They are found as soon as the required capacity exceeds 7000 m^3/h. Beyond 35,000 m^3/h, it is the axial flow compressors that take over.

- ✓ They are particularly suitable and energy efficient when the demand is relatively constant and high.
- ✓ Their specific consumption at full load ranges between 100 and 125 h/m^3.

Among their competitors, axial compressors, reciprocating compressors, and screw compressors, the centrifugal compressor is the solution in many situations.

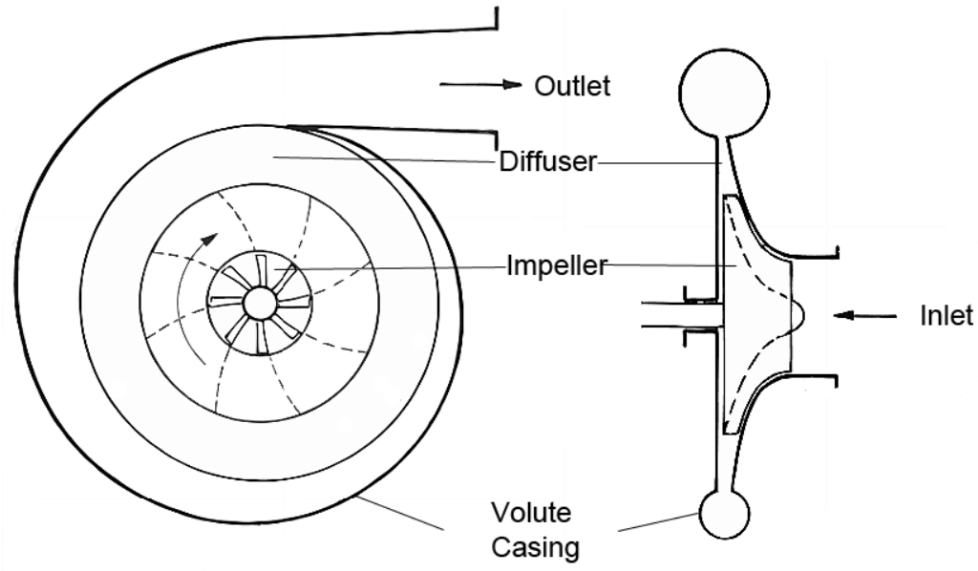

Figure 1. 3: The mechanical components of a centrifugal compressor**. [5]**

1.5. The mechanical components of a centrifugal compressor

Like any mechanical system, the centrifugal compressor is composed of certain mechanical elements to accomplish its task. These elements are generally made of aluminum alloy. In the following, each of these components will be represented individually.

1.5.1. The upstream part of a compressor

The upstream part is responsible for bringing the flow to the impeller. Generally, various elements are distinguished such as axial pre-rotation valves at the inlet, and a feed plenum.

1.5.2. The rotor (wheel)

The wheel is the fundamental element of the compressor, as it ensures the exchange of work; it is indeed the only moving element of the stage.

1.5.3. The diffuser

At the exit of the rotor, the static pressure of the flow increases, but a portion of the total pressure provided by the wheel is present in the form of kinetic energy. The role of the diffuser is to slow down this flow, as losses in the downstream ducts depend heavily on the Mach number of the flow. This deceleration also allows the conversion of some of the kinetic energy into static pressure energy.

1.5.4. The volute

The main role of the volute is to collect the radial flow at the exit of the diffuser, to return it to the system through a tubular conduit, using a change in the passage section. The flow in the volute is often modeled (assuming incompressible fluid) by logarithmic spirals, but a portion of the fluid completes the full turn and joins the main flow at the throat (the beginning zone of the spiral)(see *Figure 1. 2*).[4]

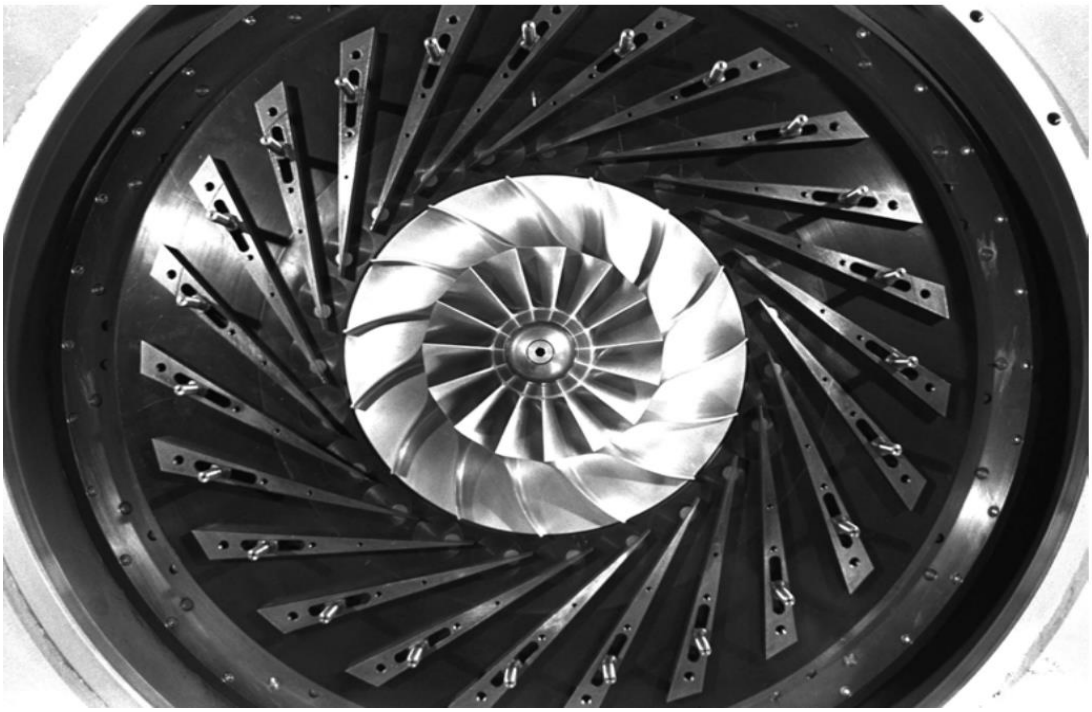

Figure 1. 4: centrifugal compressor stage[5]

1.6. Functioning principle of a centrifugal compressor

Centrifugal compressors find widespread use across various industrial applications due to their efficient operation, ability to tolerate significant process fluctuations, and high reliability compared to alternative compressor types.

Initially, gas is drawn into the compressor through the suction flange, entering an annular chamber known as the aspiration volute. Here, it converges uniformly towards the center in all radial directions. To prevent gas vortex formation, a fin is positioned in the annular chamber opposite the suction flange. The gas then proceeds to the aspiration diaphragm and is drawn in by the first impeller.

As the impeller accelerates, the gas is propelled towards the periphery, simultaneously increasing its velocity and pressure. At the outlet, the gas possesses both radial and tangential components of velocity. Following a spiral path, the gas moves through a circular chamber formed by a diffuser, where velocity decreases while pressure rises.

Subsequently, the gas flows through the return channel, another circular chamber delimited by two rings forming the intermediate diaphragm housing the blades. These blades guide the gas towards the suction of the subsequent impeller, straightening out its spiral motion to facilitate radial outlet and axial inlet into the next impeller.

This process repeats for each impeller, with labyrinth seals comprising multiple ring segments fitted to the diaphragm to minimize internal gas leakage. The last impeller of the stage directs the gas into a diffuser, leading to the discharge volute, an annular chamber that gathers gas from the diffusers' periphery and directs it to the discharge flange. Adjacent to the discharge flange, another vane prevents gas from returning to the volute, directing it instead towards the discharge flange.

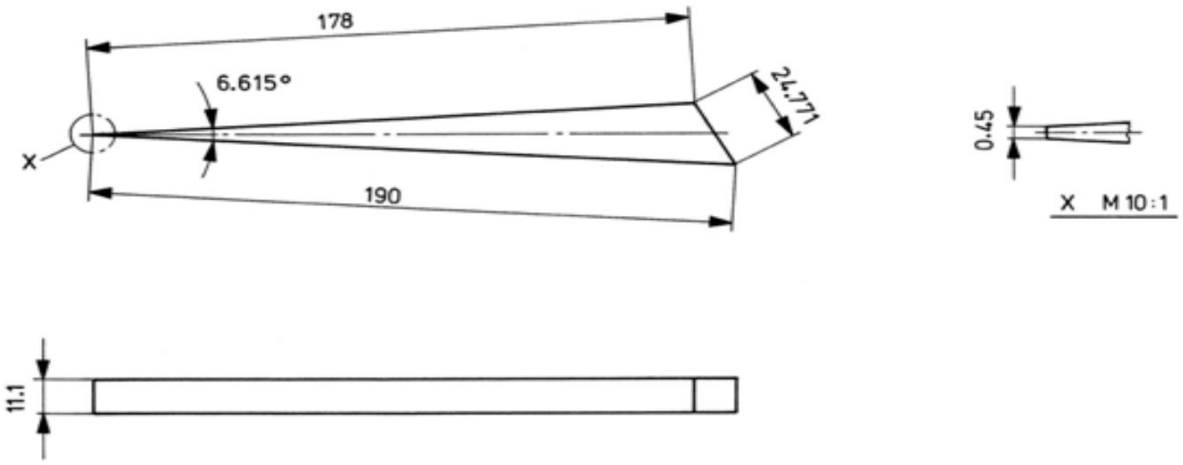

Figure 1. 5: the diffuser shape [***6]***

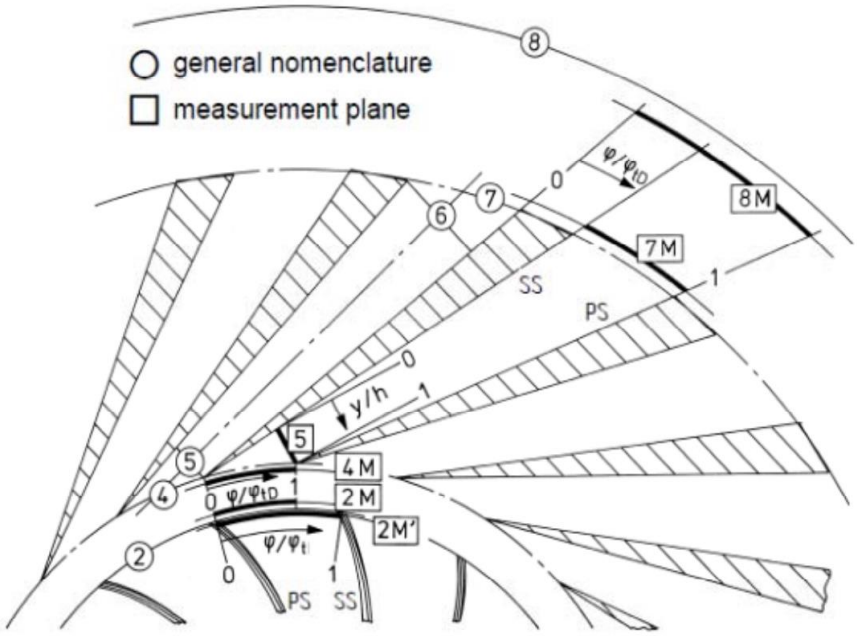

Figure 1. 6: Blade-to-Blade view [6]

1.7. Reference planes in a centrifugal compressor

The three planes of a centrifugal compressor are essential for understanding its operation:

1.7.1. Meridional Plane

This plane is perpendicular to the axis of rotation and passes through the centerline of the compressor. It provides a view of the compressor's components along the axis, including the inlet, impeller/rotor, diffuser, and collector.

1.7.2. Orthogonal Plane

Also known as the blade-to-blade plane, this plane is perpendicular to the meridional plane and intersects the blades of the impeller. It allows for the examination of the flow between the blades and the pressure variations induced by each blade as the fluid passes through the compressor.

1.7.3. Blade-to-Blade Plane

This plane is crucial for analyzing the interaction between adjacent blades of the impeller. It helps in understanding the pressure variations and energy transfer that occur as the fluid flows through the compressor, particularly focusing on the blade design and the resulting flow dynamics.(see Figure 1. 6)

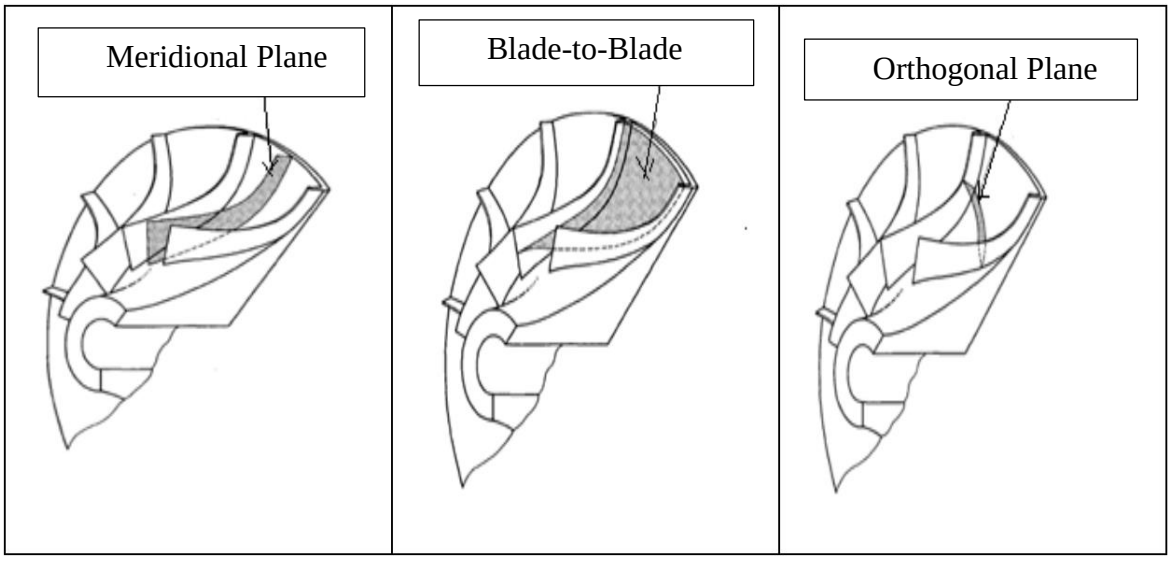

Figure 1. 7: The Reference planes in a centrifugal compressor[13].

1.8. Velocity triangle

The velocity triangle is a graphical representation of the kinematic principle according to which the absolute velocity vector V of a fluid particle is composed of the relative velocity vector W relative to the moving wheel plus the linear velocity vector U of the moving wheel. (see Figure 1. 7)The absolute velocity can thus be written as:

With:

$$U = \Omega r \quad \textbf{(I.1)}$$

Ω and r represent the rotor's rotational speed (in radians per second) and the radial distance of the fluid particle, respectively.

The angles α and β represent the absolute and relative angles of the flow, respectively. Integrating the velocity triangles into the Euler equation allows the calculation of the power exchanged between the wheel and the fluid. The torque τ exerted on a fluid particle results in a change in the tangential velocity from $V_{\theta 1}$ to $V_{\theta 2}$:

$$\tau = m^{\cdot} \left(r_2 V_{\theta 2} - r_1 V_{\theta 1} \right) \quad \textbf{(I.2)}$$

with $r_1 V_{\theta 1}$ and $r_2 V_{\theta 2}$ representing the angular momenta at the wheel's entry and exit, respectively. By multiplying by the wheel's rotational speed, the exchanged power can then be written as:

$$P_{ech} = \Omega \tau = m^{\cdot} \left(U_2 V_{\theta 2} - U_1 V_{\theta 1} \right) \quad \textbf{(I.3)}$$

According to this equation, the work that the fluid can receive through the impeller is related to the impeller's ability to produce a change in the mean radius ($U = r\Omega$) and a change in V_θ. This allows centrifugal compressors to achieve higher compression ratios than those found in axial compressors because the radius increases from the inlet to the outlet of the impeller.

The work absorbed by the compressor per unit mass is obtained by dividing equation **(I.3)** by the mass flow rate m.

$$\omega_r = U_2 V_{\theta 2} - U_1 V_{\theta 1} \quad \textbf{(I.4)}$$

For an adiabatic flow, the integration of the first law of thermodynamics shows that:

$$\omega_r = h_{t2} - h_{t1} = U_2 V_{\theta 2} - U_1 V_{\theta 1} \quad \textbf{(I.5)}$$

Where h_t is the enthalpy per unit mass of fluid. The work exchanged through the wheel therefore depends on the tangential component of the velocity vectors V_θ.

For an exit velocity vector located in a plane normal to the axis of rotation, the velocity triangle at the exit allows us to write:

$$V_{r2}^2 = V_2^2 - V_{\theta 2}^2 = W_2^2 - W_{\theta 2}^2 = W_2^2 - \left(U_2 - V_{\theta 2}\right)^2 \quad \textbf{(I.6)}$$

We thus derive the following relationship:

$$U_2 V_{\theta 2} = \frac{1}{2}\left(V_2^2 + U_2^2 - W_2^2\right) \quad \textbf{(I.7)}$$

And:

$$U_1 V_{\theta 1} = \frac{1}{2}\left(V_1^2 + U_1^2 - W_1^2\right) \quad \textbf{(I.8)}$$

the expression of the variation of the total enthalpy:

$$h_{t2} - h_{t1} = \frac{1}{2}\left[\left(V_2^2 - V_1^2\right) + \left(W_1^2 - W_2^2\right) + \left(U_2^2 - U_1^2\right)\right] \quad \textbf{(I.9)}$$

The term $\left(V_2^2 - V_1^2\right)$ represents the input of kinetic energy received by the fluid. Increasing the velocity V_2 can ensure a maximal contribution to this term in the increase of enthalpy.

The term $\left(W_1^2 - W_2^2\right)$ represents diffusion in the relative frame, or the slowing down of flow in the relative frame. This term justifies the divergent shape of the inter-blade passage.

The term $\left(U_2^2 - U_1^2\right)$ represents the centrifugal effect, which is the strong point of centrifugal compressors where the radius at the wheel outlet is much larger than the inlet radius.

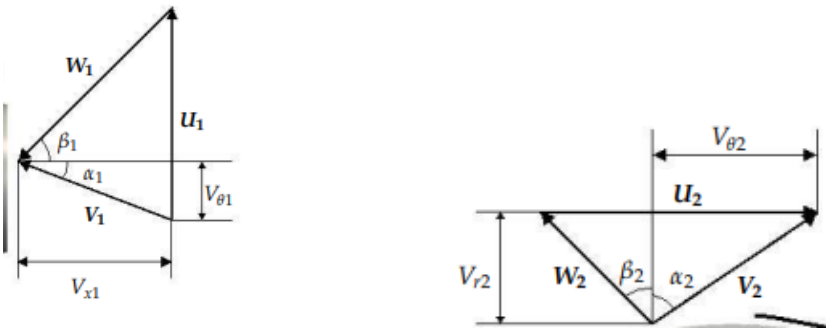

Figure 1. **8:** impeller's entry triangle-diffuser's out triangle [7]

1.9. Characteristic curves

In general, the characteristic curves of a compressor (see Figure 1. 8) are represented by plotting mass flow rate (ṁ) on the x-axis and compression ratio on the y-axis for a given rotational speed.

$$\Pi_{tt} = \frac{P_{ts}}{P_{te}} \qquad \textbf{(I.10)}$$

$$\eta_{in} = \frac{PR_{in}^{\frac{\gamma}{\gamma-1}} - 1}{TR - 1}$$

The performance is presented in a flow-pressure field, where the compressor's iso-speed curves, iso-efficiency curves, and operating limits are indicated, as shown in the figure.

Similar to the figure, the use of reduced values helps to keep the compressor map invariant concerning the fluid inlet conditions. The reduced flow value is often referenced to standard conditions, specific to each manufacturer, and in the form indicated below (mass flow rate): Pressure values are indicated in the form of compression ratios, where the values considered are absolute and the pressures are total pressures. The rotational speeds are also expressed in reduced values.

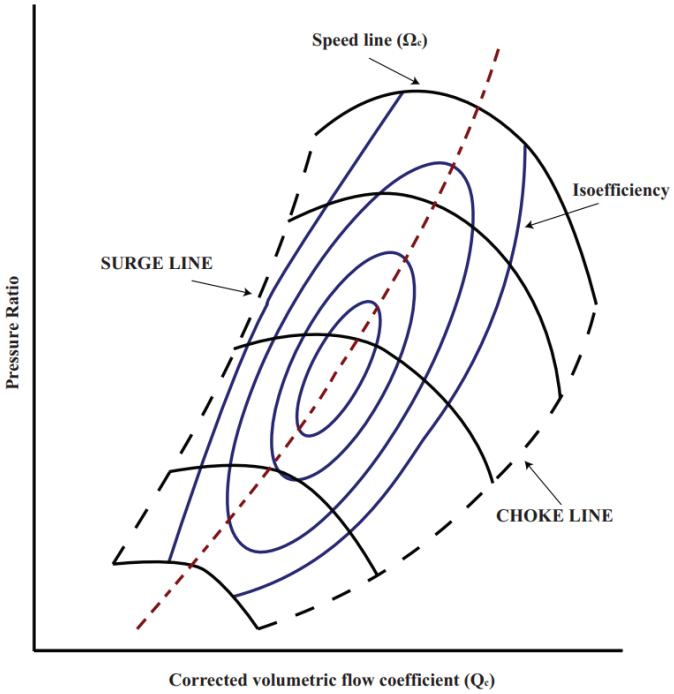

Figure 1. 9: centrifugal compressor chart [8]

1.10. The Losses in a Centrifugal Compressor

the efficiency of a centrifugal compressor is affected by various losses that occur during the compression process. Understanding these losses is essential for optimizing the design and operation of centrifugal compressors to achieve maximum efficiency and performance.

The losses in a centrifugal compressor include:

1.10.1. Frictional Losses

These occur due to the friction between the flowing fluid and the compressor's parts, such as blades. The losses depend on the friction factor, length of the flow passage, and the square of the fluid velocity.

1.10.2. Incidence Losses

These occur when the direction of the relative velocity of the fluid at the inlet does not match with the inlet blade angle, causing energy loss due to the mismatch.

1.10.3. Clearance and Leakage Losses

These occur due to the necessary clearances between the impeller shaft and the casing and between the outlet periphery of the impeller eye and the casing. The leakage of gas through these clearances causes losses.

1.10.4. Slip Losses

These occur due to the inertia effect of fluid between blade passages, resulting in a component of velocity lost, known as slip.

1.10.5. Impeller Losses

These include recirculating losses due to flow reversal at the impeller exit and wake-mixing losses due to fluid flow through the passage of blades.

1.10.6. Diffusor Losses

These occur due to frictional losses in the diffused area of the diffuser, causing a positive pressure gradient and potential backflow losses.

These losses can significantly impact the performance of a centrifugal compressor, and understanding their causes is crucial for optimizing compressor design and operation. [9]

1.11. Limitations of using a compressor

By principle, the compressor is connected to two networks at different pressures, the suction (low pressure) and the discharge (high pressure). surge of a compressor occurs when the high-pressure discharge network empties into the low-pressure networks through countercurrent flow in the compressor. This phenomenon, which can have several causes, causes momentary instability in the ventilation networks (in the case where the gas is air). When the discharge network is sufficiently emptied into the suction, the compressor returns to operating conditions allowing it to restore flow in the correct direction until a new cycle of instability begins.

These large flow fluctuations thus cause surge in the network due to the violent oscillatory nature of the flow back and forth phenomenon. Each reversal of the airflow direction represents a violent shock to the compressor's kinematic chain and the main motor's power supply.

Therefore, manufacturers provide coefficients, either immediately or progressively, to account for the fatigue of elements subjected to repeated shocks. Consequences include the breaking of fins on compressors, radial force vibrations and destruction of blades, premature wear of electric motors, and bursting of ventilation network pipes. To prevent destruction, manufacturers provide pumping or flow return sensors, which cut off the main motor's general power supply.

Thus, surge is reduced and mechanical parts are less stressed. However, these sensors do not anticipate the problem. Moving towards low airflow rates, the slope of the iso-speed curve, initially negative, passes through zero, then becomes positive while leading to slight pressure variations that may be acceptable during transient operations. When these pressure fluctuations become too significant, they can rise back to the compressor inlet and create instabilities resulting in very loud noises.

This phenomenon is called surge, and operation under these conditions should be avoided. The characteristic curve of a centrifugal compressor shows the surge limit in the form of a surge line.

1.12. Sonic Blockage

we can observe on the characteristic curve an almost vertical slope, which corresponds to a maximum flow rate (sonic blockage). Physically, if the flow rate is increased, the relative velocity incidence will decrease to a minimum value. This corresponds to an obstruction in the channel where the fluid reaches the speed of sound.(see Figure 1. 8)

1.13. surge phenomenon

Pumping is a highly complex transient phenomenon that occurs under specific operating conditions. It manifests when the airflow rate drops below a certain threshold for a given rotational speed, resulting in significant periodic variations in pressure and flow at varying frequencies.(see Figure 1. 8)

This phenomenon causes a cyclic back-and-forth movement of the airflow in the opposite direction of the normal flow. There are two types of surge:

1.13.1. **Classical surge**

This type is characterized by oscillations in both pressure and flow.

1.13.2. Deep surge

In this case, the oscillations in the flow are so large that they cause a reversal of flow direction within the pressure system.

1.14. Jet and Wake flow

The laser anemometry measurements by Eckardt (1976) have confirmed the theories proposed by Dean and Senoo (1960) and Dean (1971), which suggest the presence of a low-momentum fluid accumulation zone, the wake, at the outlet of the impeller, co-existing with a region of high energy, the jet. This is depicted in.

Eckardt (1976) proposed to explain this phenomenon as the result of the interaction between the detachment of the boundary layer at the extrados (resulting from turbulence reduction due to Coriolis acceleration) and separation at the casing (due to curvature). Although the coexistence of detachment zones and jet/wake was experimentally observed by Johnson and Moore (1983), subsequent experiments by Krain (1988) demonstrated the possibility of encountering the jet/wake structure in the absence of significant detachment.(see Figure 1. 9)

The explanation commonly accepted now (Hirsch, Kang, and Pointel, 1996; Hathaway et al., 1993) attributes the jet/wake to the transport of low-momentum fluid in the boundary layers, interacting with the main flow. This structure thus emerges from the interaction between secondary and main flow.

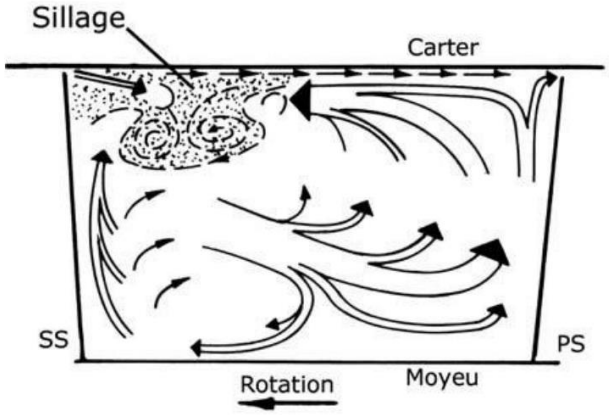

Figure 1. 10: impellers jet and Wake flow view[2]

Numerical simulations generally reproduce the jet/wake well: calculations by Casey, Dalbert, and Roth (1990) capture the progressive development of the low-momentum zone through Eckardt's (1976) impeller; results by Kang and Hirsch (1999) replicate the influence of flow rate on the position of the jet/wake, as experimentally observed by Chriss, Hathaway, and Wood (1996).

CHAPTER 2: AEROTHERMODYNAMIC MODULE

2.1. Introduction

Fluid dynamics entails studying the collective motion of many individual particles, typically molecules or atoms. This assumes that the density of the fluid is sufficiently high to treat it as a continuum. Consequently, when considered in the context of differential calculus, even the smallest element of the fluid comprises enough particles to define average velocity and kinetic energy. Thus, essential parameters such as velocity, pressure, temperature, density, and others can be specified at every point within the fluid.

The foundational equations of fluid dynamics stem from the principles of conservation, specifically the conservation of mass, momentum, and energy.

2.2. The foundational equations of fluid dynamics:

The foundational equations of fluid dynamics are based on the conservation laws of mass, momentum, and energy. These laws are derived from classical mechanics and are modified in quantum mechanics and general relativity. The key equations include:

2.2.1. The continuity equation:

This equation states that the fluid mass change rate inside a control volume must be equal to the net rate of fluid flow into the volume.

$$\frac{\partial \rho}{\partial t} + \frac{\partial \left(\rho u_i \right)}{\partial x_i} = 0 \qquad \text{(II.1)}$$

2.2.2. The momentum equation

The Navier-Stokes equations are a set of fundamental equations in fluid dynamics that describe the motion of fluids. They are based on the principle of conservation of momentum and are used to model various types of fluid flow.

$$\frac{\partial(\rho u_i)}{\partial t}\frac{\partial(\rho u_i u_j)}{\partial t} = -\frac{\partial p}{\partial x_i} + \frac{\partial t_{ij}}{\partial x_j} + s_i \qquad \text{(II.2)}$$

with:

S_i : Source term includes all volume forces (gravity, centrifugal forces, Coriolis force).

$$S_i = S_{i,cor} + S_{i,cent} = -2.\varepsilon_{ijk}.\rho.\omega_j.u_k - \varepsilon_{klm}.\rho.\omega_j.\omega_l.r_m \qquad \text{(II.3)}$$

t_{ij} : Viscous stress tensor, is expressed by the following relation:

$$t_{ij=}\delta_{ij}.\lambda.\frac{\partial u_k}{\partial x_k} + u.\left(\frac{\partial u_i}{\partial x_j} + \frac{\partial u_j}{\partial x_i}\right) = \delta_{ij}.\lambda.\frac{\partial u_k}{\partial x_k} + 2.\mu.\delta_{ij} \qquad \text{(II.4)}$$

with:

δ_{ij} : is the Kronecker symbol.

2.2.3. The energy equation

This equation describes the change in energy within a control volume and includes terms for kinetic energy, potential energy, and heat transfer.

$$\frac{\partial(\rho.h_t)}{\partial t}\frac{\partial(\rho.h_t u_j)}{\partial x_j} = \frac{\partial p}{\partial t} + \frac{\partial}{\partial x_j}.\left(K.\frac{\partial T}{\partial x_J}\right) + \frac{\partial}{\partial x_J}(t_{ij} u_j) + S_E \qquad \text{(II.5)}$$

h_t : Total energy (the sum of internal energy and kinetic energy)

S_E : Energy source term.

μ : Molecular viscosity depends on temperature.

2.2.4. perfect gas

$$PV = nRT \tag{II.6}$$

- where **P** is the pressure, **V** is the volume, **n** is the number of moles of gas, **R** is the gas constant, and **T** is the temperature in Kelvin.

2.2.5. Sutherland's law

Sutherland's law is a relationship between an ideal gas's dynamic viscosity, μ, and the absolute temperature, T. It is commonly used to model the behavior of gases and can be expressed as:

$$\mu = \mu_0 \left(\frac{T}{T_0} \right)^{\frac{3}{2}} \frac{T_0 + S}{T + S} \tag{II.7}$$

- μ is the dynamic viscosity of the gas at temperature T
- μ_0 is the dynamic viscosity of the gas at the reference temperature T_0
- T is the absolute temperature of the gas
- T_0 is the reference absolute temperature
- S is the Sutherland temperature, a constant that depends on the gas.

2.3. TURBULENCE MODELING

Turbulence modeling is a pivotal aspect within computational fluid dynamics (CFD) simulations, particularly in scenarios where turbulent flows exert significant influence. Turbulence denotes the erratic and disorderly movement of fluid particles, characterized by fluctuations in velocity, pressure, and other flow properties.

Turbulence is an inherent property of fluid flow, independent of the fluid's nature. In turbulent flow, macroscopic physical quantities such as temperature, velocity, and pressure

exhibit rapid and random variations in both space and time. Turbulence is distinguished by its high diffusivity of temperature and momentum.

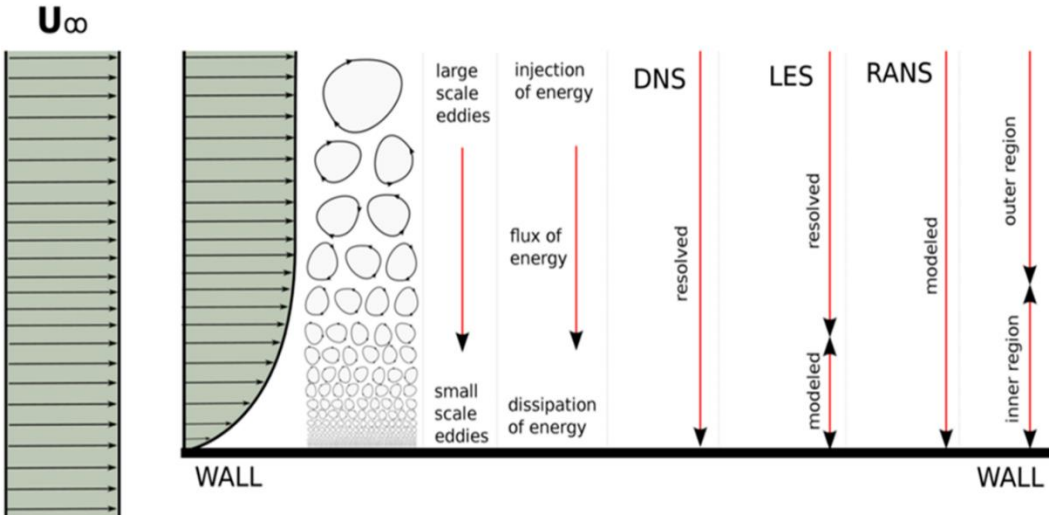

Figure 2. 1: Turbulence modeling[1]

To solve the equations governing flows with high Reynolds numbers, three approaches to simulating turbulent flows are commonly employed:

- **DNS** (**D**irect **N**umerical **S**imulation): A method for resolving all turbulent scales directly.
- **LES** (**L**arge **E**ddy **S**imulation): Focuses on simulating the larger turbulent structures.
- **RANS** (**R**eynolds-**A**veraged **N**avier-**S**tokes): Utilizes a statistical approach to turbulence simulation.

2.3.1. Direct Numerical Simulation

In this model, fluid mechanics problems are directly resolved, specifically using the three-dimensional and unsteady Navier-Stokes equations. Both the mean flow and turbulent fluctuations are computed without employing any turbulence model, necessitating a sufficiently fine mesh to capture the smallest flow fluctuations.

Indeed, the Direct Numerical Simulation (DNS) method is the most accurate among turbulent flow simulation techniques. Although computations with DNS are relatively fast compared to other methods, they require powerful computing machines and time. It's worth

noting that the most advanced DNS simulations have achieved spatial resolutions on the order of magnitude of nodes.

2.3.2. Large Eddy Simulation

Large Eddy Simulation (LES) is a technique utilized to model dissipative processes resulting from viscosity, thermal conductivity, mass diffusivity, and so forth, occurring at length scales smaller than those explicitly resolved by the mesh. Although turbulence is inherently three-dimensional and unsteady, LES enables us, through spatial filtering, to differentiate between large eddies and smaller structures, also known as microstructures. While this method provides high accuracy, it is costly in terms of computational time.

2.3.3. Reynolds-Averaged Navier-Stokes

Statistical modeling can be viewed as the coarsest level of description, involving the direct calculation of an averaged solution. This implies that all scales of turbulence are modeled. This approach, known as Reynolds-Averaged Navier-Stokes (RANS), is widely employed in industrial applications due to its low computational cost and the adequacy of approximation level with the expected results. However, it fails to highlight rare events that may occur in certain cases, such as aerodynamic instability or energy transport.

The Reynolds-averaged Navier-Stokes (RANS) equations are derived from the Navier-Stokes equations by decomposing the flow variables into their mean and fluctuating components. The laws by Reynolds and Faver, specifically, deal with the statistical treatment of turbulence.

2.3.4. Statistic Law

This approach is based on a statistical treatment of the Navier–Stokes equations, using Reynolds decomposition. When the flow is turbulent, any vector or scalar quantity can be decomposed into a mean part and a fluctuating part. This approach is valid for all steady-state or transient cases. Examples of Reynolds decomposition include:

$$U(x,t) = \overline{u(x,t)} + u'(x,t) \tag{II.8}$$

$$\phi(x,t)=\overline{\phi(x,t)}+\phi'(x,t) \tag{II.9}$$

By applying Reynolds decomposition to the variables in the continuity and Navier-Stokes equations and then taking the time average of the terms, we obtain the RANS (Reynolds-Averaged Navier-Stokes) equations.

Using mathematical tools:

- The ensemble average of a quantity, also known as the Reynolds average, is given by:

$$\overline{f(x,t)}=\underrightarrow{lim}\left(\frac{1}{N}\sum_{n=1}^{n} f(x,t)\right) \tag{II.10}$$

If the statistical quantity $\overline{f}$ is independent of time, i.e. $\overline{f(x,t)}=f(x)$ when the ensemble mean is equivalent to a time average:

$$\overline{f}(x)=\underrightarrow{lim}\frac{1}{T}\int_0^T f(x,t)\,dt \tag{II.11}$$

The average operator has the following properties:

$$\overline{c\cdot f}=c\cdot\overline{f} \tag{II.12}$$

$$\overline{f+g}=\overline{f}+\overline{g} \tag{II.13}$$

$$\overline{\overline{f}}=\overline{f} \tag{II.14}$$

$$\overline{f'}=0 \tag{II.15}$$

$$\overline{f\cdot g}=\overline{f}\cdot\overline{g} \tag{II.16}$$

$$\frac{\overline{\partial f}}{\partial\xi}=\frac{\partial\overline{f}}{\partial\xi} \tag{II.17}$$

This composition is injected into the Navier-Stokes equations, which are averaged over density and velocity:

$$\rho=\overline{\rho}+\rho' \tag{II.18}$$

$$u = \bar{u} + u' \tag{II.19}$$

$$\rho \cdot u = \bar{\rho} \cdot \bar{u} + \bar{\rho} \cdot u' + \rho' \cdot \bar{u} + \rho' \cdot u' \tag{II.20}$$

$$\overline{\rho \cdot u} = \bar{\rho} \cdot \bar{u} + \overline{\rho' \cdot u'} \tag{II.21}$$

Applying Reynolds decomposition to the compressible Navier-Stokes equations does not result in a system of equations for the mean field that is formally identical to the original equations. To avoid this problem, we use Favre decomposition, which is based on density-weighted averages.

Favre averaging is expressed as follows:

$$\tilde{\varphi} = \frac{\overline{\rho \cdot \varphi}}{\bar{\rho}} \tag{II.22}$$

The decomposition is written as:

$$\varphi = \tilde{\varphi} + \varphi'' \tag{II.23}$$

$$\overline{\rho \cdot \varphi} = \bar{\rho} \cdot \tilde{\varphi} \tag{II.24}$$

$$\overline{\rho \cdot \varphi''} = 0 \tag{II.25}$$

$$\overline{\varphi''} \neq 0 \tag{II.26}$$

2.3.4.1. The continuity equation

Due to the use of Favre averaging, the form of the continuity equation remains unchanged. Indeed, injecting Reynolds decomposition into the continuity equation (II.1)

and applying Reynolds averaging along with the linearity properties of the averaging operator to equation (II.1):

$$\overline{\frac{\partial \rho}{\partial t} + \frac{\partial (\rho u_i)}{\partial x_i}} = 0 \tag{II.27}$$

$$\frac{\partial(\overline{\rho})}{\partial t}+\frac{\overline{\partial\left(\rho u_i\right)}}{\partial x_i}=0 \tag{II.28}$$

$$\frac{\partial(\overline{\rho})}{\partial t}+\frac{\overline{\partial\left((\overline{\rho}+\rho').(\overline{u_i}+u')\right)}}{\partial x_i}=0 \tag{II.29}$$

$$\frac{\partial(\overline{\rho})}{\partial t}+\frac{\partial(\overline{\rho u_i})}{\partial x_i}+\frac{\partial(\overline{\rho' u'})}{\partial x_i}=0 \tag{II.30}$$

According to the properties of the Favre averaging operator:

$$\frac{\partial\overline{\rho}}{\partial t}+\frac{\partial\left(\overline{\rho}u_i\right)}{\partial x_i}=0 \tag{II.31}$$

2.3.4.2. The momentum equation

The same with The momentum equation, we get:

$$\frac{\partial\left(\overline{\rho}u_i\right)}{\partial t}\frac{\partial\left(\overline{\rho}u_i u_j\right)}{\partial t}=-\frac{\partial\overline{p}}{\partial x_i}+\frac{\partial(\overline{t_{ij}}+\overline{\rho u_i "u_j "})}{\partial x_j}+\overline{S_i} \tag{II.32}$$

2.3.4.3. The energy equation

As with the previous equations, Reynolds decomposition is introduced into the energy equation, which is then averaged.

$$\frac{\partial\left(\overline{\rho}.h_t\right)}{\partial t}\frac{\partial\left(\overline{\rho}.h_t u_j\right)}{\partial x_j}=\frac{\partial\overline{p}}{\partial t}+\frac{\partial}{\partial x_j}.\begin{pmatrix}-\overline{q_j}-\overline{\rho.h_t "u_j "}+\overline{t_{ij}u_{ij}"}\\-\frac{1}{2}.\overline{\rho u_i u_i "u_j "}+(\overline{t_{ij}}+\overline{\rho}.\tau_{ij})u_i\end{pmatrix}+\overline{S_E} \tag{II.33}$$

2.4. The turbulence models:

2.4.1. The K − ε model:

The K − ε turbulence model is likely the most widely employed two-equation eddy-viscosity model. It is based on the solution of equations for the turbulent kinetic energy K and the turbulent dissipation rate ε

The turbulent kinetic energy equation:

$$\frac{\partial\left(\overline{\rho}.k\right)}{\partial t}\frac{\partial}{\partial x_j}(\overline{\rho}.u_j.k)=\frac{\partial}{\partial x_j}\left[(\mu+\frac{\mu_T}{\sigma_k})\frac{\partial k}{\partial x_j}\right]+P_K-\overline{\rho}.\varepsilon \qquad \text{(II.34)}$$

The dissipation rate equation:

$$\frac{\partial\left(\overline{\rho}.\varepsilon\right)}{\partial t}\frac{\partial}{\partial x_j}(\overline{\rho}.u_j.\varepsilon)=\frac{\partial}{\partial x_j}\left[(\mu+\frac{\mu_T}{\sigma_\varepsilon})\frac{\partial \varepsilon}{\partial x_j}\right]+\frac{\varepsilon}{k}(C_{\varepsilon 1}.P_K.C_{\varepsilon 2}.\overline{\rho}.\varepsilon) \qquad \text{(II.35)}$$

With

P_K : The production of turbulence due to viscous forces and buoyancy.

Table 2. 1: The constants of the Standard Model in ANSYS CFX 2023 R2

C_μ	C_{s1}	$C_{\varepsilon 2}$	σ_k	σ_ω
0.09	1.44	1.92	1.0	1.3

2.4.2. The K ω model

This turbulence model employs two transport equations: one for dissipation ε and the other, proposed by Wilcox, which utilizes the turbulence frequency ω.

The turbulent kinetic energy equation:

$$\frac{\partial\left(\overline{\rho}.k\right)}{\partial t}\frac{\partial}{\partial x_j}(\overline{\rho}.u_j.k)=\frac{\partial}{\partial x_j}\left[(\mu+\frac{\mu_T}{\sigma_{k1}})\frac{\partial k}{\partial x_j}\right]+P_K-\beta.\overline{\rho}.k.\omega \qquad \text{(II.36)}$$

The turbulent frequency equation:

$$\frac{\partial\left(\overline{\rho}.\omega\right)}{\partial t}\frac{\partial}{\partial x_j}(\overline{\rho}.u_j.\omega)=\frac{\partial}{\partial x_j}\left[(\mu+\frac{\mu_T}{\sigma_{\omega 1}})\frac{\partial\omega}{\partial x_j}\right]+\alpha_1.\frac{\omega}{k}.P_k-\beta_1.\overline{\rho}.\omega^2 \qquad \text{(II.37)}$$

Table 2. 2: The constants of the K-ω model in ANSYS CFX 2023 R2

β^1	α_1	β_1	σ_k	σ_ω
0.09	5/9	0.075	2.0	2.0

This turbulence model has the advantage of analyzing the flow near the walls.

2.4.3. K-ω SST model

The "Shear Stress Transport" (SST) turbulence model is derived from the Baseline (BSL) model.

In 1994, Menter utilized the advantages of both the K-epsilon and k-omega models to develop a hybrid version known as the SST model. This model is more versatile because it uses the K-epsilon formulation near walls and the K-omega formulation in free-flow regions (away from walls).

The purpose of the SST model is to employ the K-epsilon model in the wake and the k-omega model in the boundary layer and the rest of the domain.

The SST model is a combination of these two models, expressed through a transition function given by:

$$\text{S.S.T} = \text{F(k-}\omega\text{)} + \text{(1- F)(k-}\varepsilon\text{)} \qquad \text{(II.38)}$$

The two turbulence models, Baseline (BSL) and SST are identical, but the SST model introduces a new expression for turbulent kinematic viscosity to better predict flow separation.

Transportation equations:

- The turbulent kinetic energy transport equation:

$$\frac{\partial\left(\overline{\rho}.\omega\right)}{\partial t}\frac{\partial}{\partial x_j}(\overline{\rho}.u_j.\omega)=\frac{\partial}{\partial x_j}\left[(\mu+\frac{\mu_T}{\sigma_{\omega 2}})\frac{\partial\omega}{\partial x_j}\right]+\left(1-F_1\right).2.\overline{\rho}.\frac{\partial k}{\sigma_{\omega 2}.\omega.\partial x_j}.\frac{\partial\omega}{\partial x_j}+\alpha_3.\frac{\omega}{k}.P_k-\beta_3.\overline{\rho}.\omega^2 \quad \text{(II.39)}$$

- The frequency transport equation:

$$\frac{\partial\left(\overline{\rho}.k\right)}{\partial t}\frac{\partial}{\partial x_j}(\overline{\rho}.u_j.k)=\frac{\partial}{\partial x_j}\left[(\mu+\frac{\mu_T}{\sigma_{k2}})\frac{\partial k}{\partial x_j}\right]+P_K-\beta'.\overline{\rho}.k.\omega \quad \text{(II.40)}$$

2.5. Study of Y+

Y+ is a dimensionless distance. It is often used to describe how coarse or fine a mesh is for a particular flow model. It is important in turbulence modeling to determine the appropriate cell size near the walls of the domain. The wall laws of the turbulence model impose restrictions on the Y+ value at the wall. The SST model requires a Y+ value between approximately 0 and 5. Faster flow near the wall will produce higher Y+ values, so the grid size near the wall needs to be reduced.

$$\Delta y = L.\Delta y^{+}.\sqrt{80}.R_{ex}^{\frac{1}{14}}.\frac{1}{R_{eL}} \quad \text{(II.41)}$$

The Y+ coefficient is a very important parameter in fluid flow modeling using CFD (Computational Fluid Dynamics). It is used to determine the accuracy of numerical calculations in fluid simulations. A well-chosen Y+ value provides more accurate and reliable results, especially for turbulent flows. Therefore, selecting the Y+ coefficient is crucial for the precision of numerical calculations in CFD and must be done carefully to ensure accurate and reliable simulation results. The following captures show the range of Y+ variation on the blade surface, the hub, and the casing.

2.6. Boundary layer

The boundary layer is a fundamental concept in fluid dynamics that describes the thin layer of fluid near a solid surface. As fluid flows over a solid boundary, such as the surface of an aircraft wing or the wall of a pipe, the adjacent layer of fluid experiences a gradual transition from the fast-moving outer flow to the slower-moving flow near the surface.

The boundary layer can be divided into two main types:

2.6.1. Laminar Boundary Layer

The flow inside a laminar boundary layer is smooth and takes place in layers. Each layer slides past the adjacent layers and any exchange of mass or momentum takes place only between these layers on a microscopic scale. A laminar boundary layer is formed when the Reynolds number is low.

2.6.2. Turbulent Boundary Layer

In a turbulent boundary layer, the flow is characterized by chaotic changes in pressure and flow velocity. The flow is no longer smooth and the exchange of mass and momentum takes place on a much larger scale compared to laminar flow. Turbulent boundary layers are formed at higher Reynolds numbers.

The boundary layer plays a crucial role in determining the behavior and characteristics of fluid flow. It is responsible for a considerable amount of drag on the surface. The thickness of the boundary layer varies inversely with the Reynolds number. The boundary layer can separate from the surface, leading to the formation of eddies and vortices in the wake.

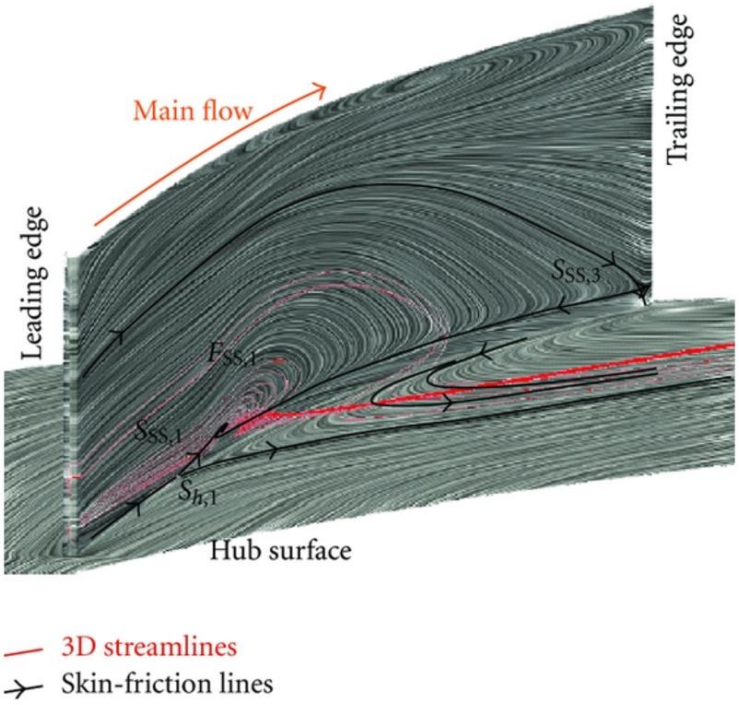

Figure 2. 2: Presentation of streamlines[2]

2.7. The stability of the boundary layer

The stability of the boundary layer in turbomachinery is a critical factor influencing performance. Research indicates that the boundary layer transitional flow in gas turbines is influenced by various factors such as Kelvin-Helmholtz instability, separated shear layers, and the impact of freestream turbulence levels. Understanding the behavior of the boundary layer is crucial due to the interaction between stationary and rotating blade rows, which can lead to flow separation and affect performance. Various studies have focused on transition mechanisms in turbomachinery boundary layer flows, highlighting the importance of models like Direct Eddy Simulation (DES) or Large Eddy Simulation (LES) for accurate predictions. Additionally, analyzing the stability of the boundary layer is essential for assessing flow separation control capabilities in low-pressure turbines, with studies focusing on the stability characteristics of the boundary layer over different configurations to enhance performance and efficiency

CHAPTER 3: SIMULATION

3.1. Introduction

With the development of numerical simulation tools and the increasing power of computing resources, there is a significant number of dedicated computational codes for handling complex three-dimensional problems, especially in the fields of fluid mechanics and turbomachinery. Some of the most well-known computational codes include ANSYS CFX, GAMBIT, FLUENT, etc. The software utilized in this study to numerically model compressible flow in a centrifugal compressor is ANSYS-CFX.

3.2. What Is ANSYS CFX

Ansys CFX is a computational fluid dynamics (CFD) software tool that allows you to design and optimize turbomachinery, including pumps, turbines, compressors, fans, and other rotating machinery. CFX is known for being the gold standard in accuracy for turbomachinery with extensive industry validation.

Like many software packages, CFX includes several tools and modules for:

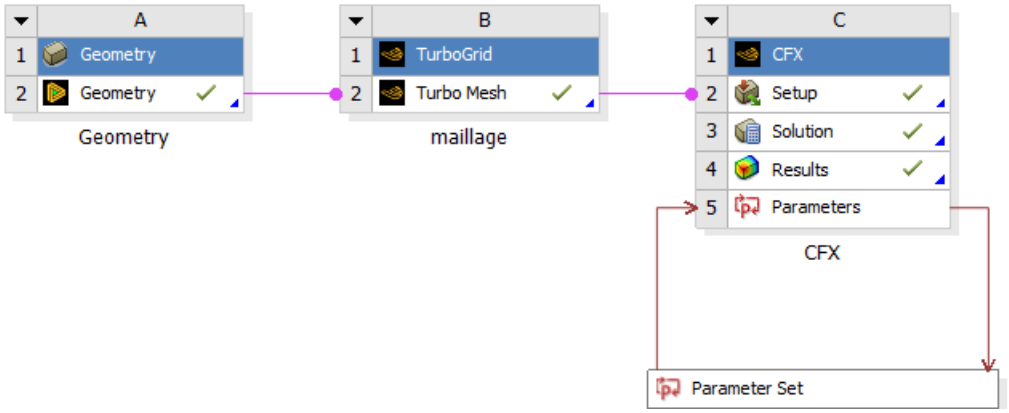

Figure 3. 1: the program organigram

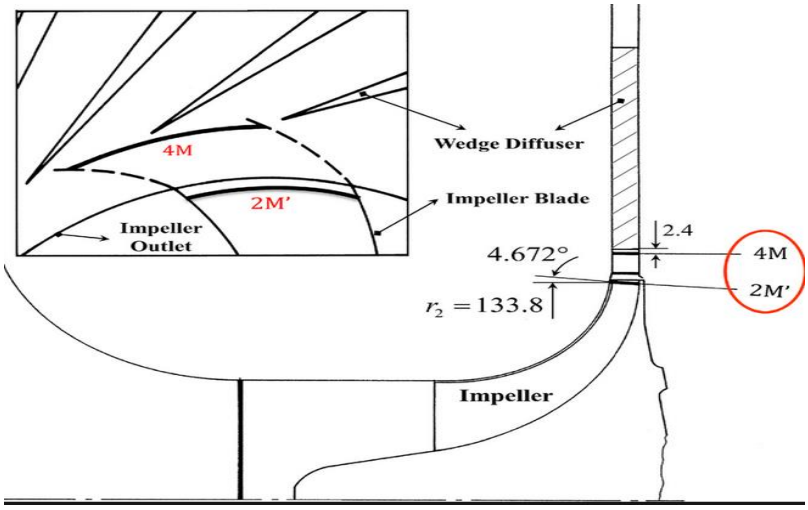

Figure 3. 2: the geometry [9]

3.2.1. ANSYS CFX BladeGen

The initial step involves defining the geometry of the centrifugal compressor impeller and diffuser using CFX-BladeGen. This is a three-dimensional tool designed to rapidly create geometry, specifically tailored for turbomachinery applications, including centrifugal or axial compressors, pumps, fans, turbines, etc. For our study, we imported files in [.dat] format containing coordinates of the impeller, hub, and compressor casing geometry points.

These data files are exported from BladeGen and represent the exact geometry of the compressor under investigation.

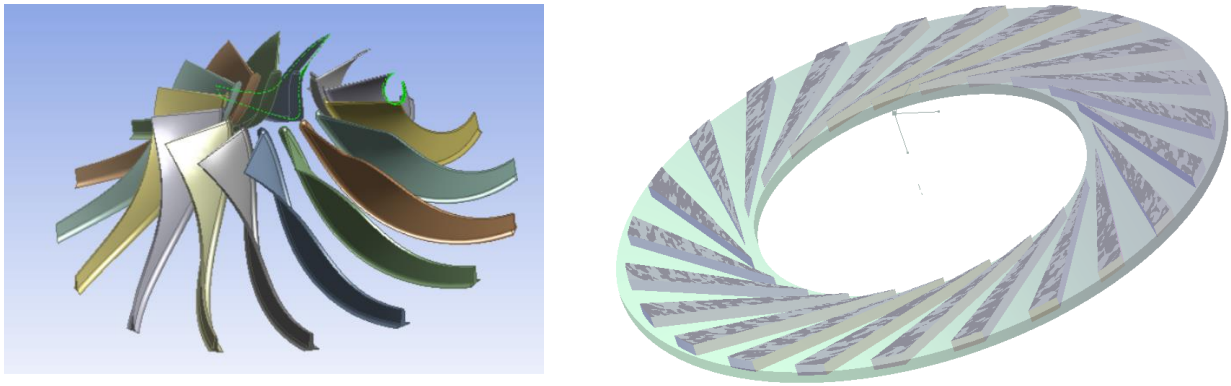

Figure 3. 3: the compressor stage

3.2.2. ANSYS CFX TurboGrid

This tool enables the generation of a structured mesh suitable for various machine types. However, there is no precise rule to achieve a good mesh quality for certain complex geometries, such as the centrifugal compressor impeller. Meshing a structure is easier using a multi-block geometry, which involves dividing the computational domains into several compartments of simple geometric shapes and meshing them separately.

- Advantages:

✓ Economical in terms of element count.

✓ Reduces the risk of numerical errors and ensures relatively fast convergence in calculations.

- Disadvantages:

✓ For complex geometries like the centrifugal compressor impeller, meshing using this technique is difficult to generate and results in poor quality.

Those are the factors used to generate our mesh which is modified using 'Mesh data'

To improve the mesh quality and precision of the boundary layer we use 'passage'

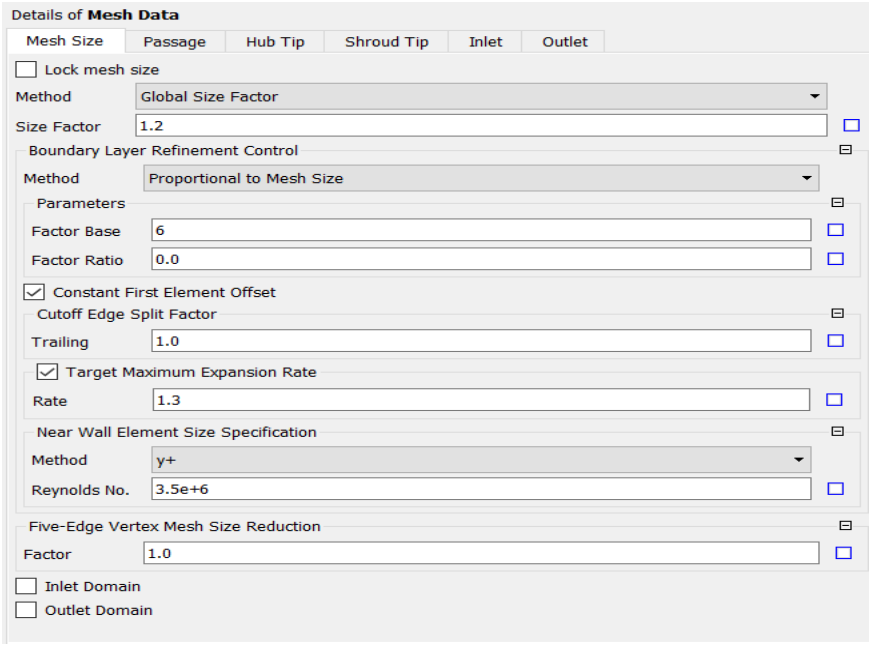

Figure 3. 4: the mesh parameter -Mesh Size-

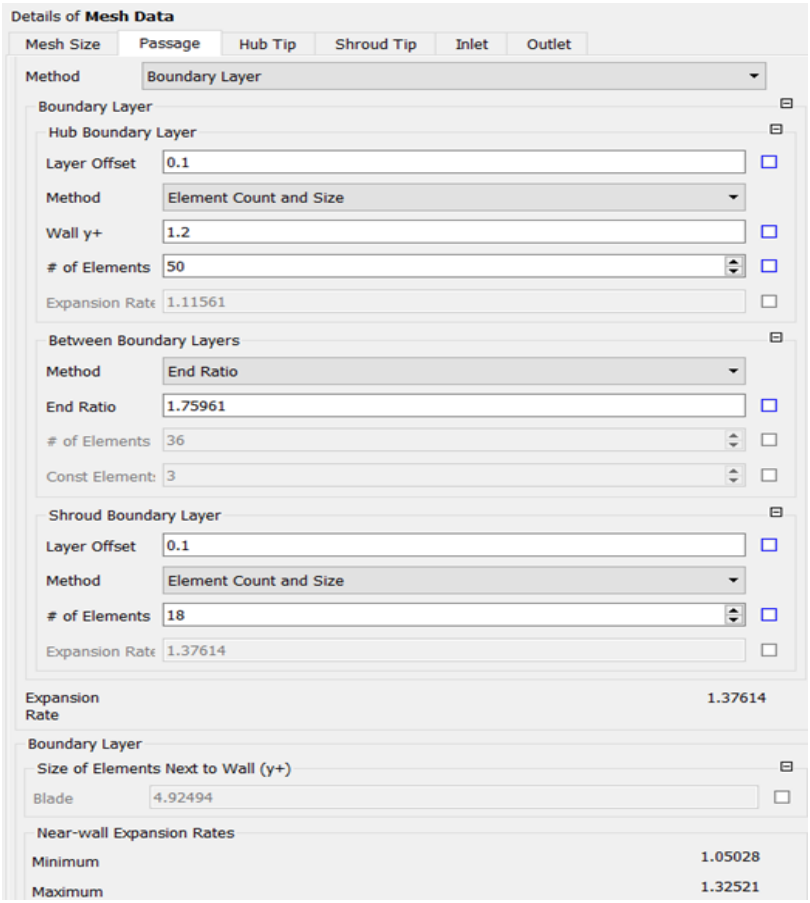

Figure 3. 5: the mesh parameter Passage

Mesh Size:

In the mesh data configuration for ANSYS, the mesh size parameters are critical for defining the resolution and quality of the computational grid. The settings include options such as the method for determining the mesh size, with the "Global Size Factor" method selected in this example.

The size factor is set to 1.2, which scales the overall mesh size. Boundary layer refinement is controlled proportionally to the mesh size with specific parameters to ensure an accurate representation of the boundary layer. Other options, such as constant first element offset, cutoff edge split factor, and maximum expansion rate, help optimize the mesh for better simulation accuracy and efficiency. Additionally, near-wall element size specification uses a y+ method with a Reynolds number of 3.5e+6, indicating the level of refinement required near wall boundaries to capture flow details accurately.

Boundary Layer -Passage-

The mesh data configuration for the boundary layer involves several key parameters to ensure accurate simulation of fluid flow near surfaces. The hub boundary layer settings include a layer offset of 0.1, using the "Element Count and Size" method with a wall y+ value of 1.2 and 50 elements.

The space between boundary layers is controlled by an end ratio method with an end ratio of 1.75961 and 36 elements. For the shroud boundary layer, the layer offset is also 0.1 with 18 elements specified. The overall expansion rate for the mesh is 1.37614, and near-wall expansion rates are monitored to maintain accuracy.

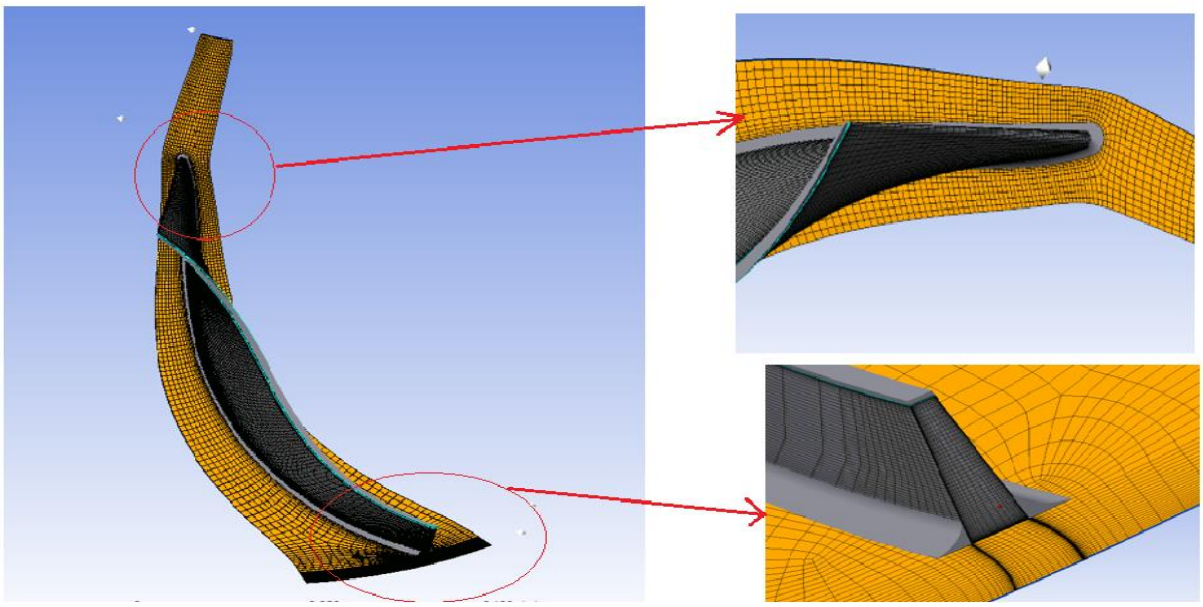

Figure 3. 6: the impeller's blade mesh

We generally have bad Y+ in the blade edge outlet so we raise the element number and

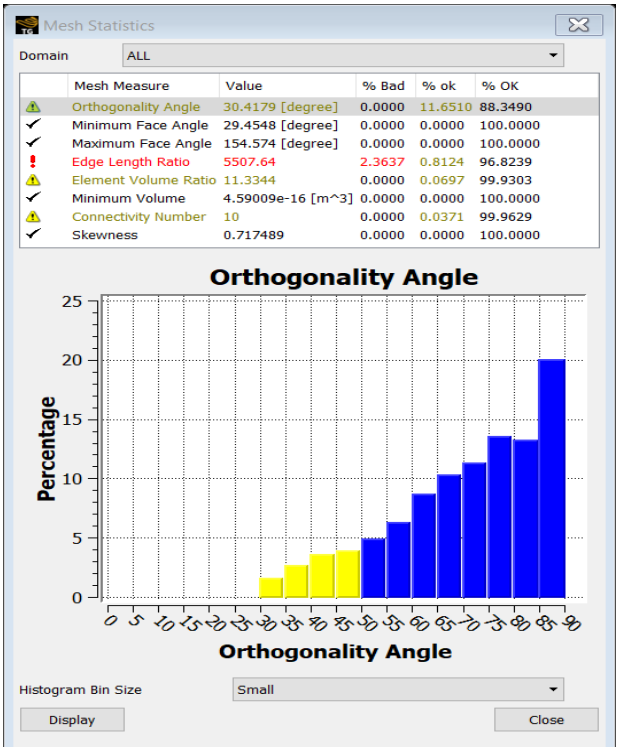

Orthogonal Quality mesh metrics spectrum:

Unacceptable	Bad	Acceptable	Good	Very good	Excellent
0-0.001	0.001-0.14	0.15-0.20	0.20-0.69	0.70-0.95	0.95-1.00

Figure 3. 7: the impeller's mesh statistics. (We see that our mesh is in the good orthogonal quality mesh)

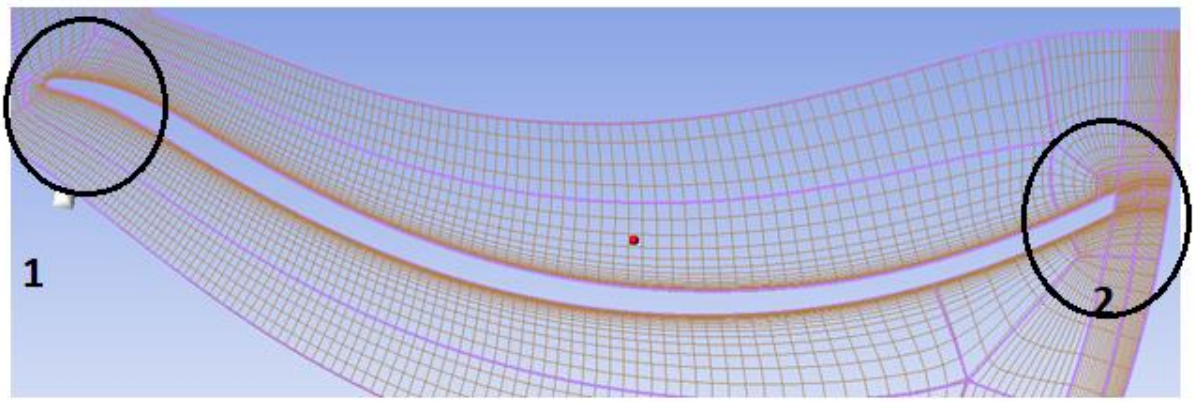

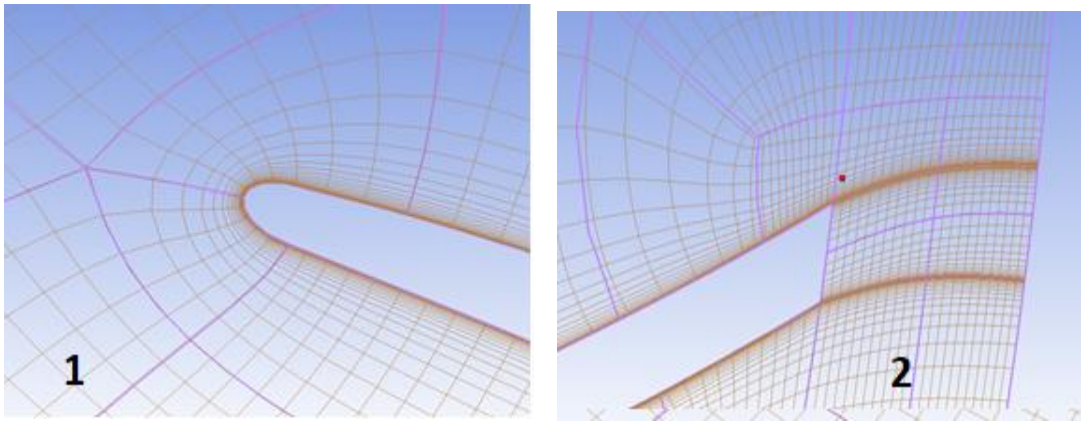

Figure 3. 8: Typology set

To create a good mesh, we have mesh zonal types that give us an optimizing form such as:

Mesh type C: blade inlet, Mesh type H: blade outlet, and mesh type O around the blade

We have the same types for the diffuser blade except the blade inlet is type H.

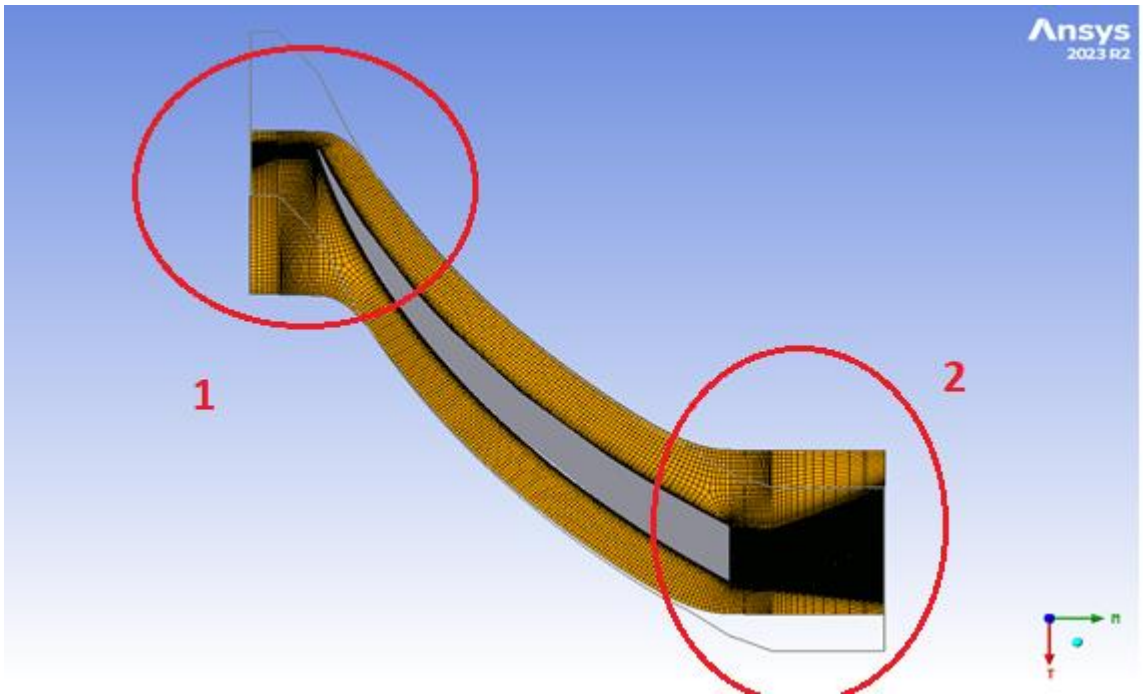

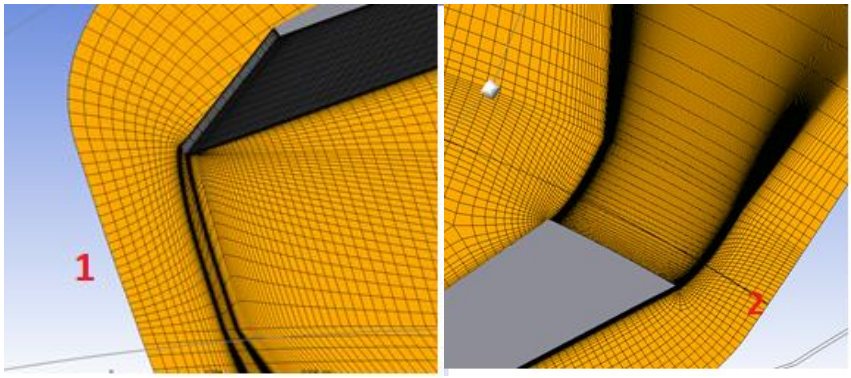

Figure 3. 9: the diffuser's mesh

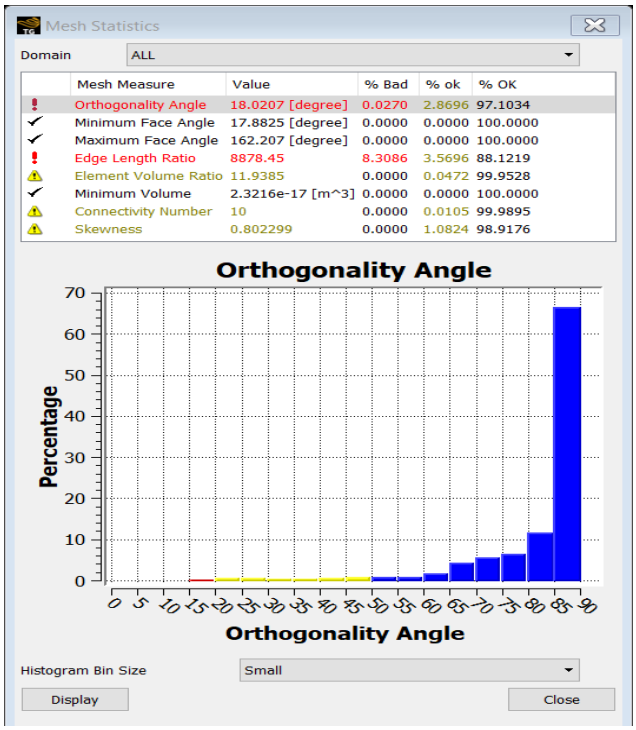

Figure 3. 10: the diffuser's mesh statistics

We see that our major percentage is in the perfect area, with a little weak percentage, so we can negligée it

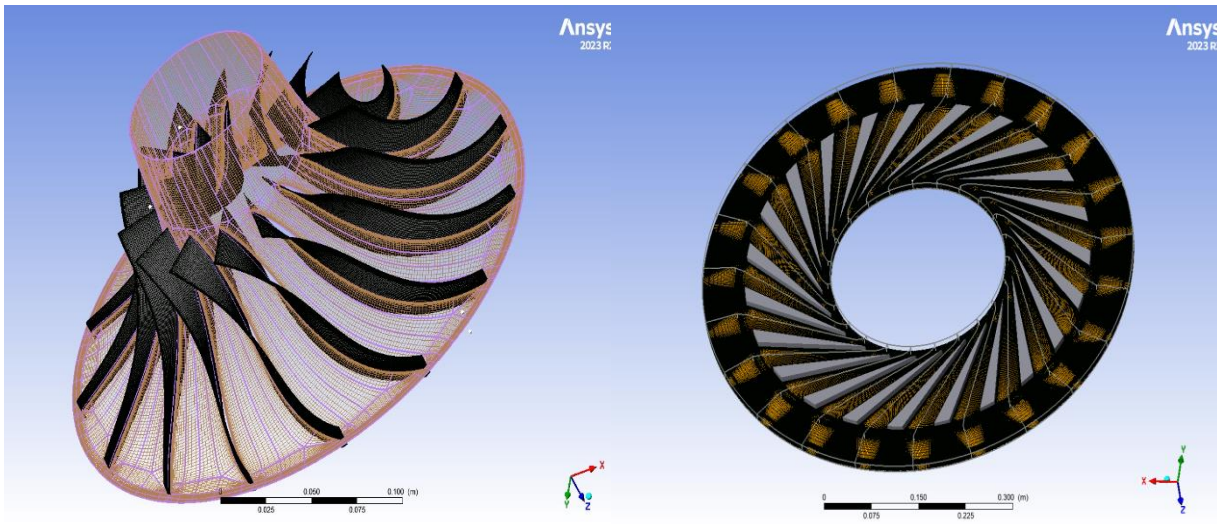

Figure 3. 11: impeller and diffuser mesh

3.2.3. The Pre-Processing Module (CFX - Pre-Processor)

In this module, boundary and initial conditions corresponding to flow regimes are defined, followed by the selection of the numerical scheme, specifying the number of iterations, convergence criteria, and fluid properties. The computational domain consists of two meshes: one for the impeller and one for the diffuser. The impeller/diffuser interface is simulated using a smooth diffuser attached to the impeller.

Considering that there are three different interface options available in ANSYS CFX - TASCflow:

- Frozen Rotor Type

This option allows modeling of the flow for a given relative position between the impeller and the diffuser. It is suitable for quasi-steady calculations when the flow velocity is relatively high compared to the machine's speed.

- Blade-to-Blade (Stage) Type

The calculation is initiated for two rows of blades simultaneously, enabling the transition from relative to absolute reference frames by calculating the circumferential flow average. This type is also employed when seeking a stationary solution in each reference frame.

- Periodic Type

This type is utilized for unsteady calculation of a sliding interface, enabling flow calculation at different positions of the interface.

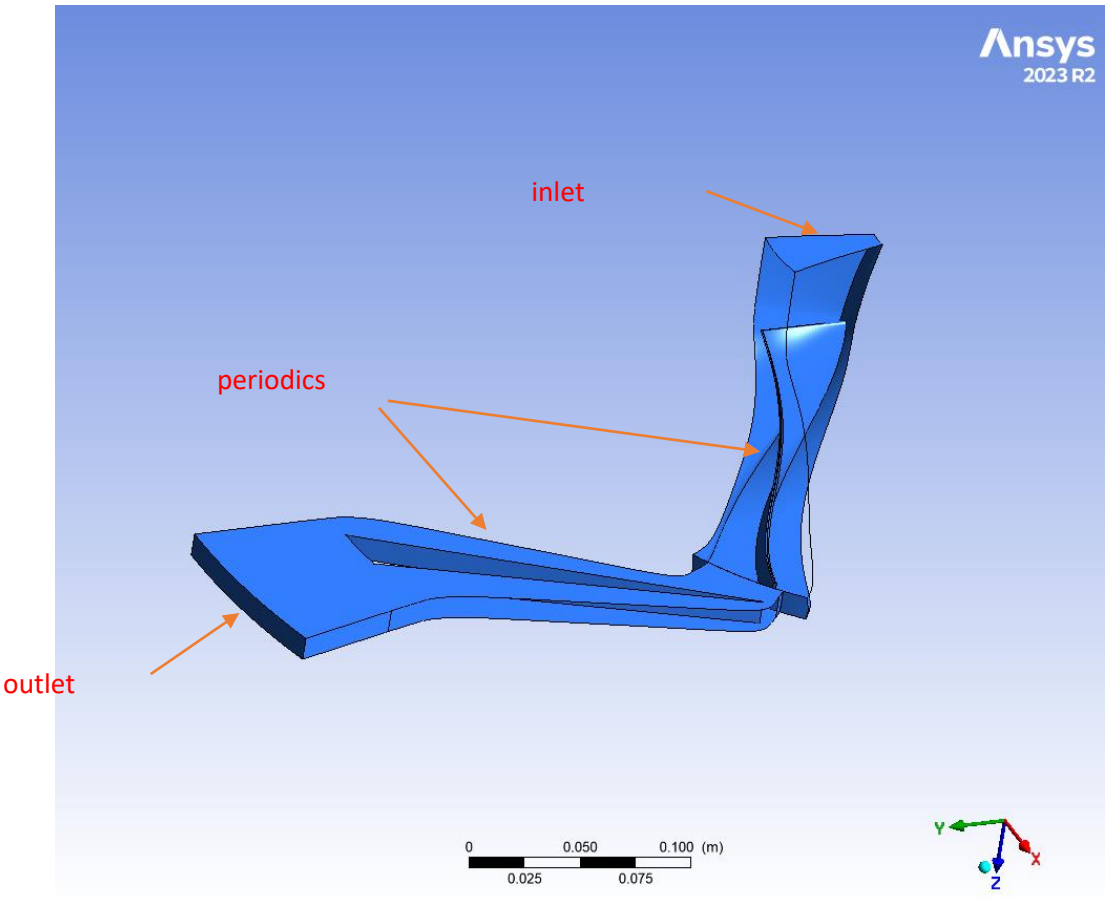

Figure 3. 12: The rotor and diffuser calculation domain

Basic Settings

- ✓ Machine Type: Centrifugal Compressor
- ✓ Rotation Axis: **z**

Component type R1

- ✓ Type: **Rotating**
- ✓ Value: **28541 [RPM]**
- ✓ Tip clearance at shroud: **yes**

Component type S1

- ✓ Type: **stationary**

Physics Definition

- ✓ Fluid: **Air Ideal Gas**
- ✓ Analysis Type: **Steady State**
- ✓ Model Data:
  - ❖ Reference Pressure: **0 [bar]**
  - ❖ Heat Transfer: **Total Energy**
  - ❖ Wall Function: **Automatic, High speed (compressible) Wall Heat, Transfer Model**
  - ❖ Turbulence: **Shear Stress Transport**
- ✓ Inflow/Outflow boundary templates: **P-total inlet P-static outlet**
- ✓ Inflow:
  - ❖ P-total = **0.6 [bar]**
  - ❖ T-total = **296 [K]**
  - ❖ Flow Direction: **Normal to the boundary**
- ✓ Outflow:
  - ❖ P-static = **BP [Variable Parameter]**
- ✓ Solver Parameters:
  - ❖ Advection scheme: **High-Resolution**
  - ❖ Convergence control: **Auto timescale**
  - ❖ Time Scale option: **Conservative**

Solver Control

- ✓ Advection Scheme: **High Resolution**

- ✓ Turbulence Numeric: **High Resolution**
- ✓ Convergence Control:
  - ❖ Min. Iterations = **1**
  - ❖ Max. Iterations = **1000**
- ✓ Fluid Timescale Control:
  - ❖ Max. timescale = **1e-5**
- ✓ Convergence Criteria:
  - ❖ Residual Type: **MAX**
  - ❖ Residual Target: **0.00001**

3.2.3.1. Discretization of the advection term

To complete the discretization of the advection term, the variable Φ_{ip} must be approximated in terms of the nodal values of Φ (discrete).

The discretization of the transient diffusion and source terms does not pose any problem, meaning that the variable Φ will simply be derived from a calculation scheme. However, for the convection term, the ANSYS CFX code offers a (hybrid) discretization scheme, in which the variable Φ_{ip} must be approximated.

The term of the nodal values of Φ in the convection, schemes can be written as:

$$\Phi_{ip} = \Phi_{up} + \beta.\nabla\Phi.\Delta\vec{r} \qquad \textbf{(III.1)}$$

Where Φ_{up} and $\nabla\Phi$ represent the variable at the node and its gradient, and $\Delta\vec{r}$ is the vector that connects the upstream node to the node (ip).

This equation **(III.1)** reflects the fact that the solution at point (ip) is equal to the upstream point (indexed as (up) for upwind) plus a second-order term multiplied by a corrective factor β used to correct the effects of numerical diffusion.

The factor β varies between zero and one. The choice of β and $\nabla\Phi$ leads to different discretization schemes.

3.2.3.2. High-resolution diagram

It's a high-resolution scheme. The ANSYS CFX software automatically calculates the value of the factor β, which is very close to 1, and assumes that $\nabla\Phi$ is equal to the gradient within the control volume of the upstream node.

3.2.3.3. Speed-pressure coupling

For determining the various flow parameters (velocity U, V, W, and pressure P), a staggered mesh is used, which in turn employs four meshes. In the ANSYS CFX software, a Co-located (Non-staggered) mesh arrangement is utilized, ensuring that the control volumes are identical for all transport equations. Patankar, Rhie, and Chow proposed a mass flux discretization technique to avoid velocity-pressure coupling, which was later modified by Majundar to ensure that the solution in the steady state does not depend on the time step.

A similar strategy is adopted in the ANSYS CFX code by applying a momentum-like equation at each integration point. The expression for the advection velocity (mass transport) at each integration point is given by:

$$U_{i,ip} = \overline{U_{i,ip}} + f_{ip}.\left(\frac{\partial p}{\partial x_i}\bigg|_{ip} - \frac{\overline{\partial p}}{\partial x_i}\bigg|_{ip}\right) - C_{ip}.f_{ip}.(U_{ip}^{0} - \overline{U_{ip}^{0}}) \quad \textbf{(III.2)}$$

$$f_{ip} = \frac{d_{ip}}{1 - C_{ip}.d_{ip}} \quad \textbf{(III.3)}$$

$$d_{ip} = \frac{-V}{A} \quad \textbf{(III.4)}$$

Where (A) represents the central coefficient approximation of the dynamic equation, excluding the transient term.

$$C_{ip} = \frac{\rho}{\Delta t} \quad \textbf{(III.5)}$$

This technique saves both memory space and computation time.

Pressure boundary condition at the inlet: using this condition, we know the pressure at the inlet and we are searching for the corresponding flow velocity and the imposed total pressure for a compressible flow through the following relation:

$$P_t = P_s.(1+\frac{\gamma-1}{2}M^2)^{\frac{\gamma}{\gamma-1}} \quad \textbf{(III.6)}$$

Total inlet temperature

$$T_t = T_s.(1+\frac{\gamma-1}{2}M^2) \quad \textbf{(III.7)}$$

3.2.4. Solution of linear equations

To solve the discretized and linearized system of equations, ANSYS CFX employs a method called the Multigrid (M.G) with Incomplete Lower-Upper (ILU) factorization acceleration. It's an iterative method where the exact solution is approximated by a discrete solution over several iterations. The system of equations is expressed in matrix form as follows:

$$[A].[\phi] = [b] \quad \textbf{(III.8)}$$

Where $[A]$ is the coefficient matrix, $[\phi]$ is the solution vector, and $[b]$ is the second member vector.

The algebraic system above can be iteratively solved by starting with an approximate solution ϕ^n that needs to be improved by a correction ϕ' to provide a better solution ϕ^{n+1}, as follows:

$$\phi^{n+1} = \phi^n + \phi' \quad \textbf{(III.9)}$$

Where ϕ' represents a solution.

$$A'.\phi' = r^n \quad \textbf{(III.10)}$$

With r^n being the residual value obtained from the following equation:

$$r^n = b - A.\phi^n \quad \textbf{(III.11)}$$

The repeated application of this algorithm enables obtaining a solution with the desired accuracy.

3.2.4.1. Residual normalization procedure

The residual vector [r] is calculated as an imbalance in the linearized discretized system of equations. The raw residuals (residual vectors) are then normalized to control the solution and achieve a convergence criterion.

For each variable solution ϕ, the normalized residual is generally given by the following relation:

$$[\vec{r_\phi}] = \frac{[r_\phi]}{a_p . \Delta\phi} \quad \textbf{(III.12)}$$

Where:

r_ϕ is the first imbalance within the control volume.

a_p is a representative coefficient of the control volume.

$\Delta\phi$ is a range of values representative of the variable ϕ in the computational domain.

The exact calculation of a_p and $\Delta\phi$ is not straightforward because:

1 .Normalized residuals are independent of the choice of time step and also for the initial estimation.

2 .For multiphase flows, the volume fraction is considered.

Residuals of the variables utilize components of velocity, mass, turbulence coefficient k, ε and the volume fraction $a_{p,v}$.

3.2.5. Summary of procedures and all required steps to follow to arrive at the solution

1 .All variable values are estimated at every point of the mesh, corresponding to the imposed initial values.

2 .The coefficients (a_i) of the equations are calculated.

3 .With the coefficients set, a linear solver solves the system of equations using an iterative technique.

4 .Regarding the iteration step, there are two cases:

a) For non-steady-state conditions, the physical time step is used.

b) For steady-state conditions, a time step that accelerates convergence is used, estimated based on flow characteristics. If the convergence criterion is met, the obtained values are solutions.

3.2.6. Simulation assumptions

The assumptions for studying the compressible flow of a centrifugal compressor stage are:

- ✓ The flow regime is steady-state.
- ✓ The fluid is compressible.
- ✓ The flow is three-dimensional.
- ✓ The thermodynamic properties of the fluid are assumed to be those of an ideal gas.
- ✓ The heat source term is zero.
- ✓ External volume forces are negligible.

3.2.7. The Solver Module

This module performs the fundamental calculations to solve the equations of the given problem. The Solver module is configured as follows:

- Solver parameters: "**Intel MPI Local Parallel**" is selected to define the number of processors and the distribution of calculations (either parallel or serial) depending on the type and performance of our computing station.
- How the calculations are executed is identified, with "Initial conditions" chosen so that each calculation is independent.

In our study we need a powerful PC performance, For our case with the following ECU performance:

Processor: 13th Gen Intel (R) Core (TM) i9-13900K / 3.00 GHz

RAM: 128 Go (128 Go utilizable)

3.2.8. The Post-Processing Module

This graphical tool enables the processing and visualization of results, including iso-surface contours, streamlines, pressure fields, etc. Results can be exported in numerical form or as animations, among other formats.

Within this module, the pressure report is configured along with the isentropic efficiency as OUTPUT parameters based on the variables displayed in the report.

CHAPTER 4: RESULT

4.1. Introduction:

In this chapter, we present the results obtained through numerical simulation and compare them with experimental results for the centrifugal compressor. Additionally, we validate these results against other studies conducted in this field.

In the first part of this chapter, we obtained results through numerical simulation using the **ANSYS CFX R2 2023** code for the isolated compressor and analyzed the aerothermodynamic parameters at a nominal flow rate. Furthermore, we also studied the influence of clearance on the centrifugal compressor impeller.

4.2. Validation of results and mesh sensitivity:

To compare the experimental results with the numerical results obtained for the variation of the following parameters: total pressure ratio, static pressure ratio, total isentropic efficiency, and power.

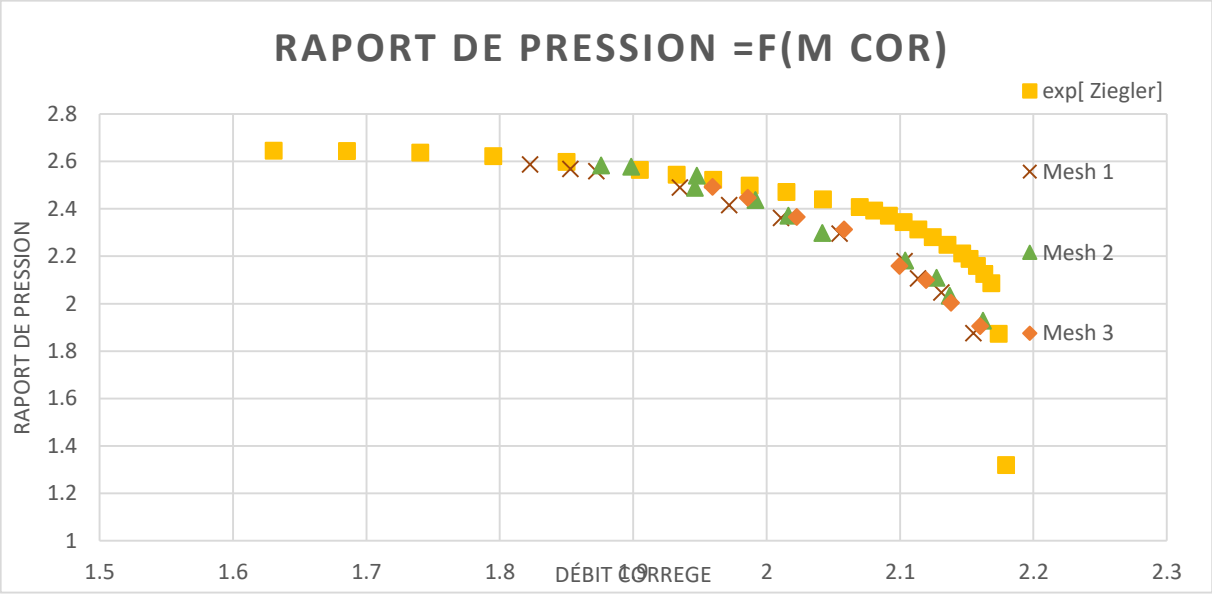

Figure 4. 1: the chart shows the results of the experimental with the different CFD's element numbers for pressure ratio

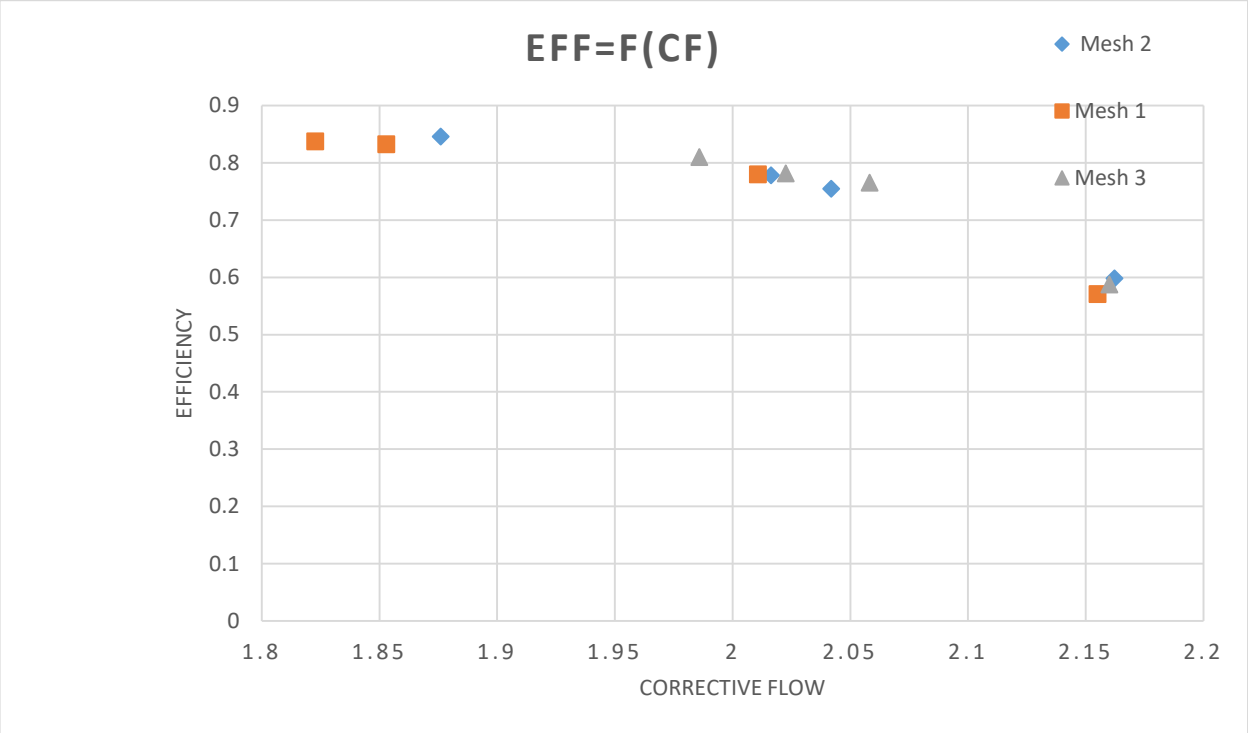

Figure 4. 2: the chart shows the results of the experimental with the different CFD's element number for efficiency

Table 4. 1: mesh element number

	Mesh 1 x10e6	Mesh 2 x10e6	Mesh 3 x10e6
Number des elements	0.8	1.8	2.6

In those charts, we present the experimental results with the different CFD mesh results.

We chose mesh 2 because it is more correspondent to the experimental.

4.2. Y+ variation

This figure shows us the Y+ variation distribution on the hub and the shroud of our centrifugal compressor stage

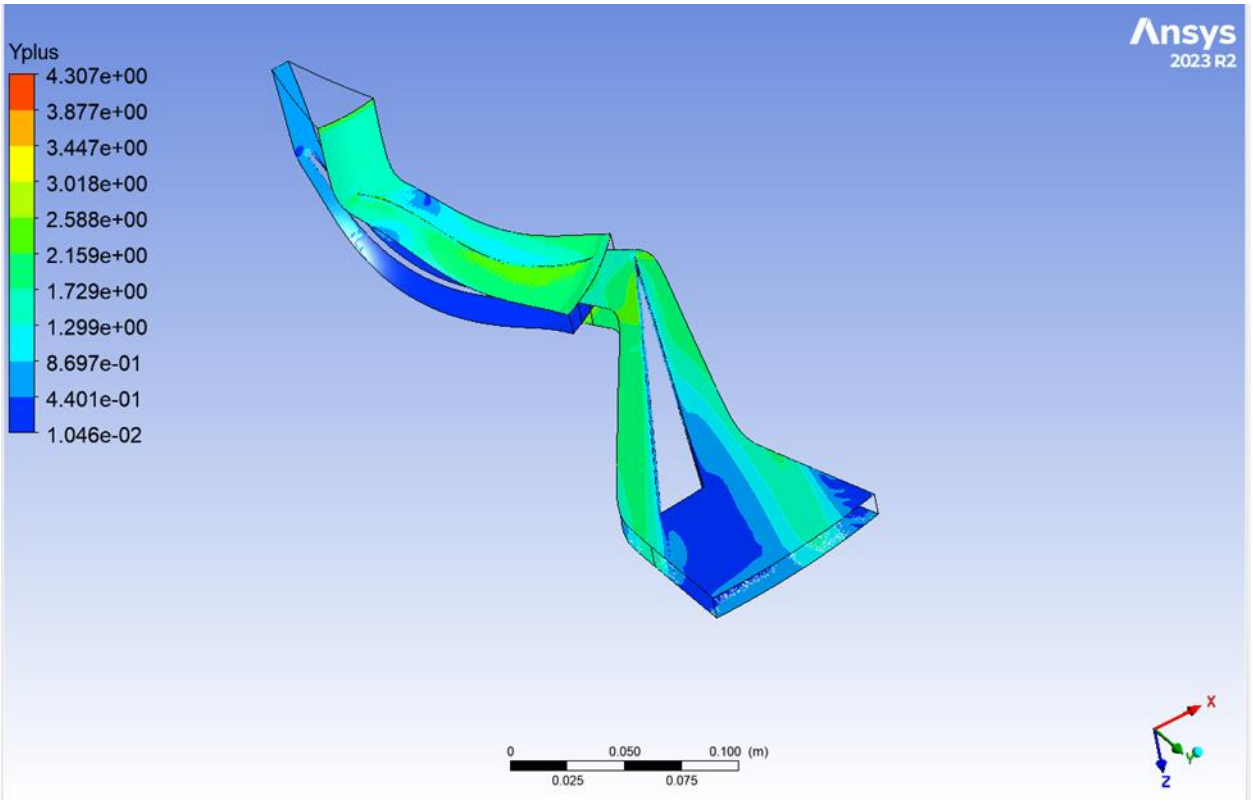

Figure 4. 3: The Y+ hub and shroud distribution

4.3. aerothermodynamics parameter

The figures below will show us the different aerothermodynamics parameters in different plans with 2.016 kg/s of corrective flow and a speed of 28541 RPM.

4.3.2. Meridional Plane:

Static and total pressure:

This figure shows us the variation of Total and static pressure on the impeller and diffuser for the meridional plane.

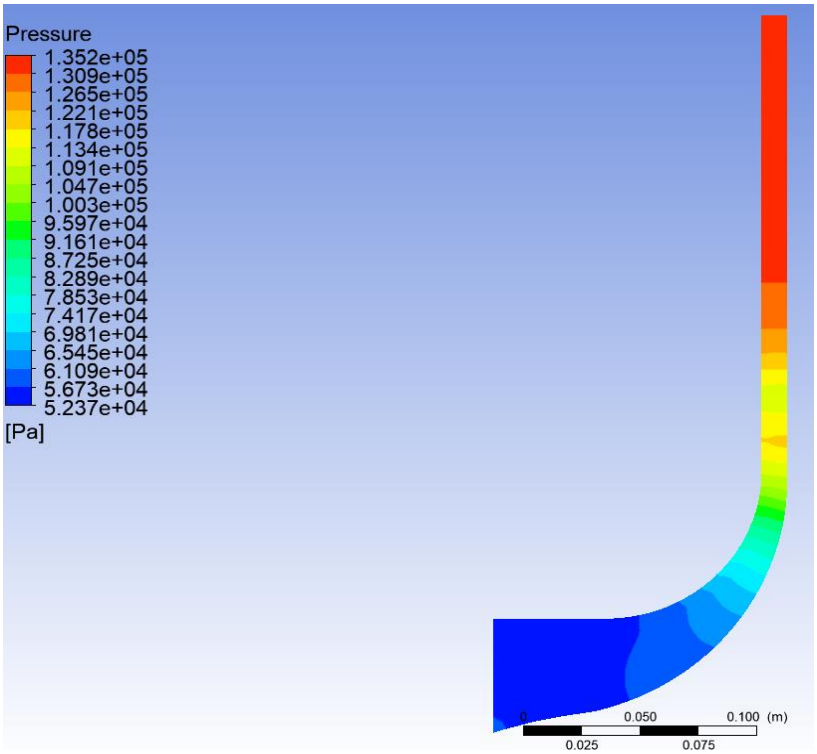

Figure 4. 4: Static Pressure

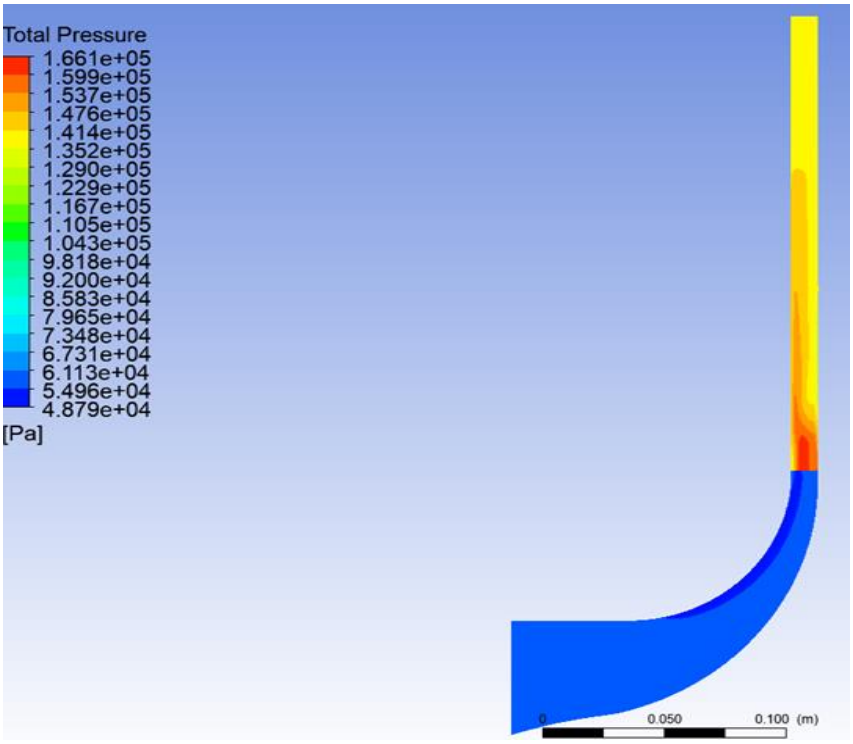

Figure 4. 5: Total pressure

Static Pressure Distribution

The pressure distribution ranges from 52,370 Pa to 135,200 Pa, the highest pressure is at the outlet of the diffuser, indicating the conversion of dynamic pressure into static pressure.

A significant pressure gradient is visible at the diffuser inlet, due to the presence of a shock wave. This shock wave results in a sudden increase in static pressure

the lowest pressure is near the impeller's eye, where the fluid enters.

Total Pressure Distribution

The pressure distribution ranges from 48,790 Pa to 166,100 Pa, the highest total pressure is again at the outlet, where the flow velocity is the highest, consistent with Bernoulli's principle.

The presence of a shock wave at the diffuser inlet is evident by the abrupt change in total pressure, causing a localized region of high pressure.

the lowest total pressure is also at the eye of the impeller, indicating energy conversion and losses.

The impeller adds energy to the fluid, increasing both static and total pressures, the shock wave at the diffuser inlet causes a sudden rise in static pressure, resulting in localized high-pressure regions. This is a critical area where shock-induced energy dissipation occurs, the diffuser converts the remaining kinetic energy into static pressure, resulting in a rise in static pressure towards the outlet.

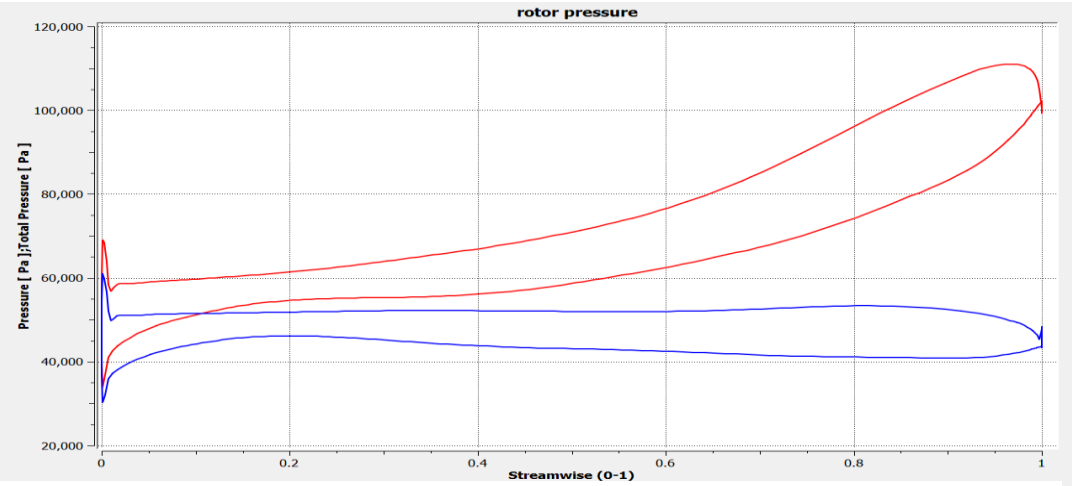

Figure 4. 6: This chart shows us variation of Total and static pressure in impeller and diffuser: Static Pressure chart (red) – Total pressure chart(blue)

Static and total temperature:

This figures shows us variation of Total and static Temperature of the impeller and diffuser for meridional plane.

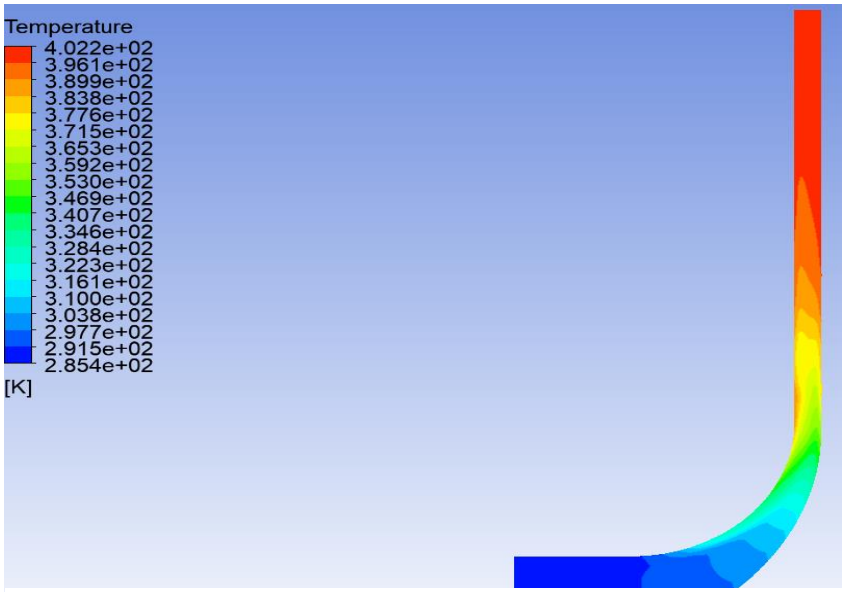

Figure 4. 7: Static Temperature

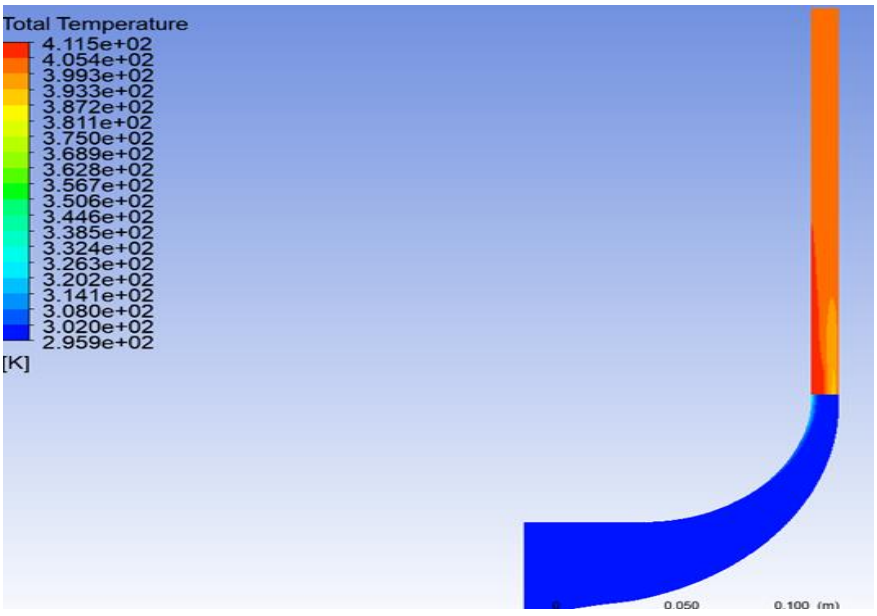

Figure 4. 8: Total Temperature

Static Temperature Distribution

The temperature distribution ranges from 285.4 K to 402.2 K. The highest temperatures (red color) are at the diffuser outlet, indicating significant temperature rise as the fluid exits the diffuser, Lower temperatures (blue and green colors) are observed near the impeller and the entrance of the diffuser, where the fluid enters and energy is added by the impeller.

The presence of a shock wave at the diffuser inlet, as seen in the pressure distribution, can also affect the temperature distribution, leading to localized regions of increased temperature.

Total Temperature Distribution

The temperature distribution ranges from 295.9 K to 411.5 K. The highest total temperatures are at the outlet of the diffuser, consistent with the energy added to the fluid by the impeller and the subsequent conversion in the diffuser, the lowest total temperatures are near the impeller's eye, indicating the initial state of the fluid before energy addition.

The presence of a shock wave at the diffuser inlet is indicated by a sudden rise in total temperature, reflecting the conversion of kinetic energy into thermal energy.

So: The impeller adds energy to the fluid, increasing both static and total temperatures. The shock wave at the diffuser inlet causes a sudden temperature rise, indicating a localized area of high thermal energy due to the conversion of kinetic energy from the shock, the diffuser further converts kinetic energy into thermal energy, increasing static temperature towards the outlet.

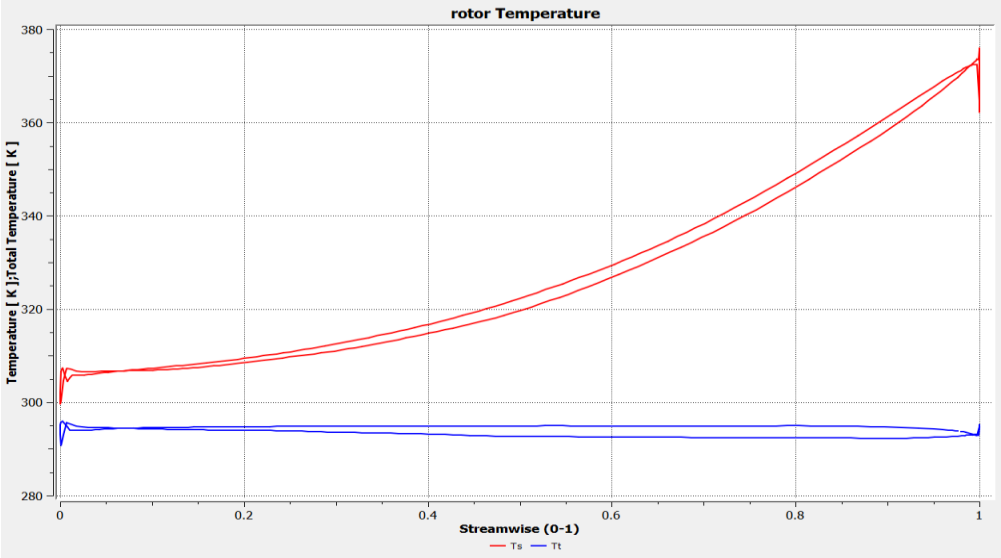

Figure 4. 9: This chart shows us the variation of Total and static Temperature in the impeller and diffuser: Static Temperature chart (red) – Total Temperature chart(blue)

Mach number:

This figure shows us the variation of Mach number in the impeller and diffuser for the meridional plane.

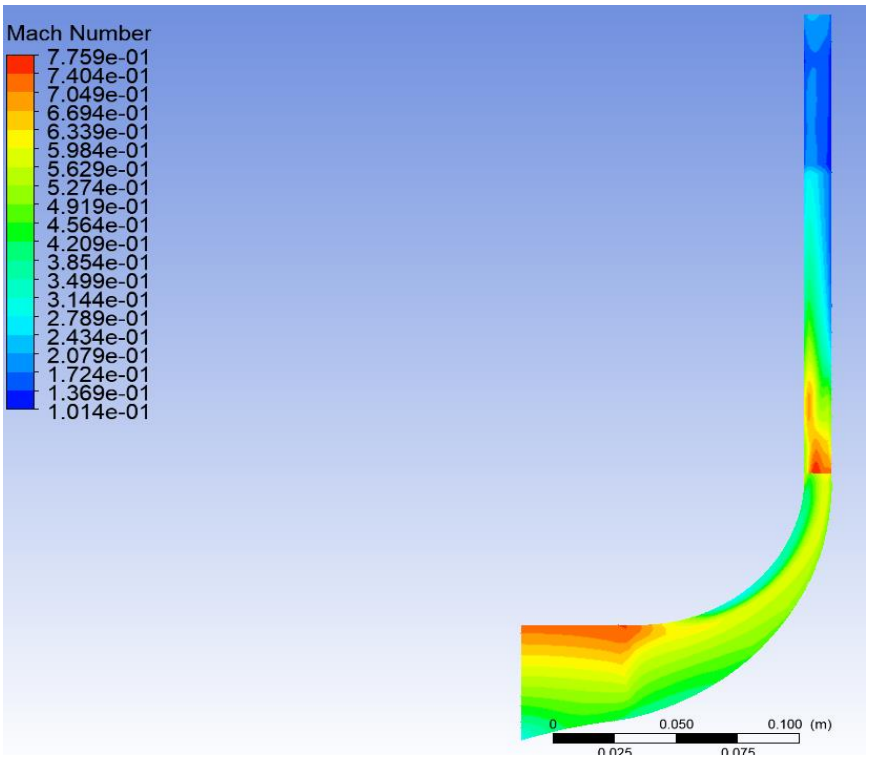

Figure 4. 10: Mach number

Mach Number Distribution

The Mach number ranges from 0.101 to 0.776. The highest Mach numbers (red color) are observed at the diffuser inlet, indicating high-velocity regions where the fluid flow speed approaches the speed of sound, which is consistent with the presence of a shock wave, Lower Mach numbers (blue and green colors) are observed near the impeller, where the fluid is initially entering and gaining energy from the impeller blades.

As the fluid moves through the diffuser, the Mach number decreases significantly, indicating a reduction in flow velocity as the kinetic energy is converted into pressure energy.

Static entropy:

This figure shows us variation of static entropy of the impeller and diffuser for meridional plane.

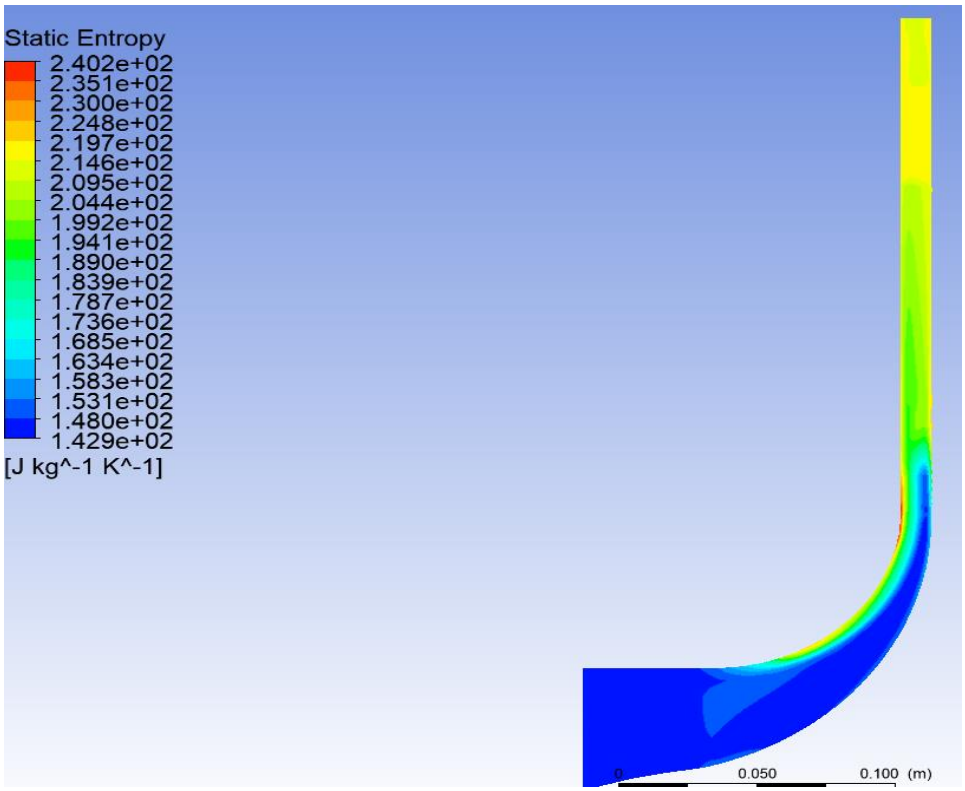

Figure 4. 11: Entropy

The highest entropy values are observed near the trailing edge of the impeller and within the diffuser, especially at the curved sections. Low entropy near the impeller, increasing to high entropy in the diffuser.

High entropy variation suggests significant energy losses and reduced efficiency. Shock waves and flow separation contribute to entropy increase and performance degradation.

4.3.3. Orthogonal Plane:

Static and total pressure:

These figures show us the variation of Total and static pressure of the impeller and diffuser for the orthogonal plane.

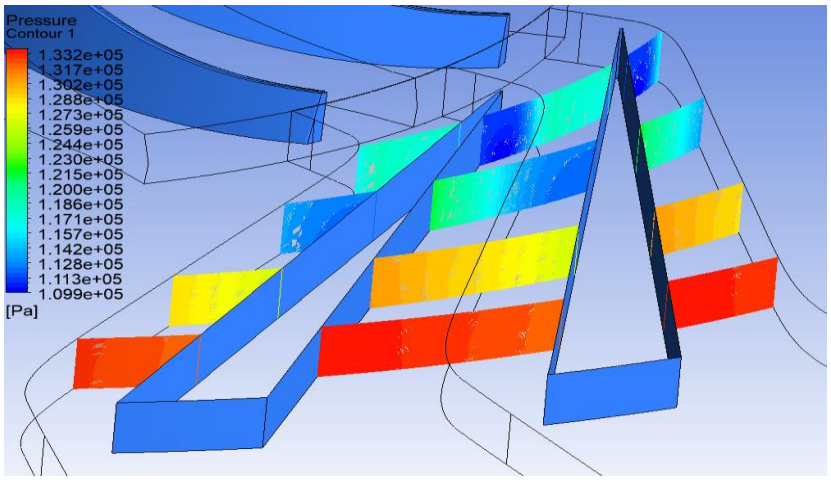

Figure 4. 12: Static Pressure

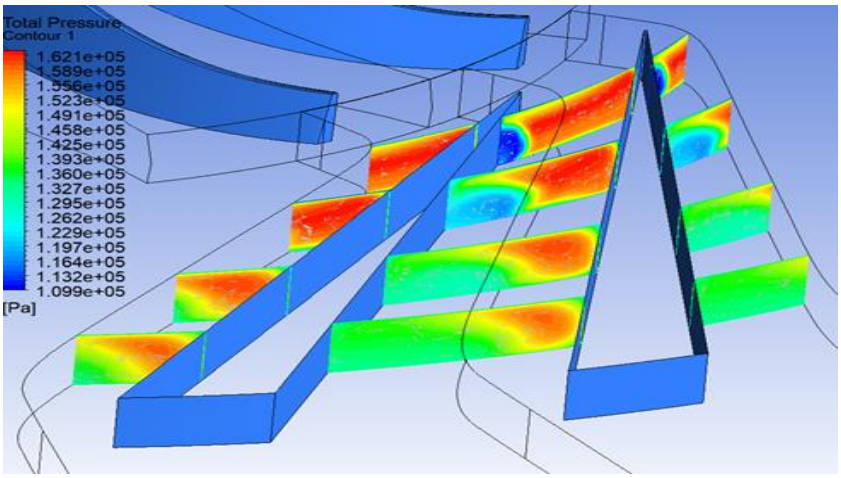

Figure 4. 13: Total pressure

Static Pressure Distribution:

The first image depicts the static pressure distribution.

There is a clear gradient from high pressure (red zones) to low pressure (blue zones) as the flow moves through the impeller towards the diffuser.

Notable high-pressure areas are observed at the leading edges of the diffuser blades, indicating the regions where the fluid decelerates and pressure increases.

Total Pressure Distribution:

The second image shows the total pressure distribution.

The presence of high total pressure regions (red) at the leading edges and within the diffuser suggests areas of high kinetic energy, likely due to the conversion of dynamic pressure.

Lower total pressure areas (green and blue zones) towards the trailing edges of the diffuser blades indicate energy losses possibly due to flow separation or viscous effects.

The shock wave at the diffuser inlet is evident in both figures, particularly highlighted by the abrupt changes in pressure.

In the static pressure distribution, the shock wave manifests as a sharp transition zone, likely causing a sudden increase in static pressure.

In the total pressure distribution, the shock wave's effect is seen as localized regions of high pressure upstream of the diffuser blades, followed by rapid pressure drops.

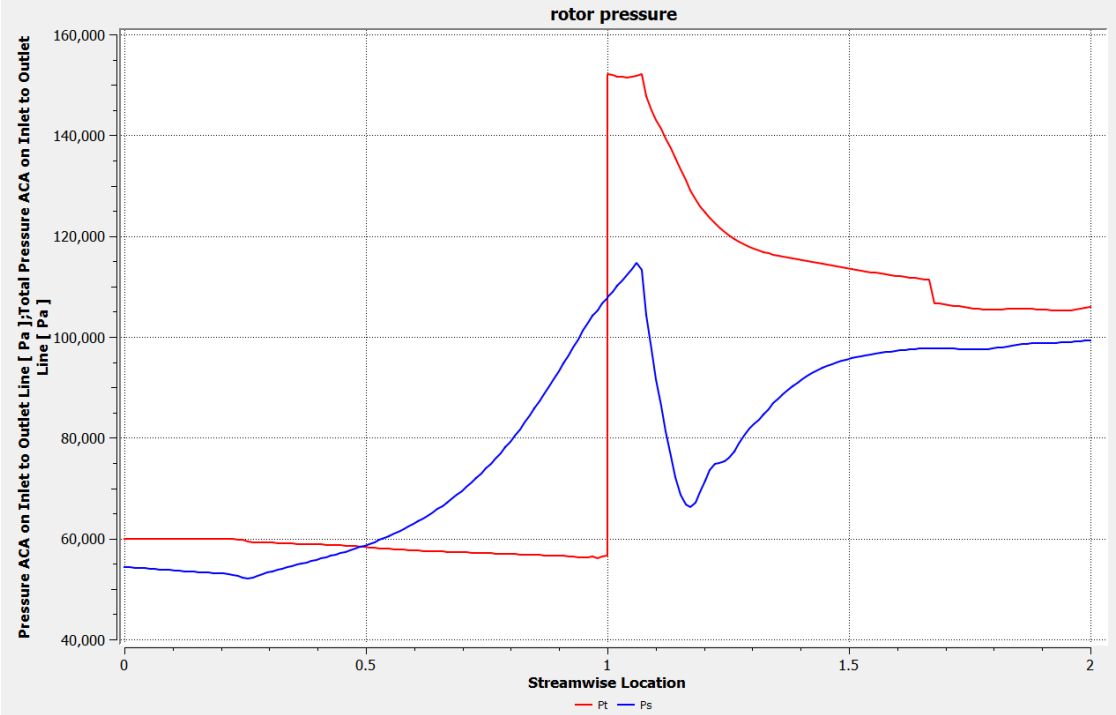

Figure 4. 14: This chart shows us the variation of Total and static pressure in the impeller and diffuser: Static Pressure chart (blue)– Total pressure chart(red)

Static and total temperature:

This figure show us the variation of the Total and static temperature of the impeller and diffuser for the orthogonal plane.

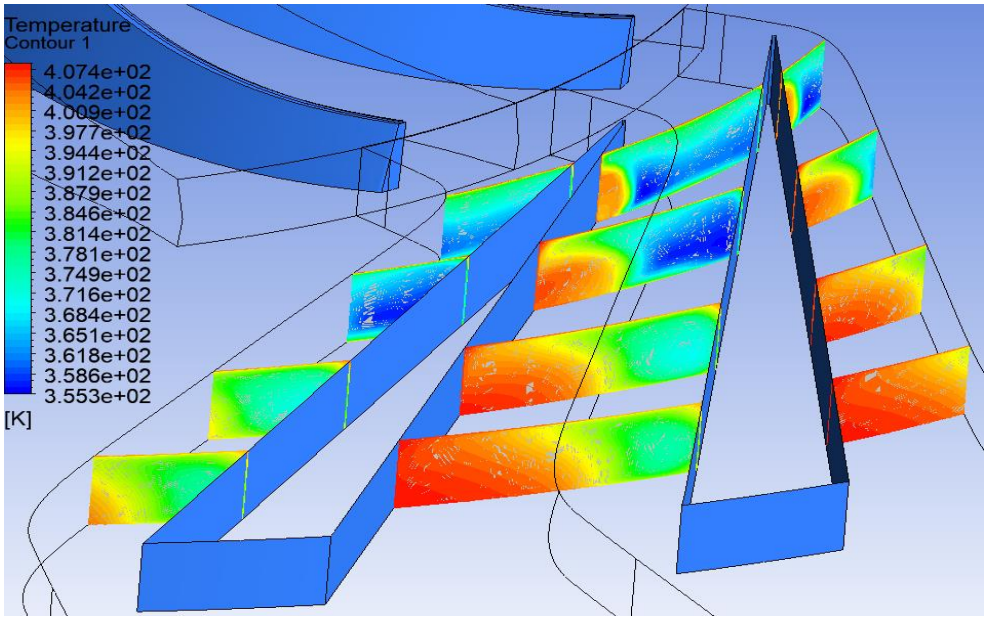

Figure 4. 15: Static Temperature

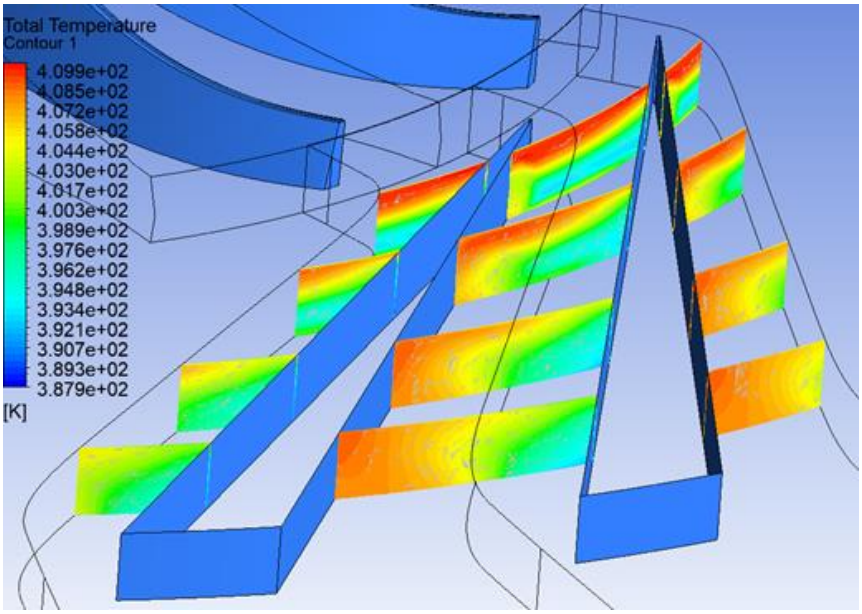

Figure 4. 16: Total Temperature

Total Temperature Distribution:

The total temperature values range from approximately 387.9 K to 409.2 K. Higher temperatures are observed near the impeller's exit and the inlet of the diffuser, suggesting significant energy transfer and compression effects.

Static Temperature Distribution:

The static temperature values range from about 355.3 K to 407.4 K. The static temperature is lower than the total temperature, which indicates the presence of dynamic effects and contributions of fluid velocity to the total energy.

A shock wave is present at the inlet of the diffuser. It causes an abrupt change in temperature gradients and sudden temperature increases.

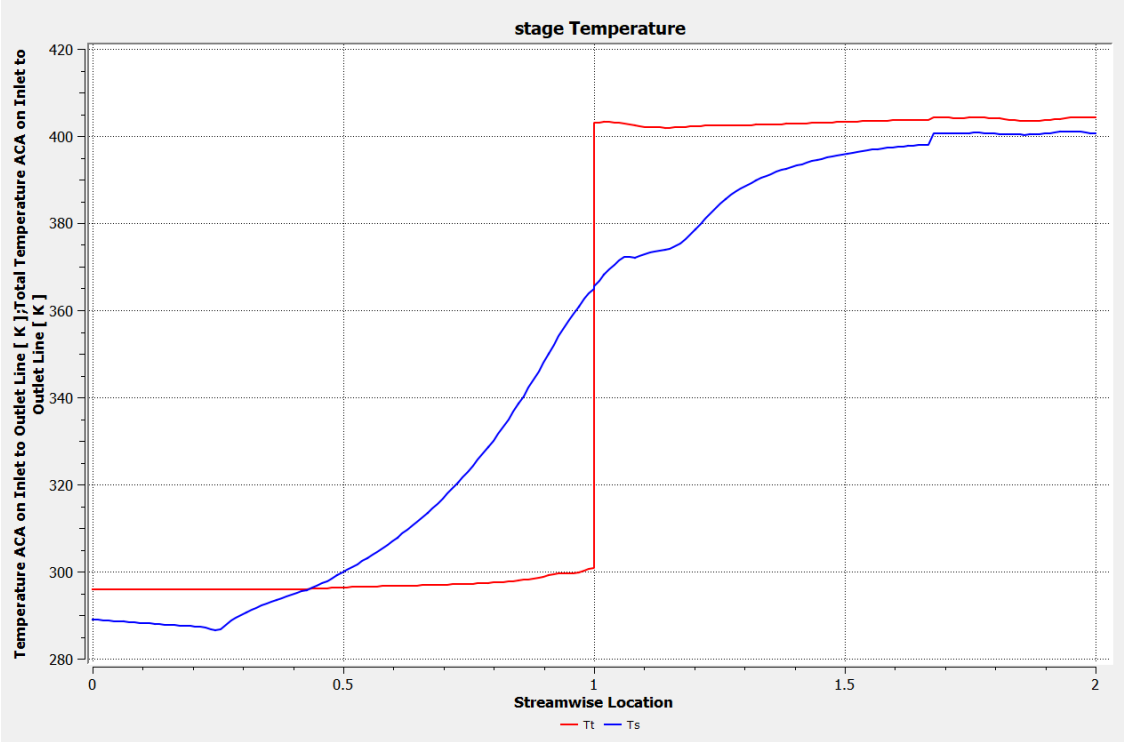

Figure 4. 17: This chart shows us variation of Total and static Temperature in impeller and diffuser: Static Temperature chart (blue) – Total Temperature chart (red)

Mach number:

This figure shows us variation of Mach number in the impeller and diffuser for orthogonal plane.

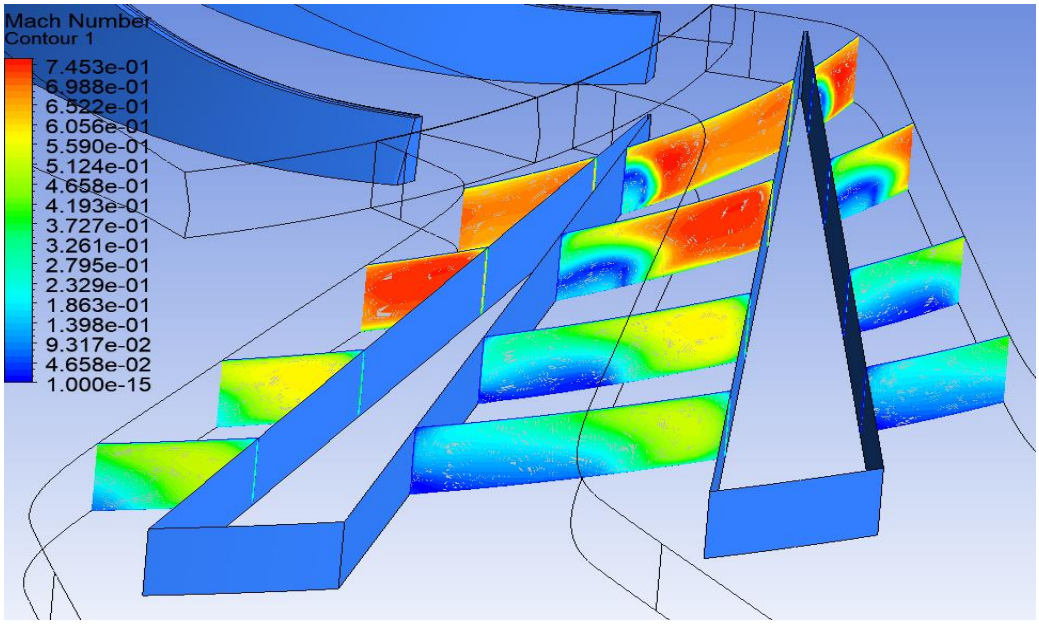

Figure 4. 18: Mach number

The Mach number values range from approximately 0 (blue) to 0.7435 (red). Higher Mach numbers are observed near the exit of the impeller and the inlet of the diffuser, indicating regions of higher flow velocity.

The presence of the shock wave at the inlet of the diffuser, is evidenced by the abrupt changes in Mach number. This indicates a rapid deceleration and compression of the flow, characteristic of shock waves in compressible flows.

Static entropy:

This figure shows us the variation of static entropy of the impeller and diffuser for the orthogonal plane.

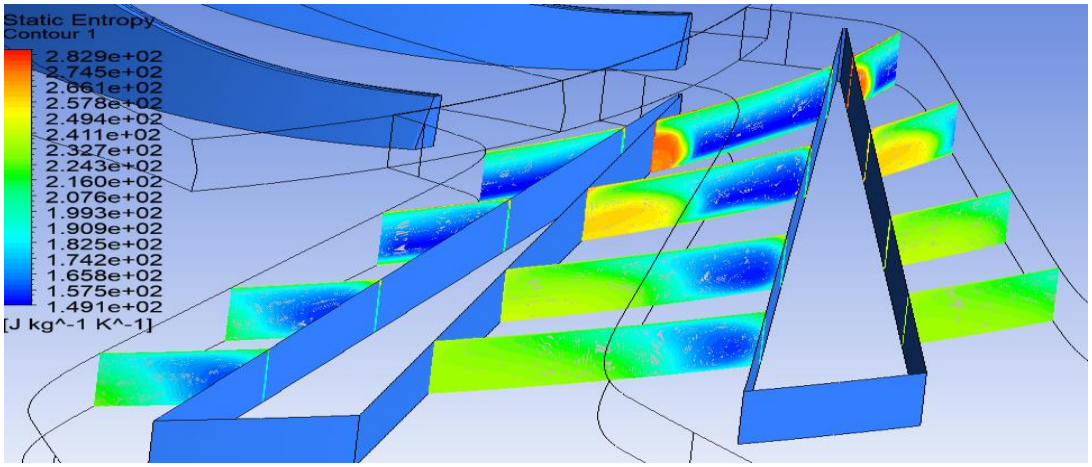

Figure 4. 19: Entropy

Entropy ranges from 149 to 282 J/kg·K. Higher entropy regions are near the leading and trailing edges of the blades, indicating significant energy dissipation.

High entropy areas indicate energy losses and inefficiencies. Due to the presence of shock waves and turbulent regions.

4.3.4. Blade-to-Blade Plane:

Static and total pressure:

This figure shows us the variation of Total and static pressure of the impeller and diffuser for the blade-to-blade plane.

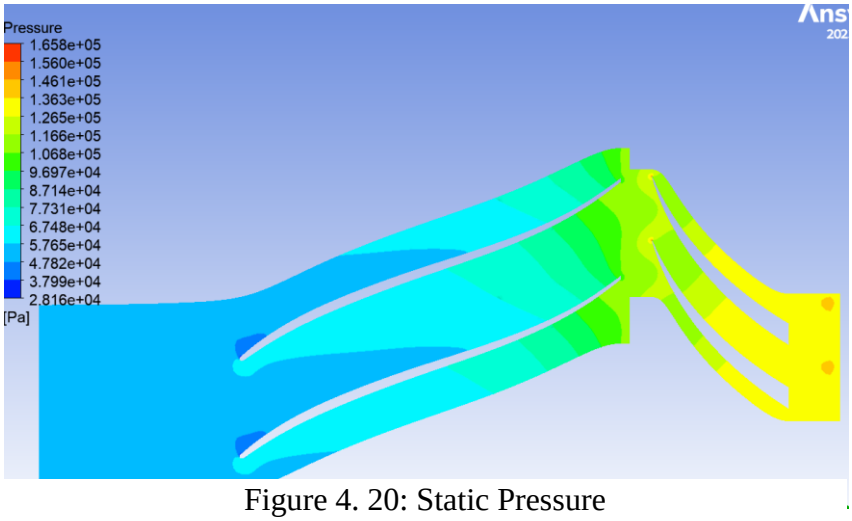

Figure 4. 20: Static Pressure

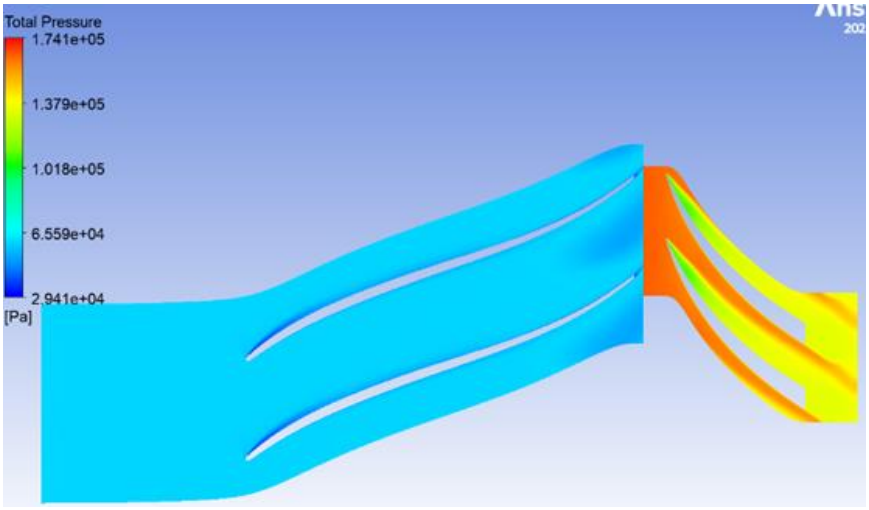

Figure 4. 21: Total pressure

Static Pressure Distribution

The static pressure is highest at the inlet of the impeller, As the flow moves through the impeller blades, the static pressure decreases.

At the diffuser inlet, there's a noticeable drop in static pressure, which indicates the presence of a shock wave.

Total Pressure Distribution

The total pressure also shows a high value at the impeller inlet, it gradually decreases as the flow passes through the impeller.

There is a significant drop in total pressure at the diffuser inlet, due to shock wave as observed in the static pressure distribution.

Static and total temperature:

These figures show us variations of the Total and static temperature of the impeller and diffuser for the blade-to-blade plane.

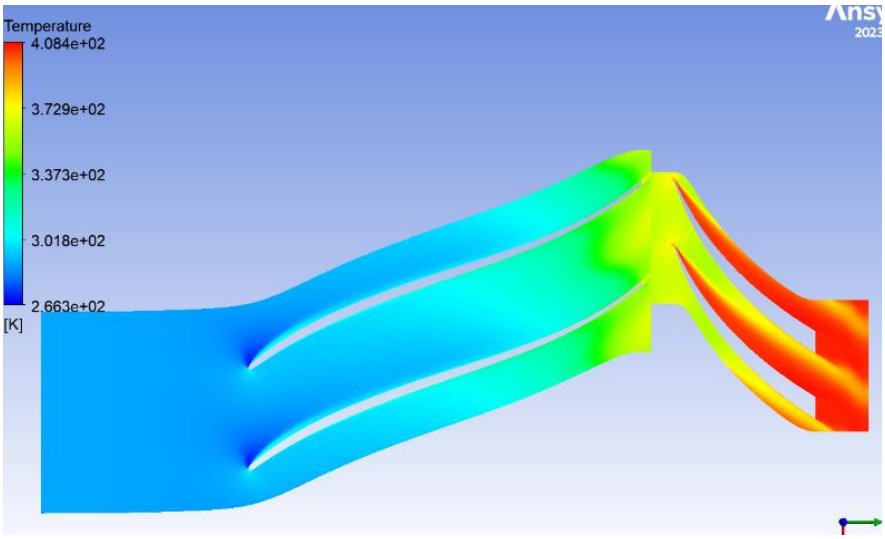

Figure 4. 22: Static Temperature

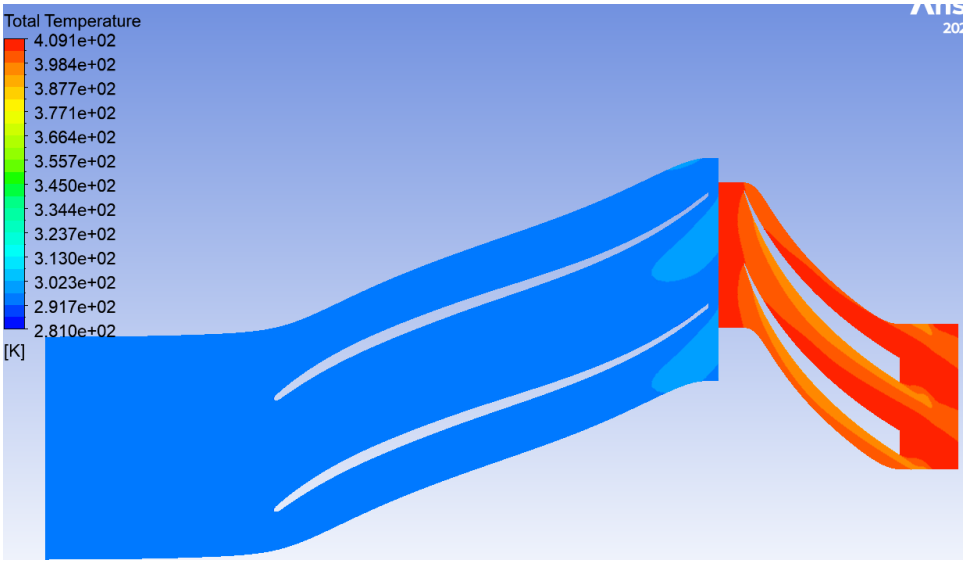

Figure 4. 23: Total Temperature

Notably, a shock wave is visible at the diffuser inlet, indicating a sudden temperature increase typical of high-speed aerodynamic flows. The temperature gradient illustrates the energy transformation from the impeller through the diffuser.

Mach number:

This figure shows us the variation of Mach number in the impeller and diffuser for the blade-to-blade plane.

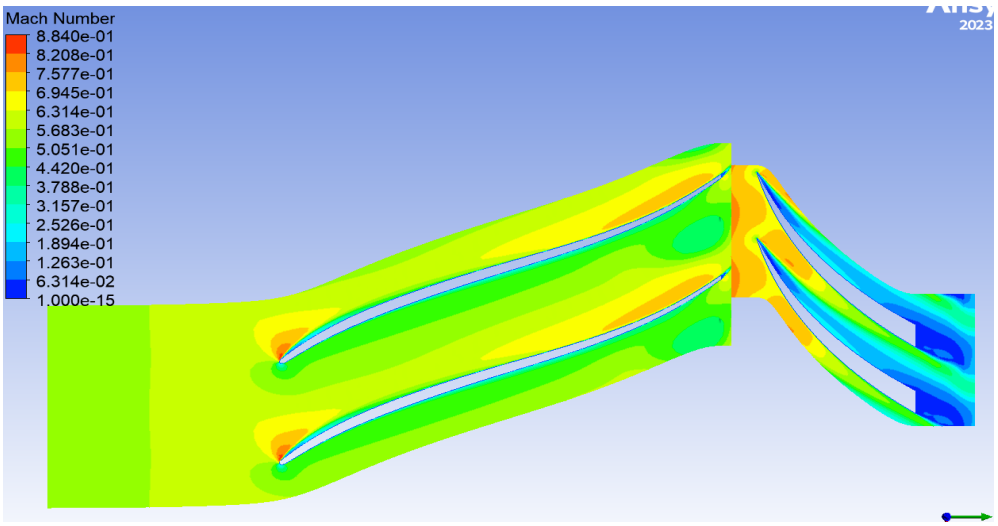

Figure 4. 24: Mach number

The Mach number increases along the impeller, indicating acceleration, and reaches a peak near the diffuser inlet, where a shock wave is likely present.

Static entropy:

This figure shows us the variation of static entropy of the impeller and diffuser for the blade-to-blade plane.

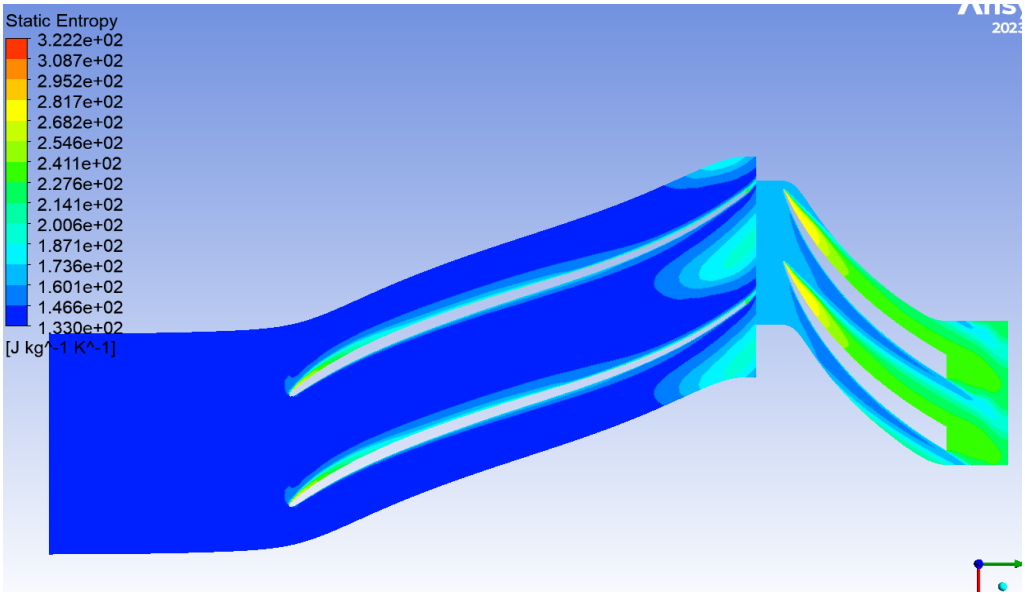

Figure 4. 25: Entropy

there is a shock wave at the diffuser inlet, marked by a sudden increase in entropy. This indicates abrupt changes in pressure and temperature as the flow decelerates from supersonic to subsonic speeds.

4.4. The flow influence:

To study the flow influence we chose 3 points with different values of flow

- The main point **M=2.016[kg/s]**, it is a middle point
- The point next to surge **S=2.16[kg/s].**
- The point next to sonic blockage **P=1.89 [kg/s]**.

To compare the three points, we present the static entropy in the figure below.

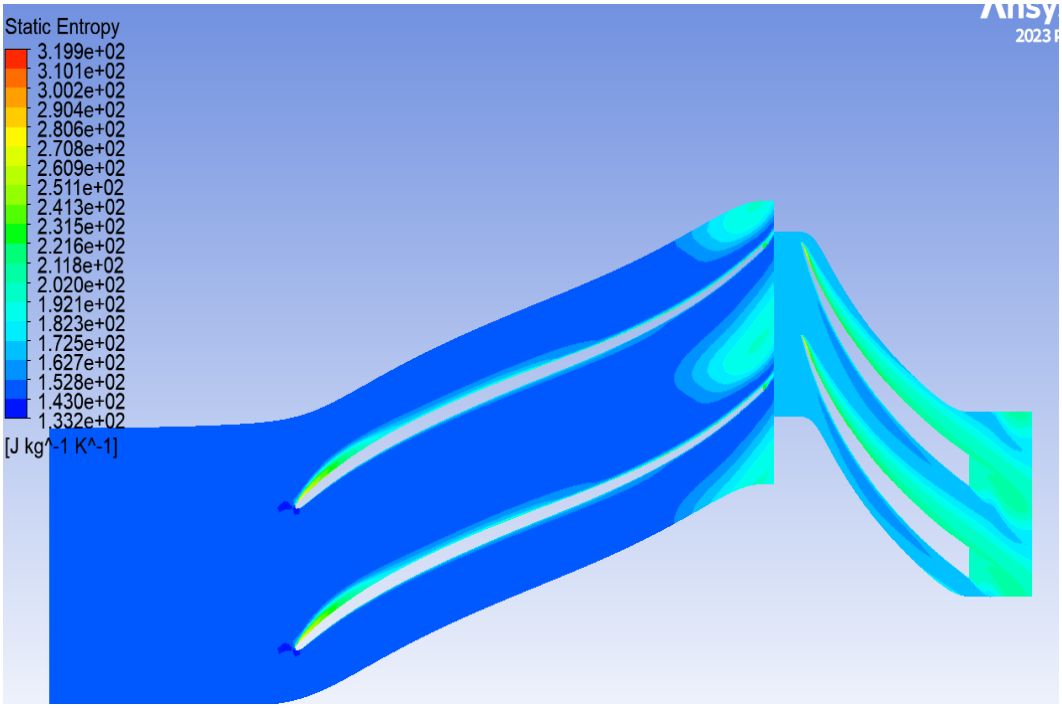

Figure 4. 26: Entropy distribution in P

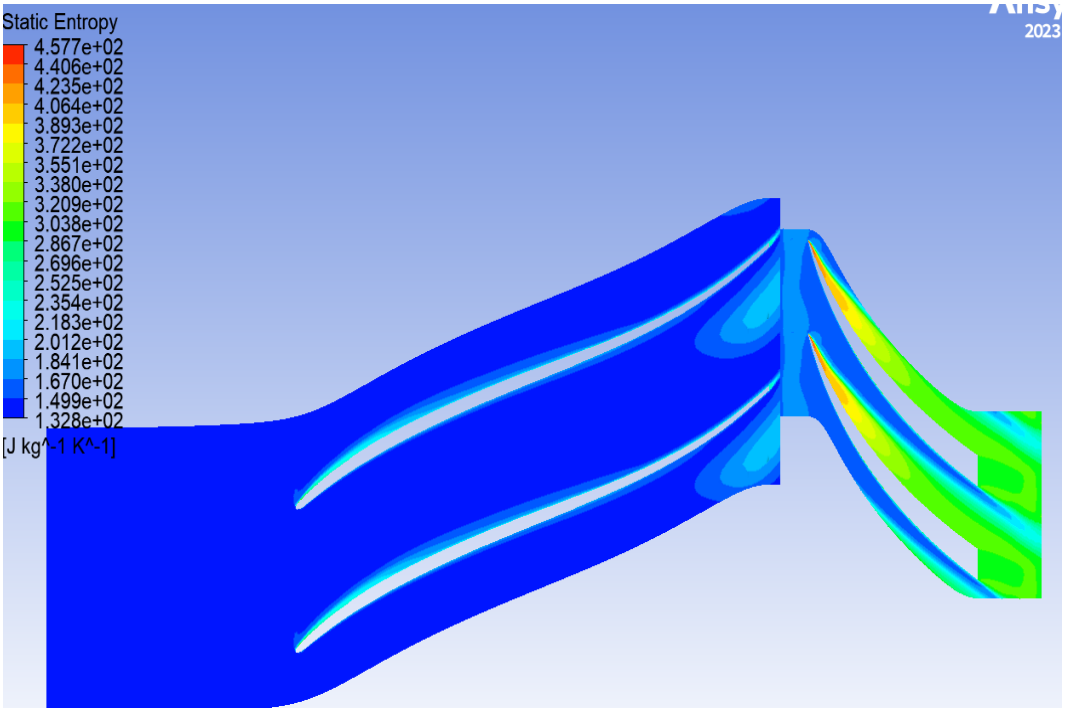

Figure 4. 27: Entropy distribution in S

We see that energy loss is greater in the high flow value, it decreases as we decrease the flow

Table 4. 2: This table shows the flow influence

Corrective flow	efficiency	Pressure ratio	Temperature ratio
M=2.016	0.778384	2.37073	1.35932
S= 2.1623	0.598193	1.92824	1.34494
P= 1.8985	0.853119	2.57702	1.36403

In this table, we resume the results of the three flow points.

we took three points, S next to the surge, P near the blockage, and the main point M

We see that the lowest value has the best performance then it decreases with rising the flow value.

We can say that the shock wave decreases the performance.

we saw that the best result corresponded to P with the highest efficiency, Pressure, and temperature ratio value. Then M point and S point with the lowest value

This simulation highlights the impact of the shock wave on the performance and efficiency of the impeller and diffuser system, indicating potential areas for design optimization to mitigate shock effects.

4.5. Part 2: Influence Tip Clearance

In this part we study the influence of Tip on the compressor performance, we choose three Tip values which are: Tip clearance **0 %,** 3 **%**, and 6 **%.**

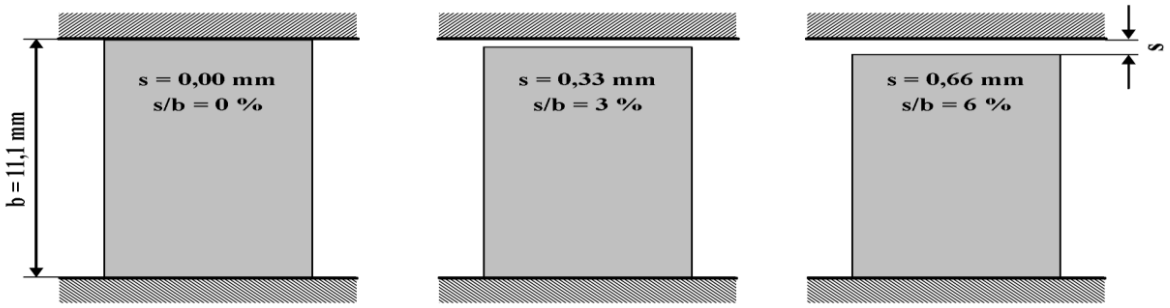

Figure 4. 28: Tip clearance in diffusor

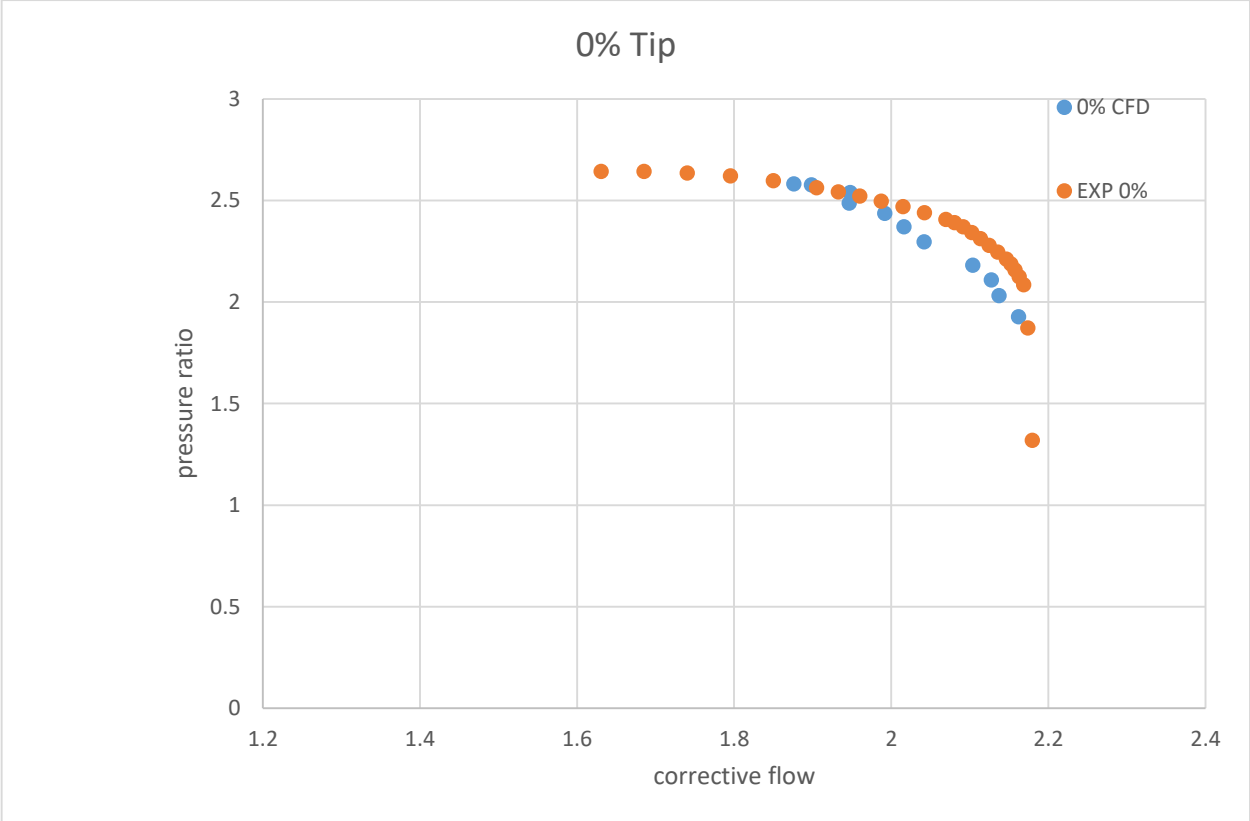

Figure 4. 29: comparison between experimental and CFDs result with 0% Tip

As we mentioned in the previous part we work with the second mesh due to its compatibility

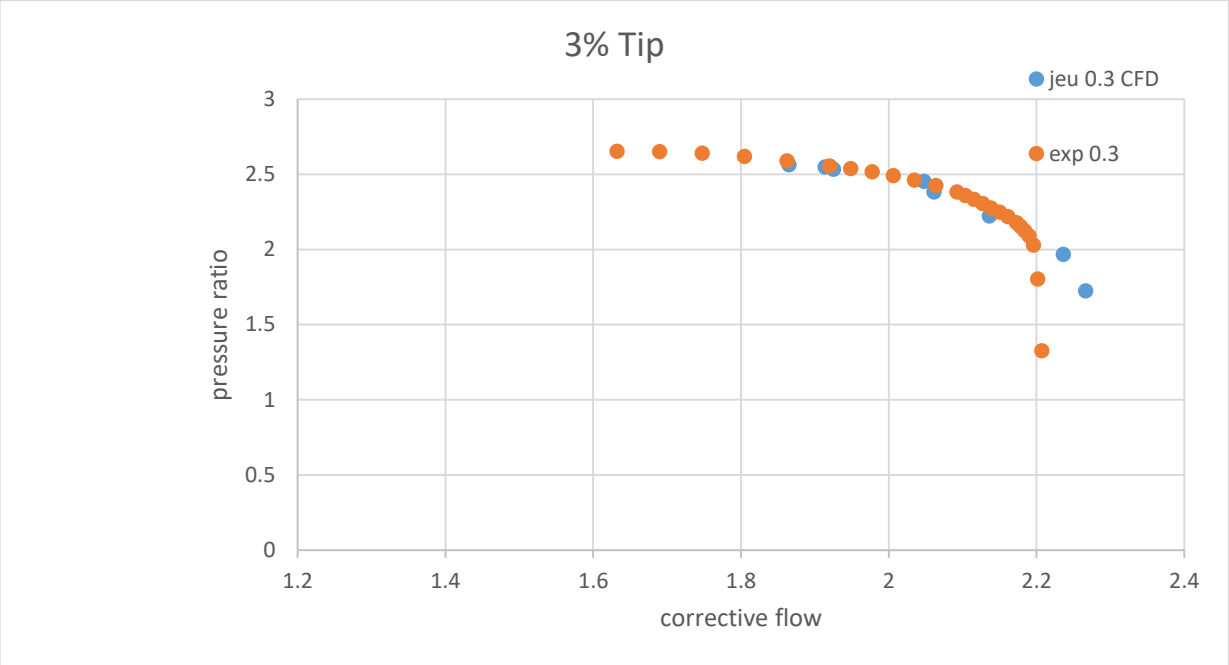

Figure 4. 30: comparison between experimental and CFDs results with 3% Tip

We have certain CFD points are conform with the experimental result, which means a good precision.

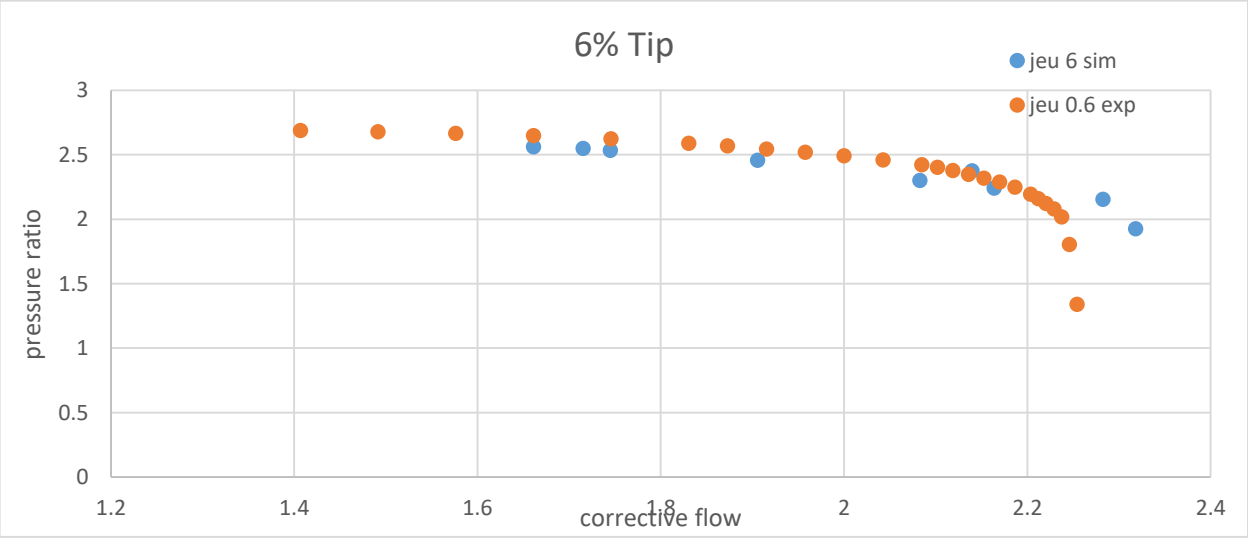

Figure 4. 31: comparison between experimental and CFDs results with 6% Tip

Here we also have a good indication, as the result of our simulation.

4.5.1. Aerothermodynamic parameter

The figures below show the variation of different aerothermodynamic parameters for the blade-to-blade plane to S point corrective flow value and Tip value equal to 0%.

Mach number:

This figure shows us the variation of the Mach number of the impeller and diffuser for the blade-to-blade plane.

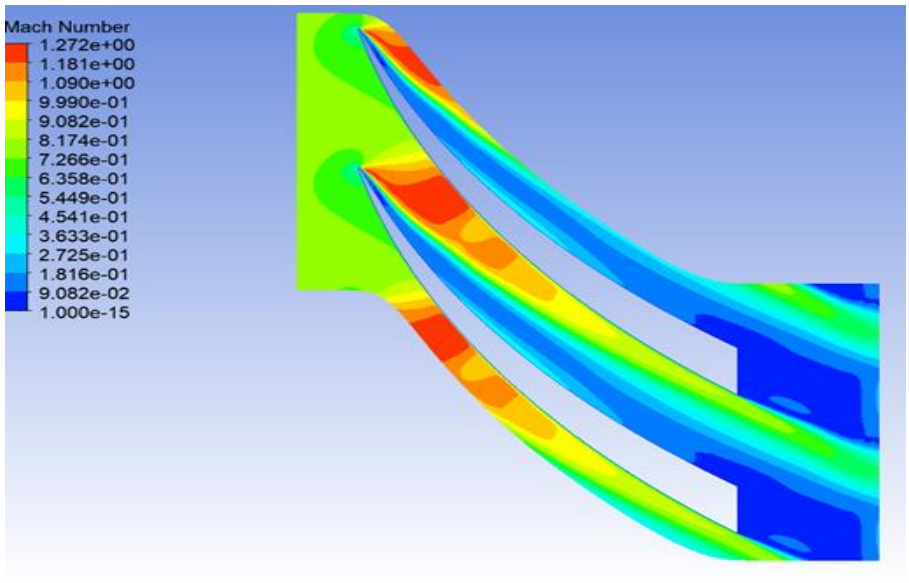

Figure 4. 32: Mach number

Static entropy:

This figure shows us the variation of static entropy of the impeller and diffuser for the blade-to-blade plane.

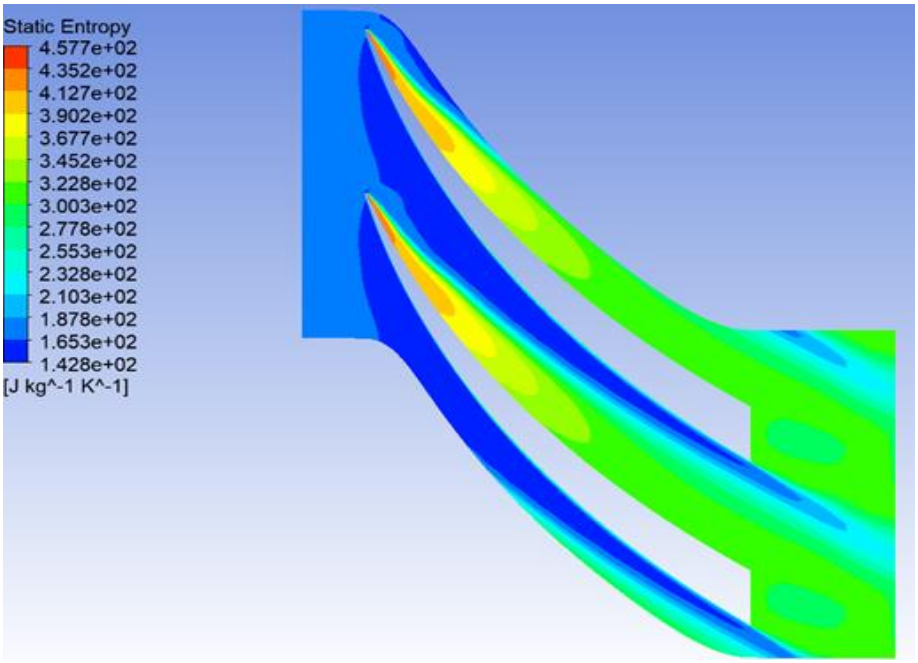

Figure 4. 33: Static entropy

static pressure:

This figure shows us the variation of the static pressure of the impeller and diffuser for the blade-to-blade plane.

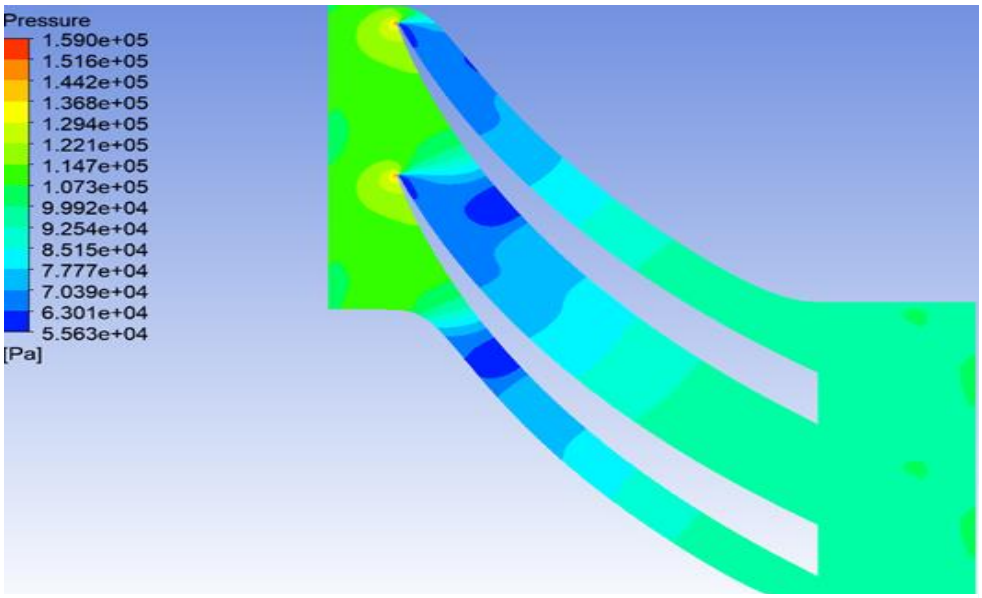

Figure 4. 34: static pressure

4.5.1. orthogonal plane

4.5.1.1. Tip clearance 0%:

The images below show the variation of different aerothermodynamic parameters for orthogonal planes in different corrective flow values and Tip values equal to 0%.

static pressure:

This figure shows us the variation of the static pressure of the impeller and diffuser for the orthogonal plane.

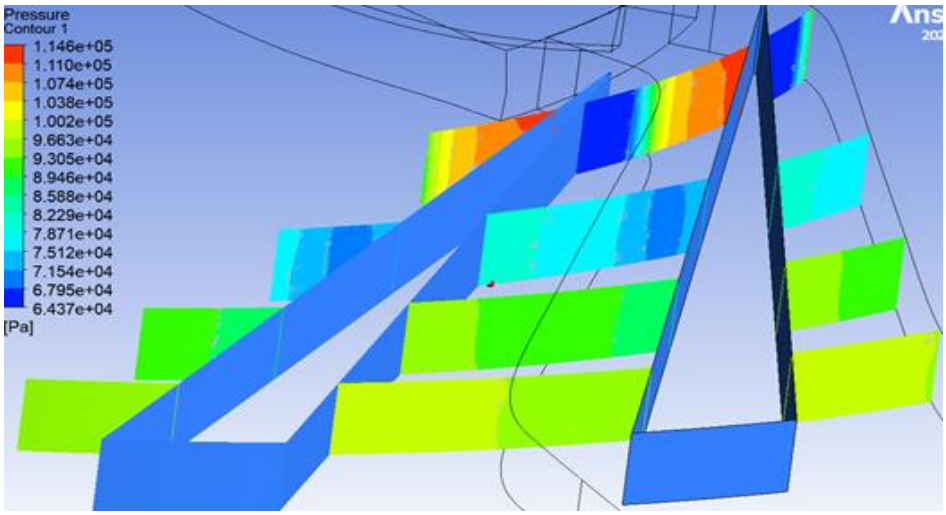

Figure 4. 35: static pressure

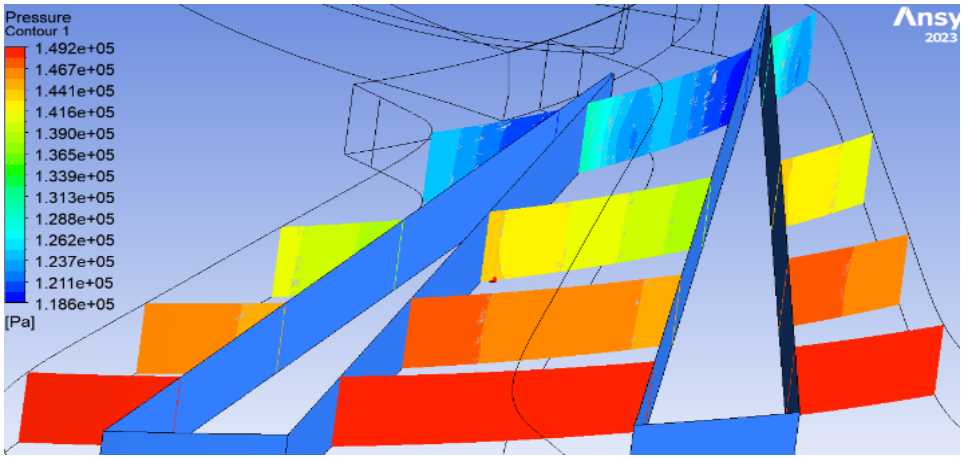

Figure 4. 36: Tip clearance 0% P

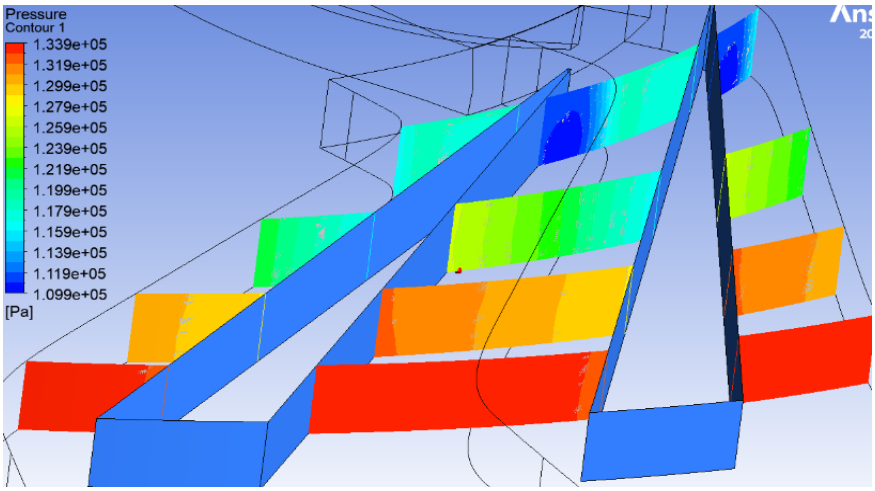

Figure 4. 37: *Tip clearance 0% M*

The first image has the lowest overall pressure range (0.64 bar to 1.14 bar). It shows the least pronounced shock waves with a more gradual pressure change.

The second image has the highest overall pressure range (1.18 bar to 1.49 bar). It shows the most pronounced shock waves with a steep and abrupt pressure change.

The third image falls between the first and second in terms of pressure range (1.11 bar to 1.34 bar). It also shows pronounced shock waves, similar to the second image, with significant and abrupt pressure changes.

Overall, the second and third images indicate stronger shock waves compared to the first image, with the second image showing the highest pressure range and the most distinct transitions between pressure regions.

Mach number:

This figure shows us the variation of the Mach number of the impeller and diffuser for the orthogonal plane.

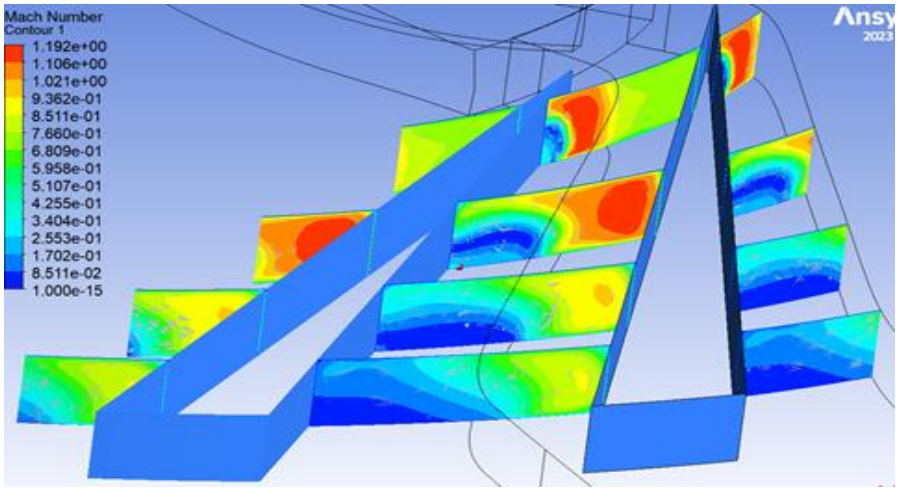

Figure 4. 38: Tip clearance 0% S

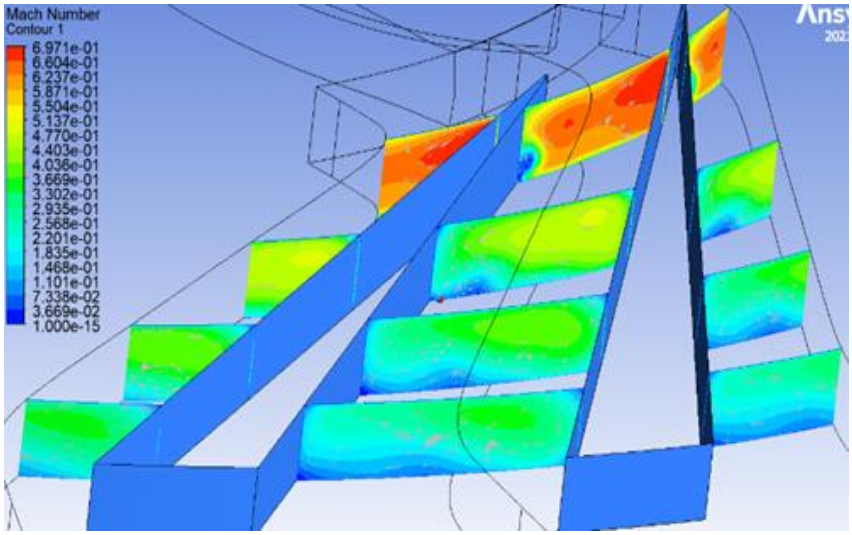

Figure 4. 39: Tip clearance 0% P

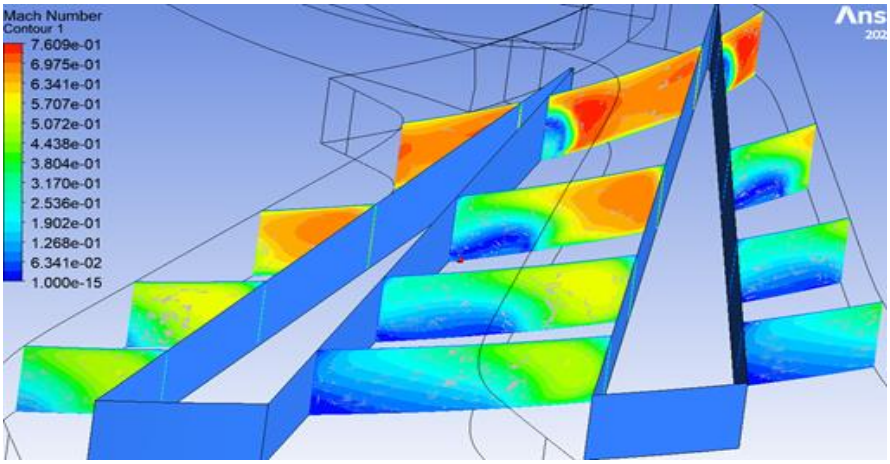

Figure 4. 40: Tip clearance 0% M

Image 1 and Image 2 have more intense shock waves than Image 3.

Static entropy:

This figure shows us the variation of static entropy of the impeller and diffuser for the orthogonal plane.

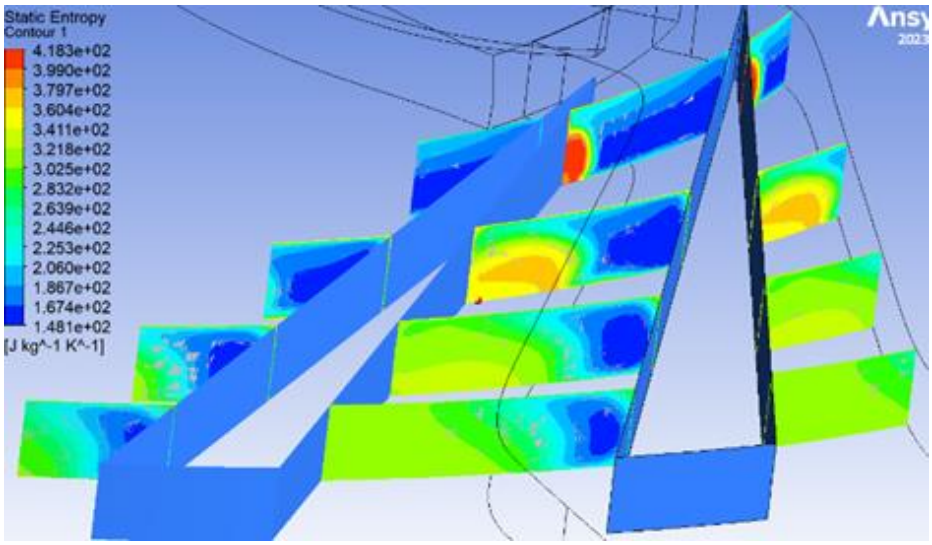

Figure 4. 41: Tip clearance 0% S

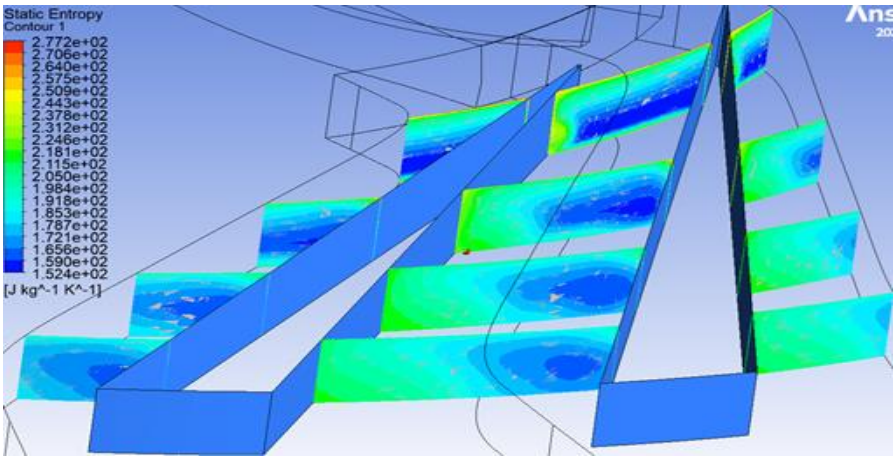

Figure 4. 42: Tip clearance 0% P

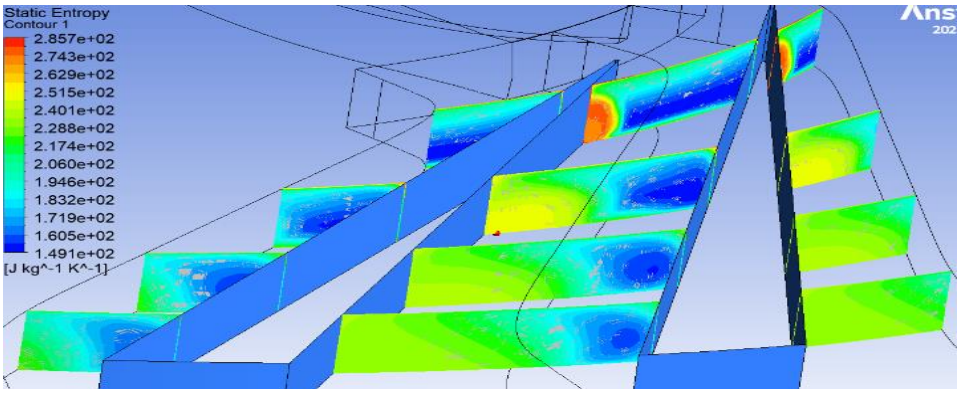

Figure 4. 43: Tip clearance 0% M

The first image shows the most significant variation in entropy, with clear high-entropy regions indicating strong shock waves.

The second and third images display lower entropy levels and less pronounced high-entropy regions, indicating weaker shocks or more efficient shock mitigation.

The difference in entropy distribution among the three images suggests variations in flow conditions, such as different inlet velocities, pressure ratios, or geometric modifications affecting the shock wave strength and location.

The presence of shock waves is most evident in the first image, with high entropy values indicating strong shocks. The second and third images show weaker shock waves, with lower entropy variations. This analysis implies that different flow conditions or design modifications significantly impact shock wave intensity and entropy distribution within the flow field.

4.5.1.2. Tip clearance 3%:

The images below show the variation of different aerothermodynamic parameters for orthogonal planes in different corrective flow values and Tip values equal to 3%.

For this clearance we took:

- The main point **M= 2.05 [kg/s]**, it is a middle point
- The point next to surge **S= 2.16 [kg/s].**
- The point next to sonic blockage **P= 1.87 [kg/s]**.

Static pressure:

This figure shows us the variation of static pressure of the impeller and diffuser for the orthogonal plane with a Tip clearance of 3%.

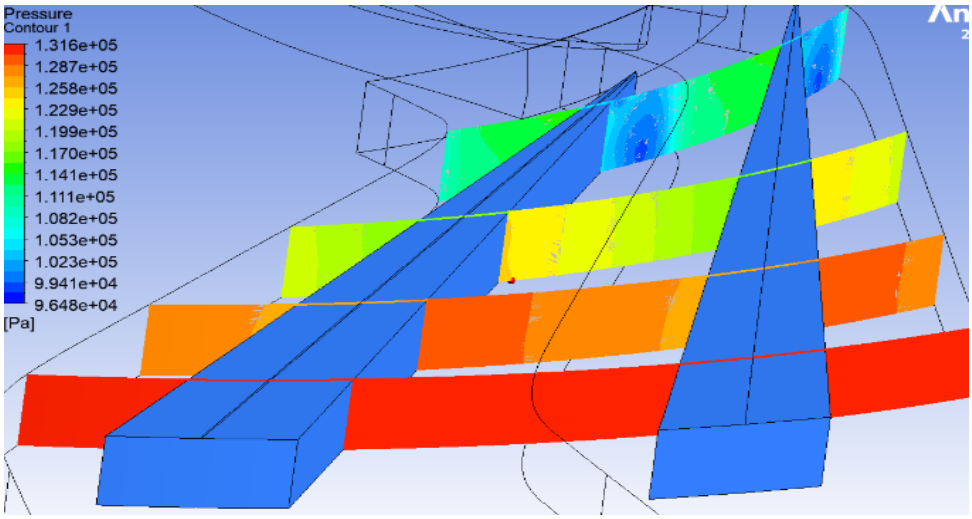

Figure 4. 44: Tip clearance 3% S

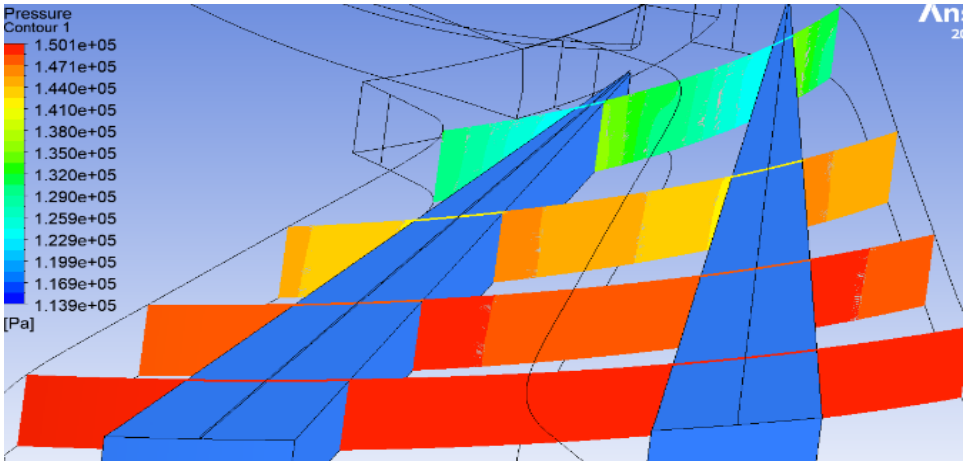

Figure 4. 45: Tip clearance 3% P.

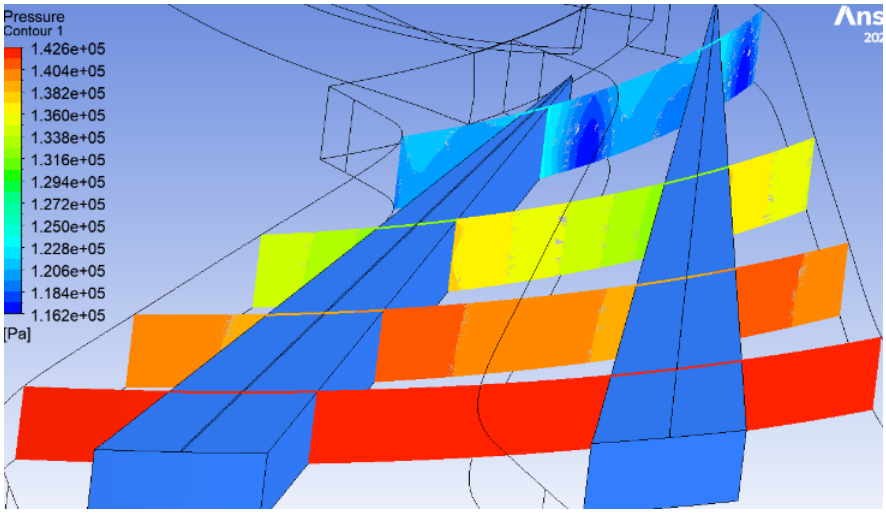

Figure 4. 46: Tip clearance 3% M.

The pressure range is greater than the 0% tip range.

Mach number:

This figure shows us the variation of the Mach number of the impeller and diffuser for the orthogonal plane with a Tip clearance of 3%.

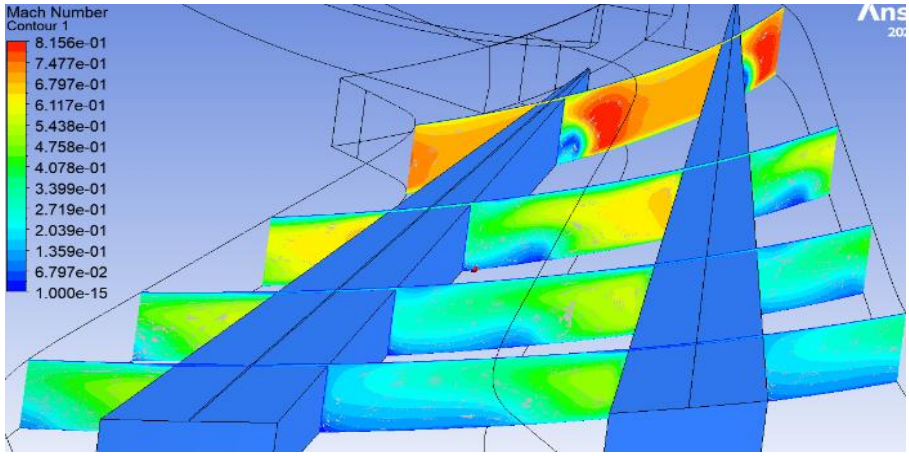

Figure 4. 47: Tip clearance 3% S.

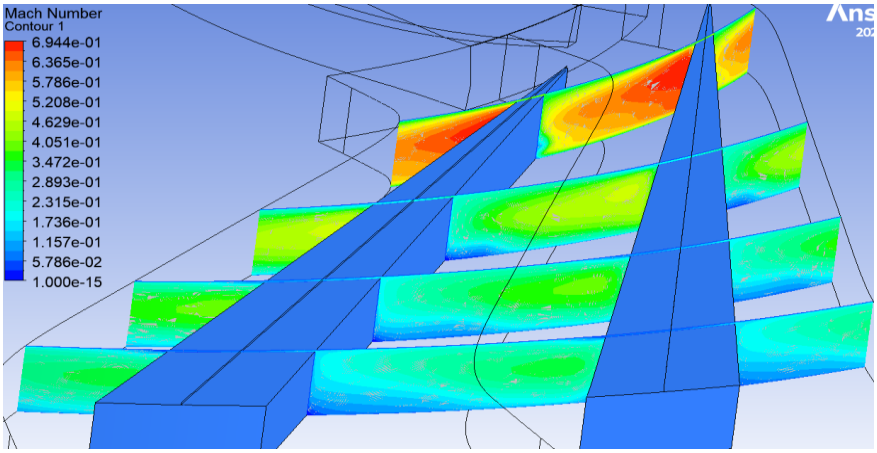

Figure 4. 48: Tip clearance 3%P.

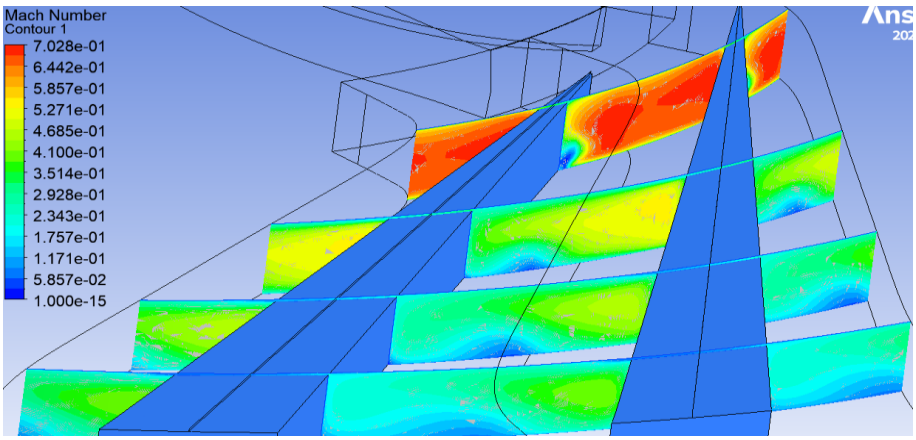

Figure 4. 49: Tip clearance 3% M.

We have less velocity value and more pressure range, which leads us to a quick transfer of velocity to pressure, which results in a higher pressure ratio.

Static entropy:

This figure shows us the variation of static entropy of the impeller and diffuser for the orthogonal plane with a Tip clearance of 3%.

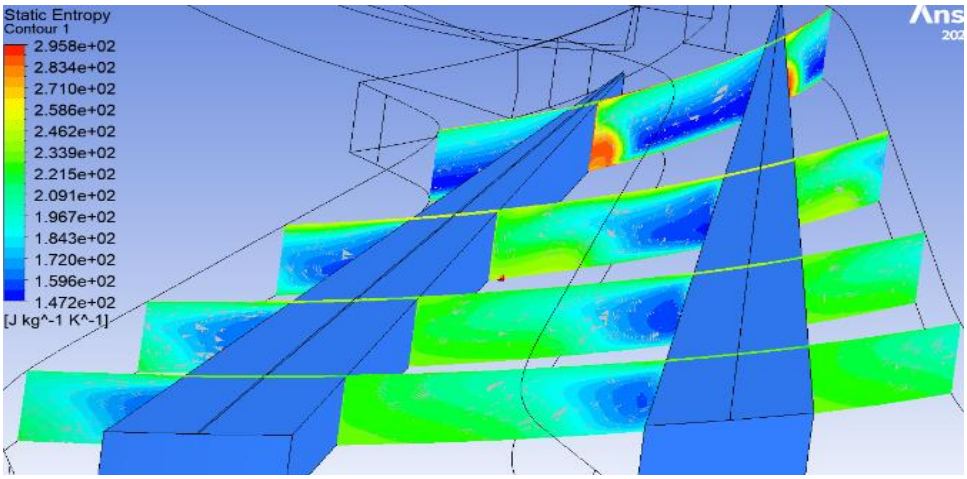

Figure 4. 50: Tip clearance 3% S

.

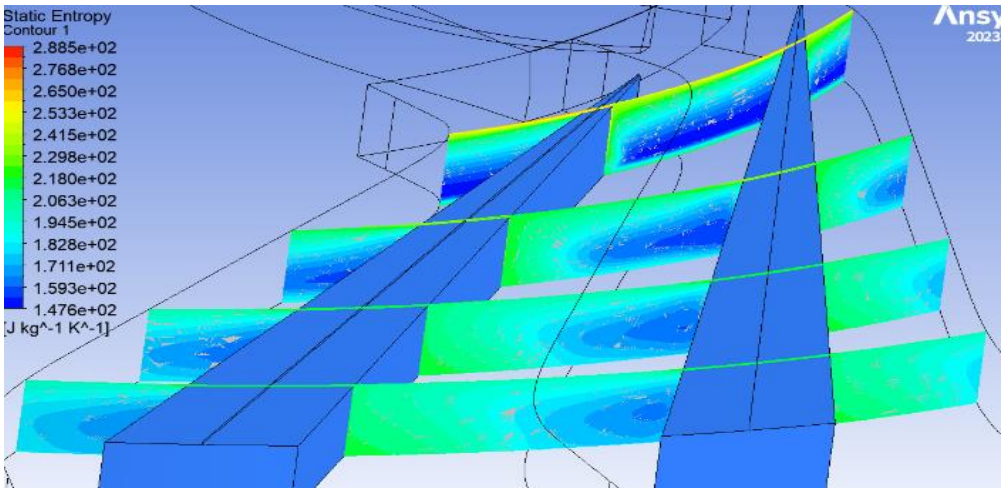

Figure 4. 51: Tip clearance 3% P.

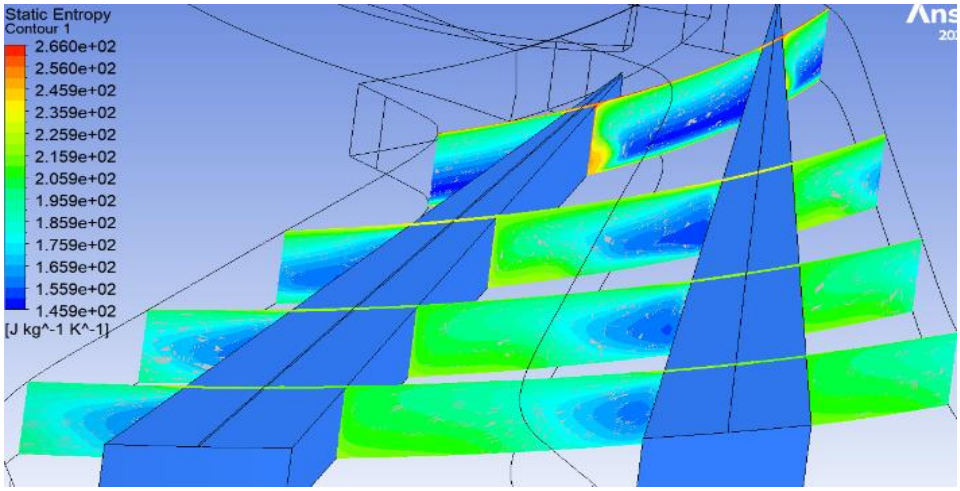

Figure 4. 52: Tip clearance 3% M.

We see that the losses are less than 0% tip losses, so we can say that it's more efficient than the previous one.

4.5.1.3. Tip clearance 6%:

The images below show the variation of different aerothermodynamic parameters for orthogonal planes in different corrective flow values and Tip values equal to 3%.

- The main point **M =2.08 [kg/s]**, it is a middle point
- The point next to surge **S=2.16[kg/s].**
- The point next to sonic blockage **P=1.90 [kg/s]**.

Static pressure:

This figure shows us the variation of static pressure of the impeller and diffuser for the orthogonal plane with a Tip clearance of 6%.

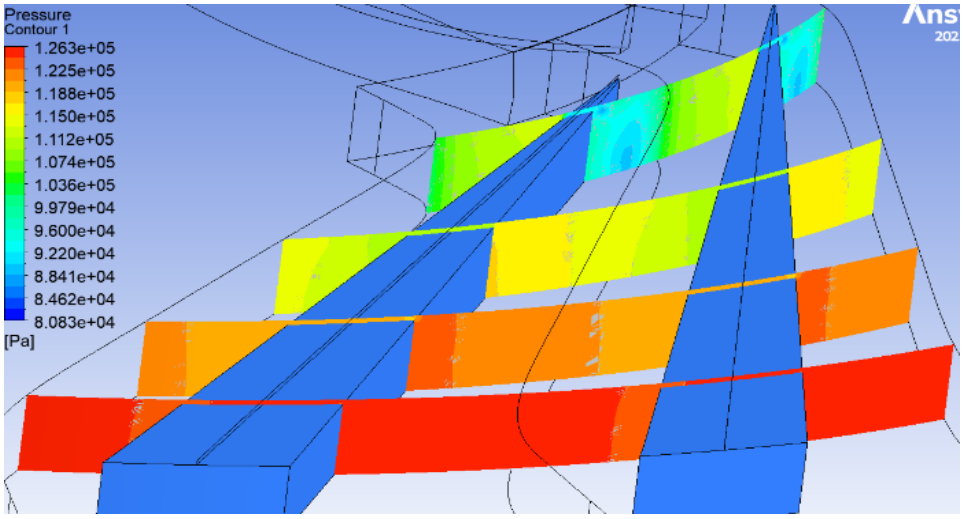

Figure 4. 53: Tip clearance 6% S.

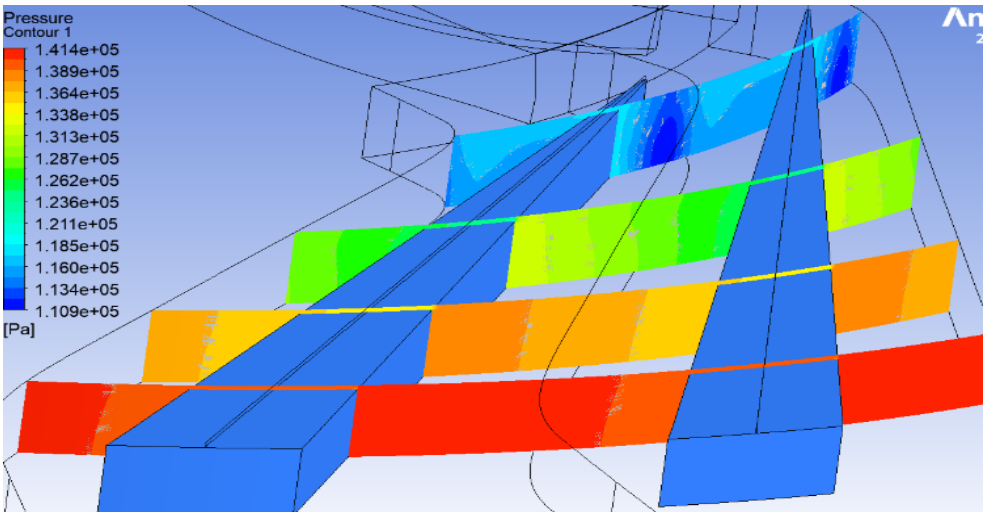

Figure 4. 54: Tip clearance 6% P.

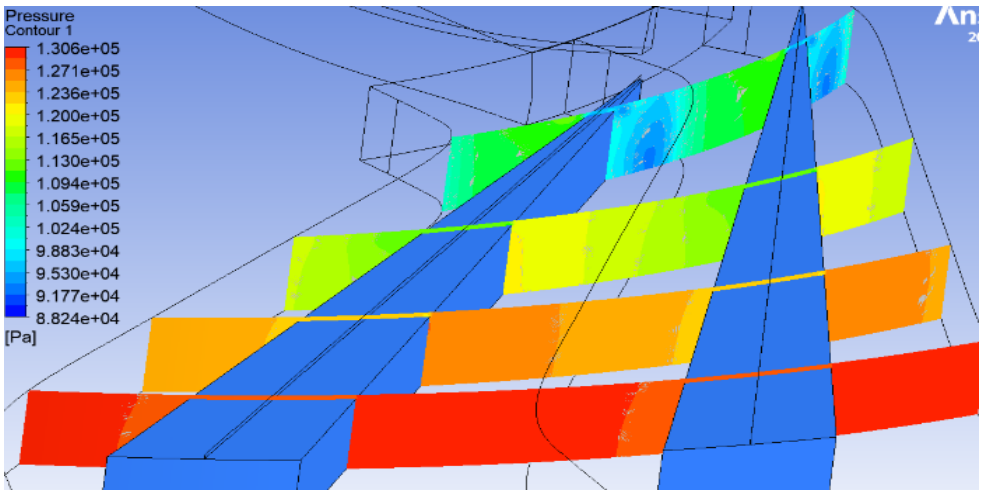

Figure 4. 55: Tip clearance 6% M

We have a lower range value compared to the previous tip.

Mach number:

This figure shows us the variation of the Mach number of the impeller and diffuser for the orthogonal plane with a Tip clearance of 6%.

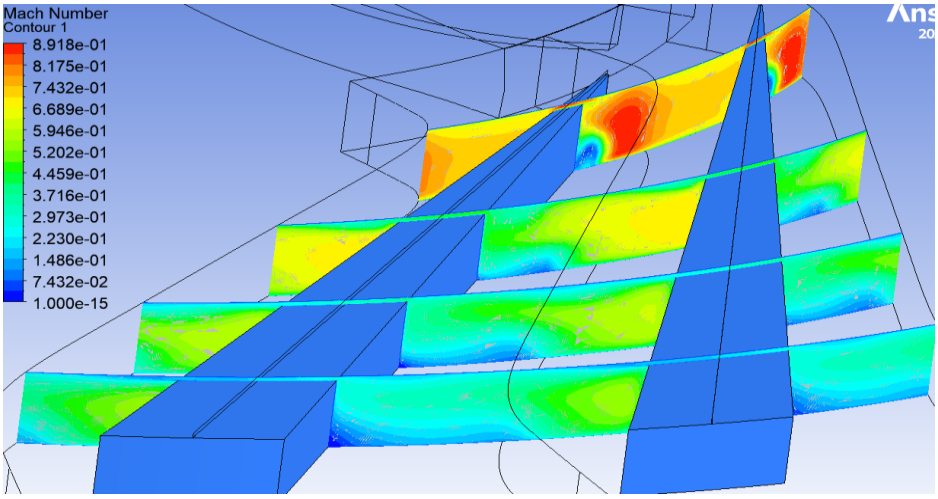

Figure 4. 56: Tip clearance 6% S.

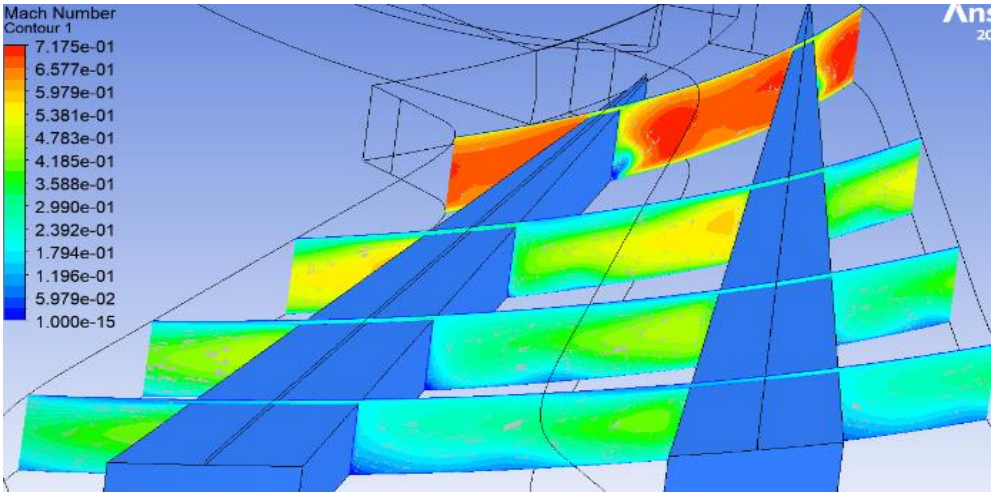

Figure 4. 57: Tip clearance 6% P.

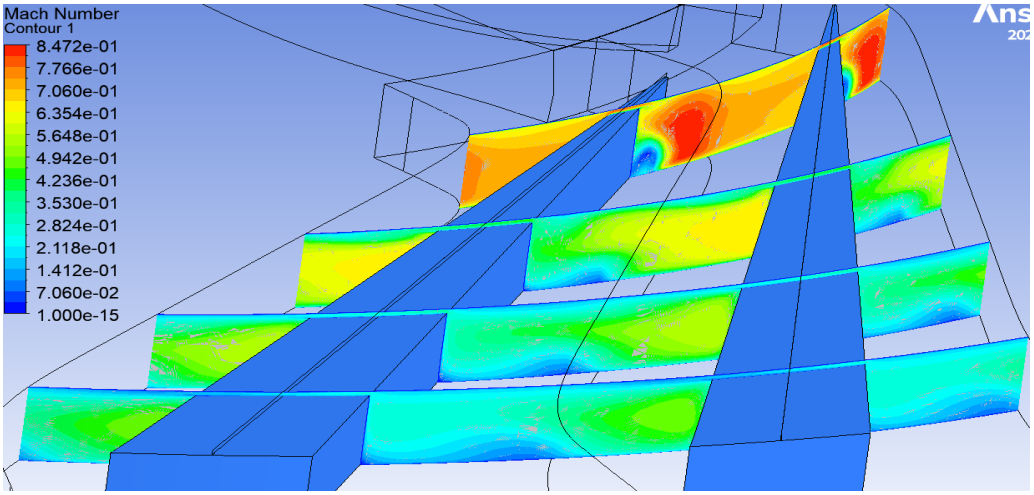

Figure 4. 58: Tip clearance 6% M.

We have the Mach range between 0% and 3% Tip

Static entropy:

This figure shows us the variation of static entropy of the impeller and diffuser for the orthogonal plane with a Tip clearance of 6%.

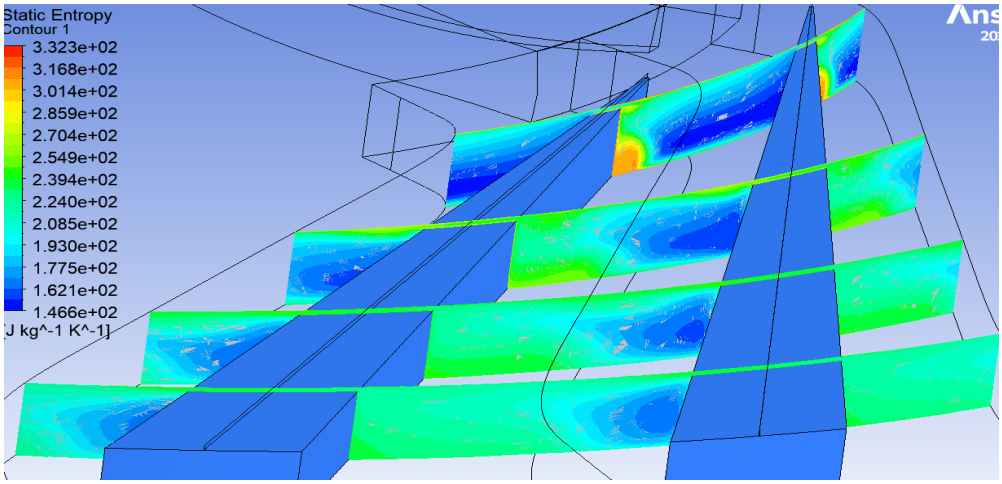

Figure 4. 59: Tip clearance 6% S.

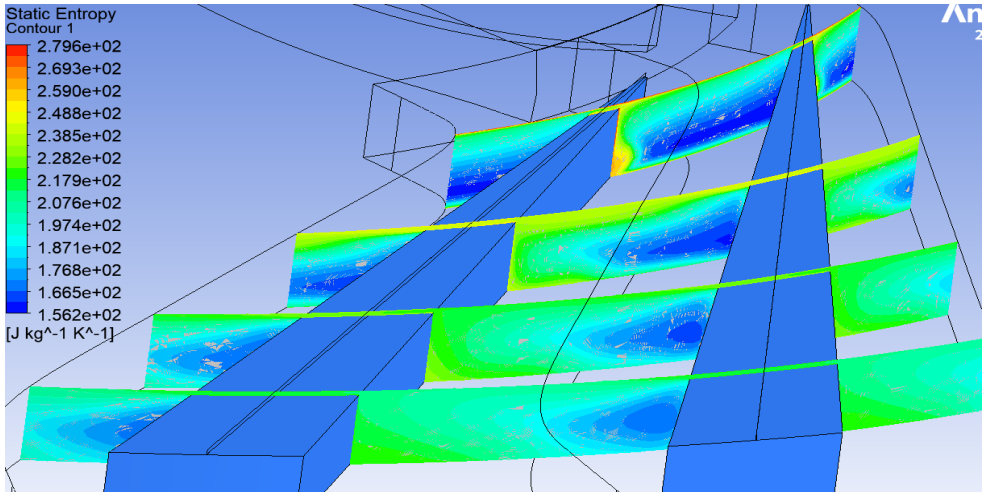

Figure 4. 60: Tip clearance 6% P.

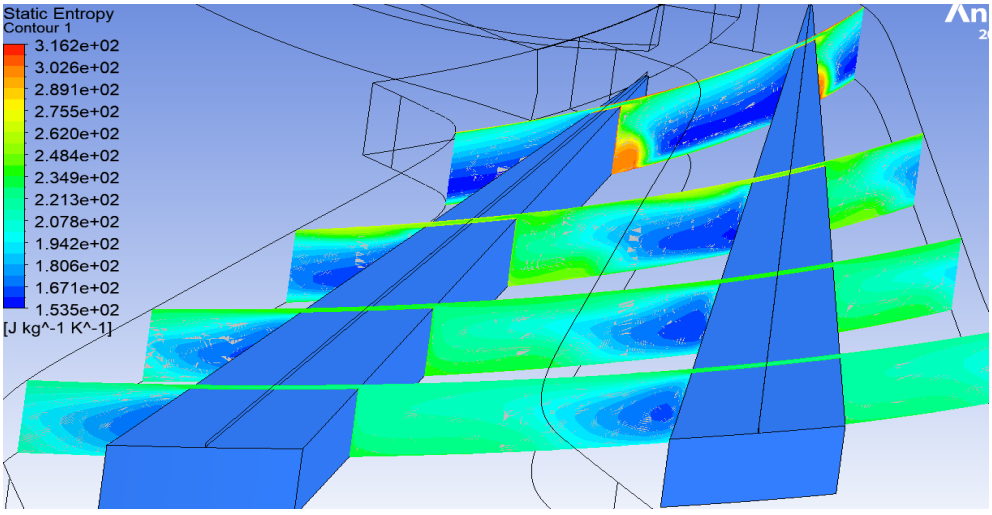

Figure 4. 61: Tip clearance 6% M.

We see that the losses in this Tip are lower than the first one and greater than the second one.

Table 4. 3: This table shows the results of our subject

	Corrective flow	efficiency	Pressure ratio	Temperature ratio
Shroud Tip= 0	M=2.016	0.778384	2.37073	1.35932
	S= 2.1623	0.598193	1.92824	1.34494
	P= 1.8985	0.853119	2.57702	1.36403
Shroud Tip= 3%	M=**2.04792**	0.812458	2.45344	1.35976
	S= **2.1566**	0.769112	2.29675	1.34865
	P= **1.86504**	0.82328	2.56367	1.37486
Shroud Tip= 6%	M=**2.08282**	0.775675	2.29981	1.34632
	S= **2.16392**	0.760775	2.24119	1.34085
	P=**1.90567**	0.814323	2.45618	1.35944

In this table, we put all the results of our simulations.

We can translate the previous table to this chart, which is also resuming our study.

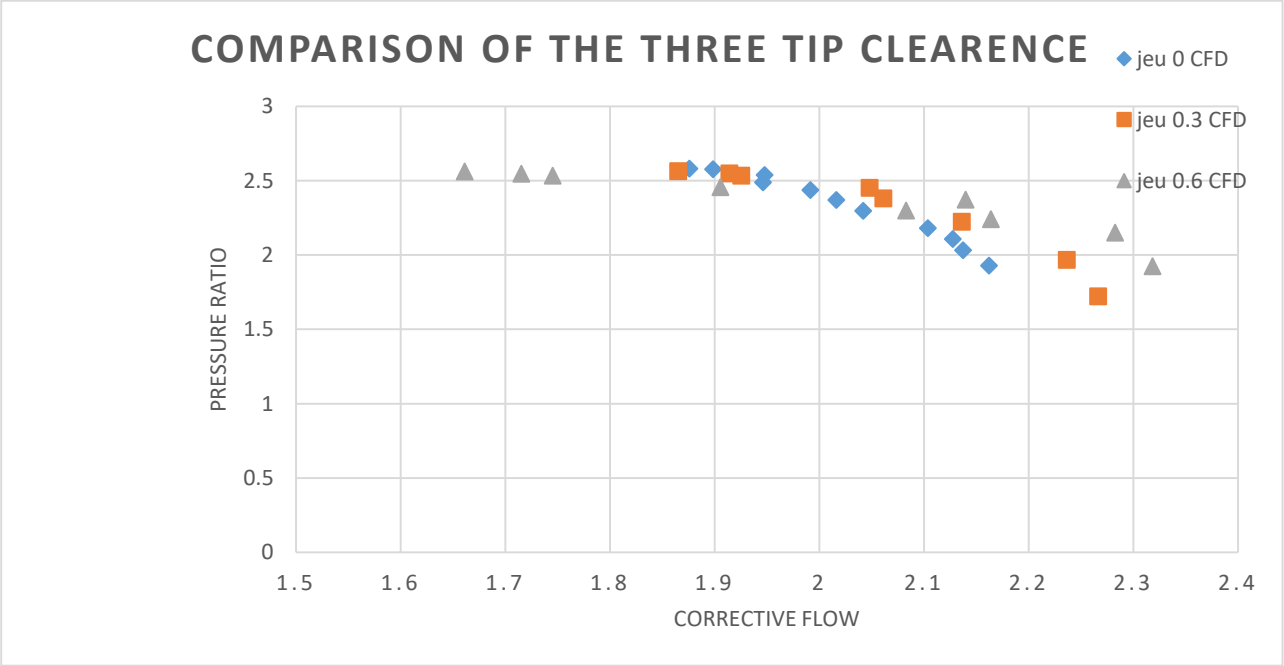

Figure 4. 62: comparison of the three-tip clearance

Conclusion:

The analysis of the results of the numerical simulation of the compressor stage allowed better understand the flow of air within it, and especially to highlight the shock waves that represent a considerable loss of efficiency in the turbomachinery.

Numerical analysis of three-dimensional, compressible, viscous flow and turbulent in steady state in the stage realized by the calculation code ANSYS CFX. The results obtained are comparable with experimental results.

The choice of mesh is made by comparing the results of three different element number values with the experimental results. We found our better mesh number 2.

To treat the problem, we start with the basic laws of fluid dynamics, and then we process these equations through the statistics laws of Reynold and Faver which gives us the Reynold tensor.

To solve the Reynold tensor, we need to use a turbulence model.

The choice of turbulence module was K omega SST, we chose This turbulence model because it uses the K Epsilon formulation near walls and the K-omega formulation in free-flow region.

The simulations were done with many design points, which allowed us to get many parameters and flow values.

The flow influences the parameters and the performance of the compressor. We found that the more flow increases, the more the parameter decreases.

Tip clearance influence: from the simulation,

We found that Tip 3% has performance greater than 0%, and takes more flow to decrease compares with 0%.

However, 6% Tip has can have high performance in wide field of flow compares with others.

So we can say that the tip clearance delays the diminution zone for the performance by changing the shock wave angle and decreasing the loss in the diffuser, which keeps the performance from decreasing with the flow rising.

References:

1. Modelisation de la turbulence pour la CFD Remi Manceau (2023)
2. Boyce, Meherwan P. Centrifugal compressors: a basic guide(2003)
3. G. DUFOUR, "Contributions to the modeling and calculation of flows in Centrifugal compressors: Application to the design by laws of similarity'', memory of Doctorate, the National Polytechnic Institute of Toulouse. 2006.
4. Kai U. Ziegler: a study on impeller diffusor interaction part 1(2002)
5. Boundary Layer Transitional Flow in Gas Turbines M O H S E N J A H A N M I R I (2011)
6. Matteo Bardelli: Numerical Investigation of Impeller-Vaned Diffuser Interaction in a Centrifugal Compressor(2019)
7. Simulation numérique des compresseurs et des turbines automobiles Hadi Tartousi (2012)
8. Analytical prediction of turbocharger compressor performance: a comparison of loss models with numerical data. Sergio Sanz solaesa.(2016)
9. Loss Development Analysis of a Micro-Scale Centrifugal Compressor Jonna Tiainen(2018)
10. TURBOMACHINERY NOTES B. TECH VI SEM (2010)
11. wide Program on Fluid Mechanics Modules on High Reynolds Number Flows K. P. Burr, T. R. Akylas & C. C. Mei (2015)
12. ONERA écoulement secondaire compresseur centrifuge ; 2003 www.onera.fr
13. Alireza Ameli 'NUMERICAL SIMULATION OF ROTOR-STATOR INTERACTION AND TIP CLEARANCE FLOW IN CENTRIFUGAL COMPRESSORS'(2015)
14. JIRI BLAZEK: COMPUTATIONAL FLUID DYNAMICS Principles and Applications (2007)